Crest Factor Reduction and Digital Predistortion of RF Power Amplifiers Driven By Carrier Aggregated Signals

by

Bilel Fehri

A thesis
presented to the University of Waterloo
in fulfillment of the
thesis requirement of the degree of
Doctor of Philosophy
in
Electrical and Computer Engineering

Waterloo, Ontario, Canada, 2015

Author's Declaration

I hereby declare that I am the sole author of this thesis. This is a true copy of the thesis, including any required final revisions, as accepted by my examiners.

I understand that this thesis may be made electronically available to the public.

Abstract

Advanced modulation techniques and access technologies are enabling higher data-rate communication at the cost of stringent signal requirements affecting radio transceivers' efficiency and cost. One of the major problems is the high peak to average power ratios (PAPRs) of modern signals, which are imposing contradictory linearity and efficiency constraints on radio frequency power amplifiers (PAs). One key solution to extend a PA's linearity and efficiency is the application of digital predistortion (DPD) techniques which are fundamentally based on accurate modeling of the PA behavior. A second approach is the deployment of crest factor reduction (CFR) techniques to effectively reduce the PAPR of the signal. To date, significant progress has been reported in the literature in both of these areas, but only in the context of single-band multi-carrier signals.

Recently, in an attempt to extend bandwidth and increase spectral efficiency, new standards have been adopting multi-band multi-standard communication schemes. These signals, also known as carrier aggregated signals, introduce two new challenges to the design of efficient radio systems. First, the wide spectral separation of the different component carriers (up to 1 GHz separation), challenges the fundamental assumption of conventional modeling schemes and CFR techniques (i.e., the envelope only processor hypothesis). Extending or revising classical single-input single-output formulations and methods is not viable, and a multi-input multi-output (MIMO) methodology needs to be developed. A second challenge is the projected deployment of up to five component carriers per signal. Based on conventional methodology, this implies the expensive deployment of up to five predistorters, five transmitter observation receivers (TORs) and five training engines (TEs). This thesis presents a number of contributions addressing the above challenges and paving the way for the deployment of carrier aggregated radios.

The first contribution of this thesis is the development of MIMO CFR and dual-band DPD modules to enable the low-speed baseband processing of carrier aggregated signals. A low-speed CFR solution is proposed and extended to different deployment scenarios (i.e., component carriers with different average powers, component carriers with different modulation schemes, and an arbitrary number of component carriers). Next, the conventional PA behavioral modeling approach is reviewed and reformulated to effectively design a novel dual-band DPD scheme.

The second contribution is the efficient hardware implementation of predistortion algorithms. A symbolic optimization approach is proposed to enable the joint optimization of the two dual-band predistorters sharing the same predistortion engine, effectively avoiding duplication of the predistortion modules. Next, a time-shared 1-TOR 1-TE real-time adaptive learning approach is proposed to effectively linearize a dual-band PA.

Acknowledgments

I would like to express my sincere thoughts to all of those who helped me to get through this challenging PhD journey.

My great gratitude goes to professor Slim Boumaiza, my supervisor, for his unlimited support. I am deeply indebted to him; he taught me how to be patient in research, how to seek results and how to be professional.

I would like to thank my family for their support and daily prayers. Thanks should also be addressed to all my friends here in Canada.

Table of Contents

List of Figures

List of Tables

Nomenclature

3GPP 3rd Generation Partnership Project

ACLR Adjacent Channel Leakage Ratio

ACPR Adjacent Channel Power Ratio

ADC Analog to Digital Converter

BBE BaseBand Equivalent

CC Component Carrier

CDMA Code Division Multiple Access

CF Crest Factor

CFR Crest Factor Reduction

DAC Digital to Analog Converter

DDR Dynamic Deviation Reduction

DE Drain Efficiency

DPA Doherty Power Amplifier

DPD Digital PreDistortion

DUT Device Under Test

E-UTRA Evolved Universal Terrestrial Radio Access

ET Envelop Tracking

EVM Error Vector Magnitude

FPGA Field-Programmable Gate Array

GaN   Gallium Nitride

GSM Global System for Mobile Communications

HDL   Hardware Description Language

HSDPA High-Speed Downlink Packet Access

LDMOS Laterally Diffused Metal Oxide Semiconductor

LPE   Low Pass Equivalent

LSE   Least Square Error

LTE   Long Term Evolution

LTE-A Long Term Evolution Advanced

LUT   Look-Up Table

MRAC Model Reference Adaptive Control

PA   Power Amplifier

PAE   Power Added Efficiency

PAPRs Peak to Average Power Ratio

PE   Peak Estimator

QAM Quadature Amplitude Modulation

QPSK Quadrature Phase Shift Keying

RMS   Root Mean Square

SISO Single-Input Single-Output

SNR   Signal to Noise Ratio

TE   Training Engine

TOR   Transmitter Observation Receiver

UMTS Universal Mobile Telecommunications System

WCDMA Wide-band Code Division Multiple Access

Chapter 1

Motivation and Introduction

1.1   Introduction

In order to respond to the demand for increased data rates, the latest communication standards are calling for a number of advanced access technology and modulation schemes requiring stringent signals which are affecting radio transceivers' efficiency and costs. For example, modulation schemes have evolved from a quadrature phase shift keying (QPSK) approach in the universal mobile telecommunications system (UMTS) release 99 3G standards, to a 16 quadrature amplitude modulation (QAM) approach for high-speed downlink packet access (HSDPA) under 3.5G standards, and then a 64 QAM-based scheme for long term evolution advanced (LTE-A) 4G standards. This has enabled an increase in the modulation index from 2 bits/symbol to 8 bits/symbol. As a result, the requirements on a signal's quality such as error vector magnitude (EVM) and signal to noise ratio (SNR) have become significantly more stringent (e.g., from 17.5% EVM for QPSK down to 8% EVM for QAM 64). Furthermore, access technologies such as code division multiple access (CDMA) and orthogonal frequency division multiplexing (OFDM), have enabled the development of more spectrally efficient radio access techniques with better immunity to multi-path fading and inter-symbol interference. The CDMA approach is used in CDMAone (2G), WCDMA (3G) and Cdma2000 (3G) technologies while OFDM has been adopted in long term evolution (LTE) (3.9G) and LTE-A (4G) standards. As these access technologies involve the summation of multiple modulated signals which have been independently phased, they yield signals with high peak to average power ratios (PAPR) – exceeding 10 dB under the LTE-A standards.

The stringent EVM constraints and problems of high PAPR, presented by advanced modulated signals, are imposing contradictory linearity and efficiency requirements on radio frequency (RF) power amplifiers (PAs). In order to respect transmission regulations and guarantee signal quality, PAs must be linear. However, the average efficiency of a linear

PA (which dominates the transceiver's power consumption), ranges between 10-20%. This means that only one fifth of the DC power consumed is converted to RF; the remaining power dissipates as heat, requiring that expensive cooling systems be employed to prevent overheating. PA efficiency and linearity enhancement solutions must be innovated in order to develop functional and cost effective wireless communication infrastructure.

1.2   Carrier Aggregated Signals

Looking for greater bandwidth and better spectrum resource utilization, the new standards are adopting carrier aggregated communication signals. Under heavy network loads, carrier aggregation will enable load balancing to occur across carriers, thus improving the data rates of all users. Under low or medium network loads, carrier aggregation is able to take advantage of unused resources, leading to significant data rate increases. Some carrier aggregation scenarios have been specified within the communication standards and others are under development. For example:

- 3GPP LTE release-10 supports the use of an up to 100 MHz signal bandwidth obtained through carrier aggregation of as many as five component carriers. This enables a peak data rate of 1 Gbps on downlink and 500 Mbps on uplink. The component carriers can be any of the supported 3GPP LTE release-8 20 MHz signals.

- 3GPP HSDPA release-10 enables the carrier aggregation of up to eight component carriers and a signal bandwidth of up to 40 MHz. As was the case for LTE, the component carriers do not need to be adjacent.

- Carrier aggregation can also provide an architectural solution to support the effective coexistence of emerging and legacy standards. In order to be backward compatible, 4G stations must support frequency bands used by 2G and 3G. Take the use case scenario of two popular signals: 900 MHz HSDPA and 800 MHz LTE. Even though there is limited spectrum availability for each of these signals, they are attractive for use given their relative low frequency (e.g., making coverage within a building easier). Carrier aggregation would enable the provision of the high data rates expected from LTE services while simultaneously maintaining coverage for HSPA devices.

Given how crowded the radio spectrum currently is, a wide contiguous spectrum band (i.e., from 40-100 MHz) is hard to provide, if not impossible. Therefore, LTE release-10 enabled component carriers to be allocated into narrow non-contiguous spectrum bands. As a typical non-contiguous carrier aggregated signal is characterized by widely spaced carriers, the aggregated channel bandwidth may be up to 1 GHz. This results in additional constraints on the analog and digital circuitry design of devices and infrastructure. Furthermore, carrier aggregation can aggravate the signal's PAPR by several dB.
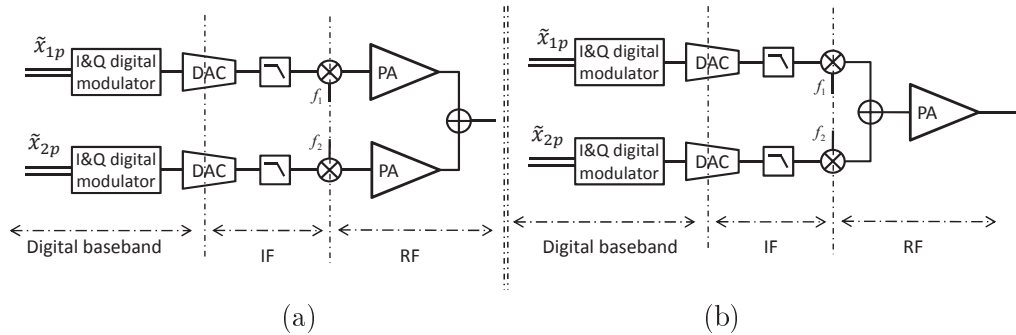
Figure 1.1: Legacy (a) vs. future (b) dual-band carrier aggregated transmitter

1.3 Multi-band Power Amplifiers

To generate carrier aggregated signals, current transceiver architecture modulates each carrier separately and then combines the different carriers after the amplification phase, thus requiring one amplifier for each of the bands (Fig. 1.1 a). This transceiver architecture dramatically increases the deployment cost of the network and forces wireless infrastructure to design and maintain a product line-up of multiple PAs. A better solution, to be adopted by next generation transceivers, consists of combining multi-band signals before amplification, requiring the use of only one concurrent multi-band power amplifier (Fig. 1.1 b).

The deployment of multi-band PAs is conditional on the provision of acceptable linearity and efficiency performance at least comparable to narrow band PAs. A number of enhancement approaches exist for PAs such as:

- Improving the efficiency in the back-off region using advanced PA design techniques and topologies (e.g., load and bias modulation techniques).

- Reducing the PAPR of the signal at the cost of slightly increasing the EVM by using crest factor reduction (CFR) techniques.

- Extending the linear region thus requiring additional linearization techniques (e.g., digital predistortion or DPD)

However, the introduction of multi-band topology raises new research challenges: the accurate multi-band behavioral modeling of concurrently driven multi-band PAs, the manageable implementation of multi-band predistorters, and the development of appropriate and adequate CFR solutions. If classical baseband approaches are adopted, they will engender excessive sampling rates in order to represent multi-band signals in baseband. It is part

3

of the fundamental assumptions for conventional modeling schemes and CFR techniques. Hence, the extension or revision of classical formulations and methods is not adequate – new multi-band centered methodology must be adopted.

1.4 Thesis Objectives

The above discussion revealed several system level challenges hindering the deployment of multi-band transceivers. This thesis contributes to addressing those challenges by targeting the following objectives:

1. Development of a dual-band predistortion model for concurrent multi-band PAs. In addition to mitigating the in-band distortion (already exhibited in single-band scenarios), the proposed model handles the inter-band distortions resulting from the interaction of the two bands' signals. The model runs at a speed relative to the signals' bandwidth and is independent from their separation.

2. Development of a dual-band CFR technique for carrier aggregated signals. The proposed technique handles the fundamental case of widely spaced component carriers and is extended to cover different deployment scenarios. The proposed technique runs at a speed proportional to the signals' bandwidth and is independent from their separation.

3. Development of an optimization approach for the efficient hardware implementation of predistortion algorithms. The approach is characterized by automatic symbolic optimization and automatic high level synthesis (HLS), effectively speeding-up the model to gate flow.

4. Development of a dual-band training algorithm. The algorithm enables time sharing of a single transmitter observation receiver (TOR) and training engine (TE) by the different component carriers.

1.5 Thesis Outline

This thesis is organized as follow:

Chapter 2 introduces modern communication signals' characteristics and the challenges faced by PA designers in order to meet the standard requirements. It enumerates some of the successful multi-band PA prototypes reported in the literature and presents a review of behavioral modeling schemes and CFR techniques.

4

Chapter 3 presents a novel CFR solution for carrier aggregated signals. It starts with a detailed analysis of the conventional clipping approach's limitations in the case of two carrier aggregated signals and proposes an adequate solution. Next, a number of generalized solutions tailored to different deployment scenarios are presented. The covered scenarios are: (i) component carriers having different power levels, (ii) component carriers with different EVM requirements, and (iii) an arbitrary number of component carriers. This chapter concludes with the experimental validation of the proposed CFR solution and compares its performance with the conventional technique.

Chapter 4 outlines the behavioral modeling and DPD of RF PAs. First, in an attempt to find a modeling approach capable of handling carrier aggregated signals, a Volterra series modeling approach applicable to a single-band scenario is proposed. This model is applied to intra-band non-contiguous carrier aggregated signals and treats them as one carrier single-band signals. Next, a dual-input dual-output (DIDO) Volterra series model adequate for an inter-band two carrier aggregated signals scenario is derived and validated.

Chapter 5 presents an automated approach to optimizing the Volterra series DPD hardware implementation in a field-programmable gate array (FPGA). First, a symbolic tool is used to carry out a number of arithmetic transformations and optimize the model's expression. Next, automated fixed-point conversion and HLS tools are used to generate the hardware description language (HDL) code of single- and dual-band Volterra series DPDs.

Chapter 6 proposes a novel linearization system using a single TOR and TE for PAs driven with inter-band carrier aggregated signals. The proposed architecture implements a recursive least squares estimator applied to a model reference adaptive control (MRAC) learning approach. Unlike conventional architectures which simultaneously linearize both bands, the 1-TOR/1-TE is switched between the two bands and the respective DPD techniques are trained and applied.

The last chapter concludes the technical results of this thesis, enumerates the author's literature contributions and patent applications and proposes potential future research directions.

Chapter 2

Background: Efficiency and Linearity of RF PAs

The incessant progress of wireless communication standard are enabling higher data-rate communication systems. The advance of modern access technology, such as wide-band code division multiple access (WCDMA) and orthogonal frequency division multiplexing (OFDM), enabled spectral efficient communication signals. However, this was achieved at the cost of generating stringent signals affecting radio transceivers efficiency and development complexity. Recently, LTE's evolved universal terrestrial radio access (E-UTRA)[73] enabled the use of frequency aggregated communication signals. These signals has more stringent characteristics challenging the design of efficient radio transceiver. This chapter describes the challenges arisen in order to maintain good signal quality and insure acceptable radio efficiency.

2.1 Carrier aggregated Signal's Characteristics

Recent modulation techniques and access technologies are generating stringent signals characterized with higher bandwidth and PAPR. Meanwhile, the communication standards are imposing strict signal qualities requirements such as EVM and adjacent channel leakage ratio (ACLR), as detailed in the following sub-sections.

2.1.1 PAPR

Peak to average power ratio (PAPR) is a measure that quantifies the amount of variation of the signal envelope. It is calculated as the peak amplitude squared (peak power) divided by the root mean square (RMS) value squared (average power)
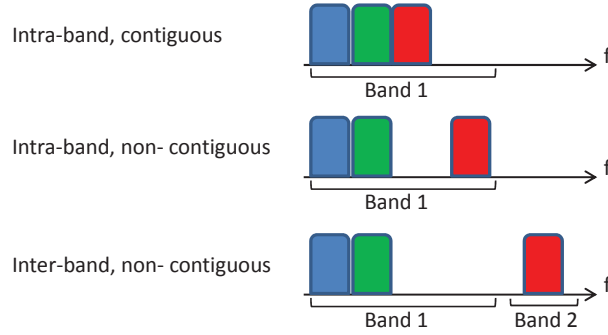
Figure 2.1: Carrier aggregation scenarios

$$PAPR = \frac{|x|_{peak}^2}{x_{RMS}^2}$$

Equivalently, crest factor is computed as the ratio of the peak amplitude of the waveform divided by the RMS value of the waveform

$$C = \frac{|x|_{peak}}{x_{RMS}} = \sqrt{PAPR}$$

For example, sine wave has PAPR of 3 dB, a 2G Global System for Mobile Communications (GSM) signal has a PAPR of 6 dB, 3G WCDMA modulated waveforms PAPR typical value ranging from 6 to 9dB and 4G LTE signal have a PAPR higher than 10 dB. The high PAPR characteristic considerably affects power amplifier efficiency and transistor utilization factor. Assume for example a 10 dB PAPR signal to be transmitted with 10 W average powers. It is then required to use a power amplifier able to handle up to a 100W.

2.1.2 Bandwidth

Both 3G and 4G standards allows up to 20 MHz bandwidth for a communication channel. This correspond to the four-carrier WCDMA signal and 20 MHZ LTE signal, respectively. This bandwidth restriction helped designer to predict a maximum required bandwidth for the analog circuits and the maximum required sampling rate of the digital components.

Seeking more data rate and better radio frequency resource utilization, 4G LTE-advanced standard introduced the carrier aggregated radio scenario. Each aggregated carrier is re-

ferred to as a component carrier (CC). Basing on the operator frequency allocation scenarios, three possible cases are introduced [72, 73], as in Fig. 2.1:

1. Intra-band contiguous: use contiguous CC within the same operating frequency band. As a maximum of five component carriers can be aggregated, the maximum aggregated bandwidth is 100 MHz [73].

2. Intra-band non-contiguous: use non-contiguous CC within the same operating frequency band, separated with a band gap.

3. Inter-band non-contiguous: use non-contiguous CC within the different operating frequency band. In this case, the aggregated communication channel bandwidth may reach a couple of GHz.

The aggregated channel bandwidth become significantly large and has direct impact on analog circuit bandwidth requirements and on digital processor speed and memory. Based on hardware impact considerations, for the following chapters, two cases are distinguished.

1. Wide-band scenario: for both contiguous and non-contiguous intra-band aggregated signals.

2. Multi-band scenario: for non-contiguous inter-band aggregated signals.

2.1.3 EVM

Error vector magnitude (EVM) is a figure of merit for evaluating digital modulated signals quality. EVM measures the difference between the ideal I/Q constellation values of a demodulated symbol vs. the values of the real received ones. The error vector magnitude is equal to the ratio of the power of the error vector to the root mean square (RMS) power of the reference. It is defined in dB as:

$$\text{EVM(dB)} = 10 \cdot \log_{10}\left(\frac{P_{\text{error}}}{P_{\text{reference}}}\right)$$

where P_{error} is the RMS power of the error vector. Alternatively, a percentage measure of the EVM is given by:

$$EVM(\%) = 100 \cdot \sqrt{\frac{P_{\text{error}}}{P_{\text{reference}}}}$$

Unlike bit error rate, EVM is more practical to microwave engineering because it embeds both amplitude and phase errors information, and hence, enable better assessment of the system distortion.

Table 2.1: EVM requirements [72]

Modulation scheme	Required EVM (%)
QPSK	17.5
16 QAM	12.5
64 QAM	8

E-UTRA [72] specify that, for all bandwidths, the EVM measurement shall be performed for each E-UTRA carrier over all allocated resource blocks and downlink subframes within 10ms measurement periods. The EVM requirement depends on the modulation scheme, and have to be better than the limits reported in table 2.1.

2.1.4   ACLR

Adjacent channel leakage ratio (ACLR) is yet another measure of the required transmitted signal quality. It is defined as the ratio of the transmitted RF power on the assigned RF channel to the power in the adjacent channel. It was introduced by UMTS (WCDMA) standard as a replacement of the legacy measure adjacent channel power ratio (ACPR). ACPR is a measure of the degree of signal spreading into adjacent channel, caused by non-linearity in the power amplifier. It is defined as the power contained in a defined bandwidth at a defined offset from the channel center frequency, divided by the power in the defined bandwidth placed around the channel center frequency. The ratio will hence quantify the amount of the interference of the transmitted signal with its neighbor channel.

Whether the transmitted signal is single or multi-carrier, the requirements shall apply outside the base station RF bandwidth edges. E-UTRA [72] specifies that, in all transmission cases, whether in carrier aggregated case or not, the ACLR performance should be better than -45 dB.

2.2   Power Amplifier Efficiency vs. Linearity

A solid state power amplifier uses one or more transistor as an active device to amplify an input signal. A number of dedicated networks are designed to integrate the transistor in a transmission chain, as illustrated in Fig. 2.2.

First, the transistor is biased in active mode for amplification purposes. The biasing is performed by a set of passive components and forms the biasing network. The choice of the bias point dictates the amplifier class of operation. Then, an input and output matching

9
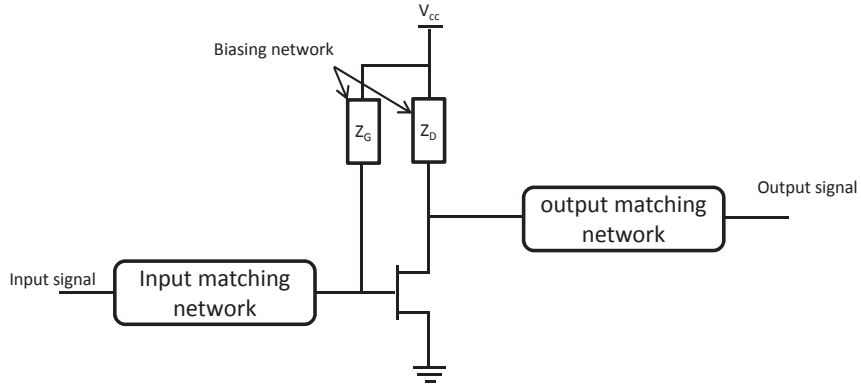
Figure 2.2: Biasing and matching networks

networks are designed to adapt the source and load impedance to the input and output impedance of the transistor, respectively. Load matching networks affects significantly the bandwidth and gain performance of the amplifier.

The design of biasing, input and output matching networks directly affects the efficiency and linearity performance of the power amplifier, and hence, forces designers to make design trade-off as explained in the following sub-sections.

2.2.1 Efficiency

Two equivalent figures of merit are defined to quantify the power efficiency of a power amplifier. The first one is the power added efficiency (PAE) and describes the amount of power added to the signal over the consumed one.

$$PAE = 100.\frac{(P_{out} - P_{in})}{P_{DC}} \tag{2.1}$$

A second efficiency measure is drain efficiency (DE) and given by:

$$DE = 100.\frac{P_{out}}{P_{DC}} \tag{2.2}$$

Different Power Amplifier's classes of operation have different efficiency performances. These classes differs in the bias point of the device, or equivalently, the conduction angle. Conventional classes of operations are classes A, AB, B, and C. As shown in Fig. 2.3, efficiency is increased from Class A all the way to Class C. Drain efficiency increases

sharply as the quiescent bias level is reduced. Unfortunately, this increase of efficiency is made at the expanse of lower gain.
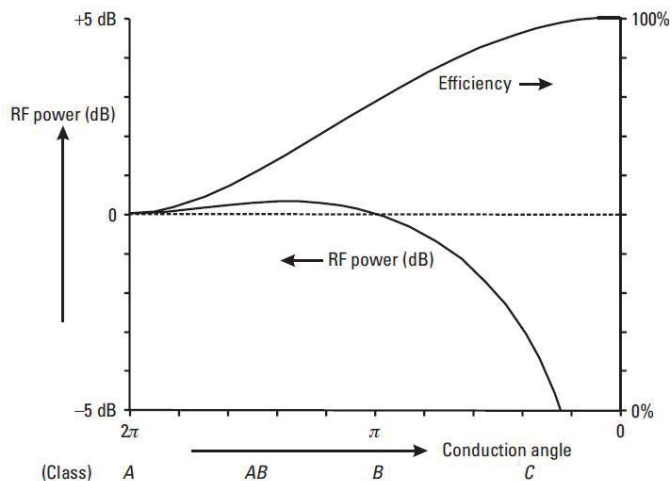
Figure 2.3: Efficiency of classical amplifier architecture [74]

2.2.2 Distortion

Distortion of power amplifier is any deviation of the output signal from the linear power amplifier response. It can be categorized into linear and nonlinear distortion. Linear distortion is characterized with change of scale implying variation of the gain factor vs. frequency such as the action of a filter. However, nonlinear distortion is a more complex phenomenon that produces modifications of gain vs. input power and frequency and generates new frequencies components.

Power amplifiers are unfortunately characterized with both linear and nonlinear distortion. Linear memory effect is the distortion caused by the non-flat frequency response of power amplifier input and output matching network which are designed for a specific carrier frequency, and causes reflections in frequencies different from the central one. This problem accentuates when wide-band signals are deployed and becomes significantly severe in multi-band cases. However, nonlinear distortion is caused by the PA transistor, usually known as static nonlinearity.

The distortion mechanism in PA gets more complicated as linear memory effect and nonlinear static distortion interacts through a feedback process caused by the biasing net-

11

work, as depicted in Fig. 2.2. This mechanism produces distortion commonly known as nonlinear memory effect.

2.2.3 Linearity vs. Efficiency Trade-off

Linearity and efficiency are conflicting goals that a PA designer have to trade off between. Fig. 2.4 illustrates that at low output power level, linearity is high and efficiency is too low. However, in higher and efficient output power, linearity is poor. Designers compromises efficiency and linearity to operate the PA efficiently and with the minimum possible distortion.
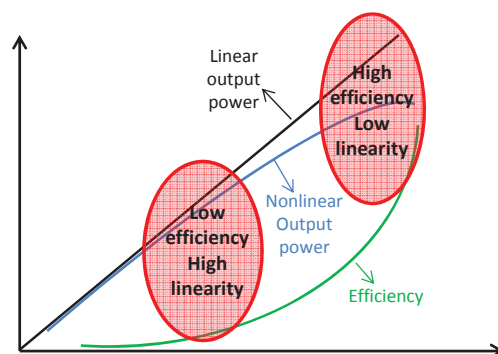
Figure 2.4: Linearity vs. efficiency

2.3 Efficiency and Linearity Enhancement Techniques in Single-band Scenario

As power amplifiers dominates the transmitter's power consumption, efficiency and linearity enhancement techniques have attracted major attention in the research community. Three enhancement approaches exists; more efficient designs, clipping solutions and linearization techniques. Indeed, the approach aims at improving PA's efficiency over classical design through novel topological and technological circuitry. Clipping techniques aims at reducing the signal PAPR with minimal distortion generation in order to lower the PA's power back-off. The first two approaches increases PA efficiency at the cost of added signal distortion. It is the duty of the third approach, i.e. linearization techniques, to improve the linearity.
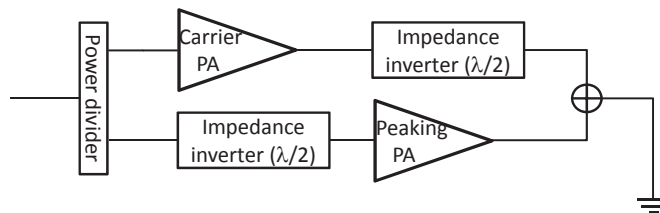
Figure 2.5: Architecture of Doherty amplifier

2.3.1 Advanced PA Designs

Modulated signal's high PAPR implies that power amplifiers, typically designed to be most efficient at peak power, are now on average operating in significant back-off where their efficiency is considerably reduced. The higher the PAPR, the higher the power back off is, and hence, the lower the power efficiency is. Extensive research was conducted in the literature, and advanced PA design techniques, such as load (Doherty [40, 41, 42, 43]) and drain-supply (envelope tracking [44, 45, 46]) modulations, have been applied to improve efficiency at the back-off region of single-band PAs. Envelop tracking (ET) solution was found more suitable for hand-held mobile devices where the Doherty solution was found more suitable for base stations. Being the device under test (DUT) used in this thesis, Doherty power amplifier theory of operation is explained as below.

A Doherty power amplifier (DPA) system combines the outputs of two RF amplifiers, called carrier and peaking amplifiers, through an impedance inverter as shown in Fig. 2.5. The impedance inverter could be a quarter-wavelength transmission line or its equivalent lumped-element circuit. It aims at converting the carrier device from a current source to a voltage source. The carrier amplifier is biased in class AB and the peaking amplifier is biased in class C. The power divider split the power between the carrier and peaking amplifier. The quarter-wavelength delay (or equivalent circuit) in the input path of the peaking amplifier compensate for the delay introduced by the quarter-wavelength delay in the output of the carrier amplifier.

The fundamental idea of a DPA is to let the carrier amplifier to work at peak power to yield a maximum efficiency, meanwhile the peaking amplifier deals with the modulation peaks. The Doherty amplifier implements the technique known as load modulation. In fact, at low power the peaking amplifier is off and the carrier one is usually designed to reach saturation around the targeted average power. At high output power, the peaking amplifier is on, and, being a current source, it dictates current amount pumped into the load. Meanwhile, the carrier amplifier cascaded to the quarter-wavelength behaves as a voltage source, and dictates voltage across the load. As a result to Kirchhoff laws, current pumped by the carrier amplifier has to decrease. This is seen from the carrier device as a load impedance decrease. This behavior implements the load modulation theory which
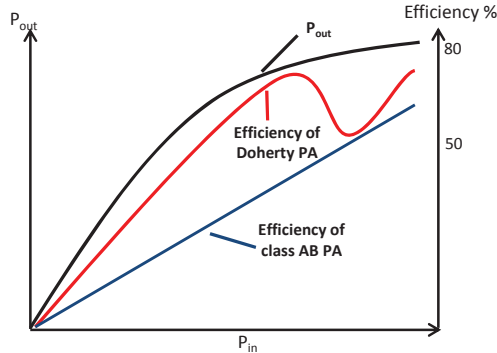
Figure 2.6: Efficiency of Doherty power amplifier

guaranties maximum efficiency not only at peak power like classical amplifier classes, but also at back-off levels.

DPA has shown significant power efficiency enhancements over the standard Class AB amplifier, Fig. 2.6. It offers back-off efficiency improvements of 20 % and 40 % for signals with 10 dB and 6 dB, respectively.

2.3.2 Crest Factor Reduction

The development of crest factor reduction (CFR) techniques was motivated by the fact that time-domain multi-carrier signals usually exhibit large amplitude variations, which can be approximately described by the Gaussian distribution. As a result, the envelope and power of the signal satisfy the Rayleigh distribution and the exponential distribution, respectively. These distributions tail reveal that signal comprises low probable large amplitudes, theoretically approaching infinity. Although those tails are very improbable, they increase the signal PAPR significantly. A good idea is to limit those tails to significantly reduce the signal PAPR while accepting a minimal distortion. With a powerful PAPR reduction technique, we can expect high power efficiency, low nonlinear distortion, and small dynamic-range requirement of the analog components. CFR is a useful tool to boost the transceiver performance.

In the literature several techniques have been devised for crest factor reduction of single-band signals. These techniques can be divided into two categories:

- Distortion-less methods (commonly called also linear CFR techniques), such as selected mapping [3], partial transmit sequence [4], tone injection, tone reservation, and coding [5, 6].

14

- Distortion-based methods (called also nonlinear CFR techniques) such as clipping and windowing [7], companding [8], active constellation extension (ACE) [9], and generalized ACE methods [10].

Linear techniques can achieve more significant crest factor reduction than their nonlinear counterparts and without altering the signal quality. However, they usually require modifications of the receiver that may be incompatible with existing communication systems.

2.3.3 Digital Predistortion

Efficiency enhancement achieved by novel architectures has been compromised by the accentuation of signal distortion problems. In order to conform to the radio access regulations and standards, a solution to address the distortion has been a prolific area of research leading to the development of several linearization techniques; namely feed-forward, feedback and predistortion techniques. While the predistortion technique, particularly its baseband digital form, has been widely adopted to mitigate the distortions generated by RF PAs in 3G wireless base stations, more work is required to meet the challenges of 4G wireless networks using wide-band signals. Investigators of digital predistortion (DPD) have struggled with linearization capacity and implementation complexity.

The basic function of a predistorter is shown in figure 2.7. It consists in implementing an inverse behavior of the nonlinear amplifier. The cascade of the predistorter with the PA will engender a linear response at the output stage.
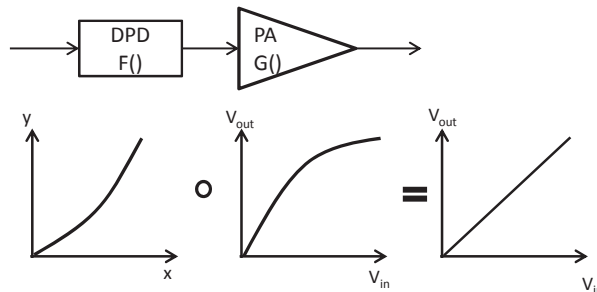
Figure 2.7: Predistortion concept

Over time, DPD schemes have evolved from simple memoryless models to more sophisticated types which attempt to mitigate the memory effects that gain intensity as the signal bandwidth widens. Several DPD schemes with memory have been proposed, mainly consisting of derivations of the low pass equivalent (LPE) Volterra series [15]. In order to address the complexity burden of the LPE Volterra series [16], these derivations discard

15

kernels that are considered negligible. One popular example is the memory polynomial model [17], where several polynomials are applied to the delayed input signals' samples separately and delayed cross-terms are discarded. Another approach, dynamic deviation reduction (DDR), has been employed to elegantly prune the LPE Volterra series [21]. It begins by reformulating an LPE Volterra series expression to assemble terms with the same dynamic distortion order. By setting a value for the maximum allowed dynamic order, such a reformulation allows a simple elimination of distortion terms of higher dynamic order in the LPE Volterra series, consequently reducing its complexity. A DDR based LPE Volterra series with a preset value for the dynamic order equal to one or two has been used to linearize various RF PAs and significant linearization results were reported for different types of signals. Yet, as the signals' bandwidth increases, and PA's memory effects gain intensity, a larger value for the dynamic parameter of the DDR technique is needed and eventually the complexity of the pruned LPE Volterra series approaches the un-pruned series.

2.4 Efficiency and Linearity Enhancement Techniques in Multi-band Scenario

The amplification of carrier aggregated signals by a single power amplifier poses several challenges (Fig. 1.1). Indeed, such a PA is required to maintain good power efficiency over multiple frequency bands. This has motivated many recent research attempts to develop high efficiency and multi-band and broadband PAs [2]. In addition, due to the high CF of the carrier aggregated signals, these PAs are often required to operate in the large back off region from their peak power to meet the linearity requirements, and consequently they yield poor power efficiency. The simultaneous amplification of several carriers aggravate also to the signal distortion due to the mutual distortion. The advance of carrier aggregation radio challenged the microwave research community with new objectives as detailed in the following subsections.

2.4.1 Advanced PA Designs

Processing multi-band signals using single multi-band PA, with RF performance (efficiency, gain, output power) comparable to multiple single-band PA modules (Fig. (1.1), is challenging.

Researchers focused first at previous efforts to improve the efficiency and linearity of single-band PAs and identified their sources of bandwidth limitations and devised solutions to mitigate them. It was also proven that, because of the high bandwidth of carrier aggregated signals, the dual band signal fractional bandwidth ratio defined as the bandwidth of

the signal over the carrier frequency, is very high and harden the design of matching networks. The bias network design, which bandwidth is normally 5 times the signal bandwidth, is further complicated too. Those limitations were examined and several proof-of-concept prototypes have been proposed and demonstrated excellent efficiency in the back-off region over a wide range of frequencies [47, 2, 48, 49, 14].

2.4.2   Crest Factor Reduction

Linear techniques were successfully applied to multi-carrier single-standard signals through proper modulation and coding [11]. However, their generalization to carrier aggregated multi-standard signals is not possible due to the dissimilarity between the modulation schemes employed in each carrier. Linear CFR solutions being unavailable, the PAPR of the carrier aggregated multi-standard signal is expected to be significant, and hence, nonlinear methods are a must.

The nonlinear CFR techniques are generally carefully applied to obtain the highest possible reduction while not exceeding a given distortion threshold. These techniques, and in particular the clipping/windowing one, were applied to multi-carriers signals co-located in the same spectrum band [12]. However, their application to carrier aggregated signals, especially when each carrier is located in different and widely spaced band, is very challenging as it will require high sampling rate.

As I will investigate on multi-band multi-standard scenarios, CFR techniques are categorized differently. Two types are distinguished:

- Baseband Methods: which are CFR techniques applied individually to baseband components of the multi-carrier signal.

- IF Methods: which are CFR techniques applied to the multi-carrier signal combined in IF.

IF methods could be divided to single-band multi-carrier techniques where the signal carriers are adjacent and belongs to the same band, and multi-band multi-carrier methods where the signal carriers belongs to different bands, i.e. widely separated.

The later scenario was not investigated in the literature and is addressed in this thesis. A low computational complexity and power overhead approach for the CFR in the case of carrier aggregated signals is proposed.

2.4.3   Digital Predistortion

As the application of the LPE Volterra series approach to the linearization of single-band PAs which exhibit significant memory effects was conditional on its successful pruning

17

[16, 20] and is unmanageable and impractical in wide-band cases, researchers investigating dual-band DPD schemes opt to discard the Volterra series option. Hence, most of the recent work has concentrated on efforts to generalize the previously mentioned low complexity schemes to the dual-band PA context, at the cost of linearization performance.

Several attempts to devise describing functions to implement a dual-band model was reported in the literature.

Roblin et al. [58] proposed a third order frequency selective predistortion technique to handle each band separately in order to model and/or linearize PAs exhibiting strong "differential" memory effects (i.e., high imbalance between the upper and lower in-band and inter-band distortion components). This technique was tested using a multi-carrier 20 MHz WCDMA signal [58] and extended to address the 5th order inter-modulation distortions of a PA driven with multi-tone signals [59]. Although this technique was applied to multi-carrier single-band signals, it can be generalized to the dual-band case provided the required sampling rate is reduced to cope with large frequency spacing.

Cidronali et al. [60] proposed an IF dual-band model implementing a Wiener Hammerstein DPD scheme using a sub-sampling feedback path. Although the reported simulation results showed 10 dB spectrum regrowth reduction, the proposed architecture involved digital to analog converter (DAC) and analog to digital converter (ADC) with disproportionate sampling rates and complicated IF processing.

Furthermore, starting with a 5th order memoryless model driven with a dual-band signal, Bassam et al. [61] showed that the PA's output in each band depends on both PA input signals. This observation has been generalized to the memory polynomial model to yield a two dimension DPD (2D-DPD) model. Reported linearization results [61, 62, 65, 63, 64] demonstrated a 12 dB improvement of the ACLR at the cost of a large number of coefficients.

Quindroit et al. [68] and Yang et al. [69] proposed an orthogonal representation to handle the ill-conditioning problem and numerical instability of the 2D-DPD model.

Alternatively, Liu et al. [70] proposed 2D Hammerstein and 2D Wiener models to address the large number of coefficients required by the 2D-DPD model. When applied to construct a behavioral model of a dual-band PA with a nonlinearity order equal to 5 and a memory depth equal to 5, the 2D Hammerstein and 2D Wiener models needed 40 coefficients in each band as opposed to the 2D-DPD which required 150 coefficients [70]. However, while the 2D-DPD model has been validated as a dual-band digital predistorter, the application of the 2D Hammerstein and 2D Wiener models to the linearization of dual PAs is problematic and only behavioral modeling results have been reported.

Ding et al. [66] pointed out the implementation complexity of the 2D-DPD and suggested a two dimensional look-up table (LUT) based representation as an alternative. This latter approach was further simplified to use single dimension LUTs. When applied to the

linearization of a dual-band PA driven with dual-band signals (separated by 97 MHz), the model demonstrated an ACLR of about -45dB, which barely passes the mask. However, the proposed DPD scheme was operated with a sampling rate equal to 153.6 MHz and consequently a large oversampling rate with a 10 MHz signal.

Other work has focused on devising more sophisticated Volterra series based dual- and tri- band DPD models [84, 95, 87] and on augmenting these models to mitigate distortions exhibited by dual-band envelope tracking PAs [96, 97, 98].

In this thesis, the LPE Volterra series formulation, which has been at the center of the majority of baseband DPD schemes, is reviewed. A novel modeling approach will be proposed and used to model and linearize a concurrently driven dual-band PA. Special set derivations will be followed to construct the dual-band Volterra to avoid the previously highlighted complexity issue and the use of pruning methods.

Chapter 3

Crest Factor Reduction of Carrier Aggregated Signals

The absence of frequency bands that can support wide transmission bandwidths called for the intra-band or inter-band aggregation of multiple carriers according to specific set of technical requirements [1]. Such carrier aggregated signals inherit and accentuate the challenging characteristics of the constituent carriers, such as the high peak to average power ratio also commonly referred to as crest factor (CF), and wide bandwidth. As power amplifiers efficiency and analog to digital converters dynamic range are heavily affected, crest factor reduction (CFR) techniques were proposed in literature to mitigate the high PAPR problem. Although several techniques have been devised for single-band signals, solutions for multi-band signals are still lacking.

In the following sections, we propose an effective approach for the crest factor reduction of multiple, widely-spaced inter-band signals such as needed in 4G carrier aggregated systems. This solution embeds a signal-amplitude estimator which provides the amount of clipping to apply to the instantaneous samples of the different carriers that constitute an inter-band carrier aggregated signal. Hence, the resulting CFR runs at a sampling rate proportional only to the bandwidth of the constituent carriers and is not impacted by the frequency spacing between the carriers. This allows for a significant decrease in computational complexity and power overhead associated with classical multi-band CFR techniques that need to operate at much higher rates.
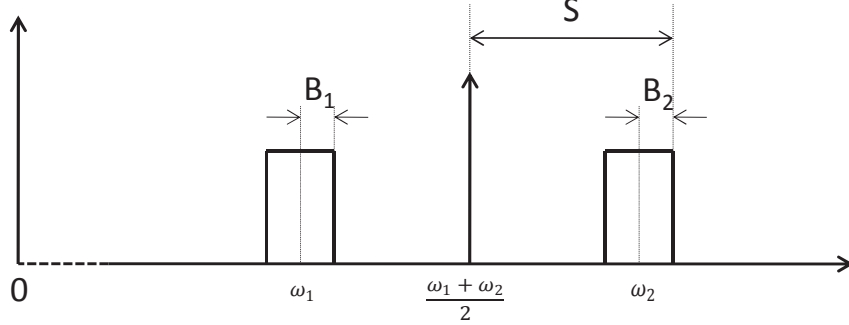
Figure 3.1: Carrier aggregated signals over two spaced bands

3.1 Challenges of SISO CFR for Carrier Aggregated Signals

For simplicity purposes, in this section, the following study is conducted for the number of bands equal to two; in subsequent sections, the technique will be extended to arbitrary numbers of bands. A carrier aggregated signal over two bands, $x(t)$, , as the one shown in Fig. 3.1, can be expressed as

$$
\begin{aligned}
x(t) &= x_1(t) + x_2(t) \\
&= Re\left(\widetilde{x}_1(t)e^{(j\omega_1 t)} + \widetilde{x}_2(t)e^{(j\omega_2 t)}\right)
\end{aligned}
$$

where $x_1(t)$ and $x_2(t)$ are the mixed mode signals in each band, $\widetilde{x}_1(t)$ and $\widetilde{x}_2(t)$ denote the baseband envelopes of $x_1(t)$ and $x_2(t)$ around the angular frequencies ω_1 and ω_2, respectively. The carrier aggregated signal can be represented as a broadband signal with an angular carrier frequency $((\omega_1 + \omega_2)/2)$ as given by:

$$
\begin{aligned}
x(t) &= Re\left(\widetilde{x}(t) \cdot e^{\left(j\frac{(\omega_1+\omega_2)}{2}t\right)}\right) \\
&= Re\left(\left(\widetilde{x}_1(t)e^{\left(j\frac{(\omega_1-\omega_2)}{2}t\right)} + \widetilde{x}_2(t)e^{\left(j\frac{(\omega_2-\omega_1)}{2}t\right)}\right) e^{\left(j\frac{(\omega_1+\omega_2)}{2}t\right)}\right)
\end{aligned}
\tag{3.1}
$$

where $\widetilde{x}(t)$ is the baseband envelope of the carrier aggregated signal given by

$$
\widetilde{x}(t) = \widetilde{x}_1(t)e^{\left(j\frac{(\omega_1-\omega_2)}{2}t\right)} + \widetilde{x}_2(t)e^{\left(j\frac{(\omega_2-\omega_1)}{2}t\right)}.
$$

$x(t)$ can be amplified using a dual-band or broadband PA instead of two single-band

21

PAs in order to reduce a transmitter's costs and size. The carrier aggregation can result in an increased CF, which unless reduced, will require the designer to operate the dual-band PA in its large back-off region, inefficiently. The classical clipping/windowing nonlinear CFR technique can be applied to $\widetilde{x}(t)$. In such case the CFR module would be a single-input single-output (SISO) unit that processes a digitized version of $\widetilde{x}(t)$ which is sampled at a frequency f'_s, where $f'_s \geq 2 \cdot (S + max(B_1/2, B_2/2))$, and S , B_1 and B_2 represent the frequency spacing and the bandwidths of the two signals respectively. The digitized baseband signal $\widetilde{x}(n')$ can then be expressed as follows:

$$\widetilde{x}(n') = \widetilde{x}_1(n')e^{\left(j\frac{(\omega_1 - \omega_2)}{2}\frac{n'}{f'_s}\right)} + \widetilde{x}_2(n')e^{\left(j\frac{(\omega_2 - \omega_1)}{2}\frac{n'}{f'_s}\right)}.$$

The frequency spacing S is generally significantly greater than the bandwidths of $x_1(t)$ and $x_2(t)$, i.e. B_1 and B_2, especially in the case of inter-band aggregation scenarios. Hence, f'_s would need to be considerably larger than f_{s1} and f_{s2}, needed to digitize $\widetilde{x}_1(t)$ and $\widetilde{x}_2(t)$, respectively ($f_{s1} \geq 2 \cdot B_1$, $f_{s2} \geq 2 \cdot B_2$). As an example, assume a carrier aggregated signal is composed of a 15 MHz WCDMA signal around 2.1 GHz and a 10 MHz LTE signal centered in 2.4 GHz. The minimum theoretical sampling rate f'_s must therefore be higher than 610 $Msps$. This sampling rate is significantly higher than the one needed to represent the WCDMA and LTE signals themselves. The direct application of the SISO clipping/windowing to $\widetilde{x}(n')$ is thus seen to imply a high and unpractical sampling rate. To address this limitation, a new dual-input dual-output (DIDO) nonlinear CFR technique suitable for carrier aggregated signals over two bands will now be introduced in the following section.

3.2   Proposed CFR Techniques

The classical clipping/windowing method consists of monitoring the instantaneous amplitude of the signal envelope, and limiting it to a preset threshold to obtain the targeted CF, as shown in Fig. 3.2(a). As can be seen, in addition to the clipping and filtering modules, the SISO CFR includes an up-sampler, a digital up-converter, a down-sampler and a down-converter. As this technique is a nonlinear operation, in-band distortions and out of band spectrum regrowth are induced. In order to meet the mask requirement in terms of ACLR, the clipped signal needs to be filtered. The clipping threshold is set so that the CF is reduced while respecting the EVM and ACLR specifications. The high sampling rate requirement associated with the conventional clipping and windowing approach makes this solution sub-optimal in the context of inter-band carrier aggregated signals.
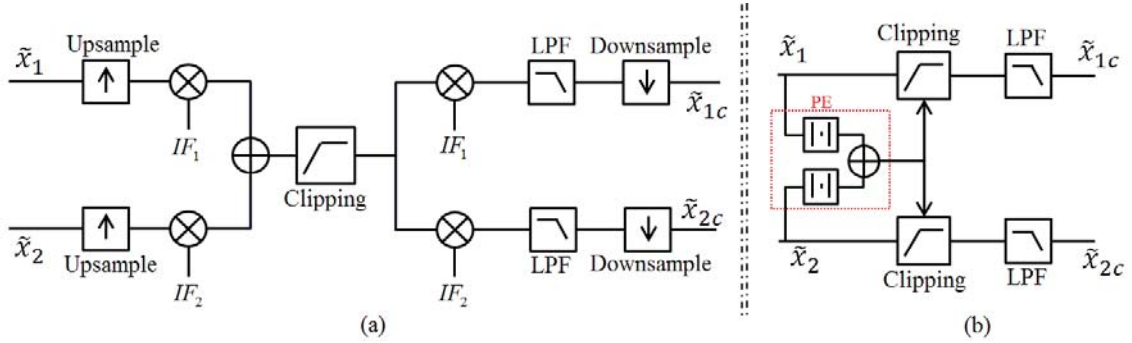
Figure 3.2: Conventional (a) vs. proposed (b) crest factor reduction technique

3.2.1   2CC-CFR

In the new proposed DIDO CFR technique, shown in Fig. 3.2(b), a peak estimator (PE) is created and embedded to compute the instantaneous amplitude of the carrier aggregated signal using the baseband signals of the two carriers as a first step of the CFR process. First, the envelope of the carrier aggregated signal expression given in 3.1 can be rewritten as follows:

$$\widetilde{x}(t) = |\widetilde{x}_1(t)|e^{j\left(\frac{\omega_1-\omega_2}{2}t+\varphi_1(t)\right)} + |\widetilde{x}_2(t)|e^{j\left(\frac{\omega_2-\omega_1}{2}t+\varphi_2(t)\right)} \tag{3.2}$$

where $\varphi_1(t)$ and $\varphi_2(t)$ are the instantaneous phase of $\widetilde{x}_1(t)$ and $\widetilde{x}_2(t)$, respectively. The terms $\left(\frac{\omega_1-\omega_2}{2}t\right)$ and $\left(\frac{\omega_2-\omega_1}{2}t\right)$ imply additional phase difference between $\widetilde{x}_1(t)$ and $\widetilde{x}_2(t)$, which occurs at much higher speed than $\varphi_1(t)$ and $\varphi_2(t)$. In fact, the two terms in the right side of 3.2 can be in-phase at a given instant t_0 before both baseband envelopes evolve noticeably, i.e. $e^{j\left(\frac{\omega_1-\omega_2}{2}t_0+\varphi_1(t_0)\right)} = e^{j\left(\frac{\omega_2-\omega_1}{2}t_0+\varphi_2(t_0)\right)} = e^{(j\varphi_0(t_0))}$. At instant t_0, the carrier aggregated signal envelope is given by

$$\widetilde{x}(t_0) = \left(|\widetilde{x}_1(t_0)| + |\widetilde{x}_2(t_0)|\right)e^{(j\varphi_0(t_0))}.$$

Hence, the carrier aggregation process yields an instantaneous full constructive addition even if the two carriers' envelopes are out of phase, i.e. $|\widetilde{x}(t_0)| = \left(|\widetilde{x}_1(t_0)| + |\widetilde{x}_2(t_0)|\right)$. The envelope of the carrier aggregated signal is therefore given by

$$PE\left(\widetilde{x}(t)\right) \cong |\widetilde{x}_1(t)| + |\widetilde{x}_2(t)| \tag{3.3}$$

Note that the triangular inequality of complex numbers ensures that the PE given will never exceed the real value of the dual-band envelope $|\widetilde{x}(t)|$.

$$|\widetilde{x}(t)|^2 = \left|\widetilde{x}_1(t)e^{\left(j\frac{(\omega_1-\omega_2)}{2}t\right)} + \widetilde{x}_2(t)e^{\left(j\frac{(\omega_2-\omega_1)}{2}t\right)}\right|$$

$$\leqslant \left(|\widetilde{x}_1(t)| + |\widetilde{x}_2(t)|\right)^2$$

$$= \left(PE\left(\widetilde{x}(t)\right)\right)^2$$

In other words, the triangular approximation ensures that the proposed 2CC-CFR based on the proposed PE will always guarantee a signal within the targeted PAPR. The proposed derivations given in (3.2-3.3) prove that, given the large frequency spacing between the two carriers forming the carrier aggregated signal, the two component carrier envelopes, $\widetilde{x}_1(t)$ and $\widetilde{x}_2(t)$, will always vectorially combine and reach a maximum magnitude at a given instant, t_0, despite their potentially random phases. This proves that the PE computes the upper bound of the dual-band envelope $|\widetilde{x}(t)|$ and has the advantage of requiring a low sampling rate.

As a result, the CF of the carrier aggregated signal can be estimated by monitoring the magnitude of the two carriers' baseband signals. Furthermore, 3.3 suggests that the envelope of $\widetilde{x}(t)$ can be obtained using the envelopes of $\widetilde{x}_1(t)$ and $\widetilde{x}_2(t)$ sampled at a rate $f_s = max\left(f_{s1},\ f_{s2}\right)$.

$$PE\left(\widetilde{x}(n)\right) \cong \left(|\widetilde{x}_1(n)| + |\widetilde{x}_2(n)|\right).$$

For illustration purpose, two sine waves were combined and the resulting signal is analyzed. According to Fig. 3.3, the summation of the two magnitudes of the two signals provided a good estimate of the carrier aggregated signal's envelope.

Given an arbitrary clipping threshold, C, and a carrier aggregate signal peak estimate of $S(n)$, $S(n) = |\widetilde{x}_1(n)| + |\widetilde{x}_2(n)|$, where $\widetilde{x}_1(n)$ and $\widetilde{x}_2(n)$ are the envelopes of the two CCs, a CFR can be implemented by subtracting $(S(n) - C)/2$ from the two CCs, as given in 3.4.

$$If\ S(n) = |\widetilde{x}_1(n)| + |\widetilde{x}_2(n)| > C$$
$$\Rightarrow \begin{cases} |\widetilde{x}_{1\_clipped}(n)| & = |\widetilde{x}_1(n)| - (S(n) - C)/2 \\ |\widetilde{x}_{2\_clipped}(n)| & = |\widetilde{x}_2(n)| - (S(n) - C)/2 \end{cases} \qquad (3.4)$$

The CFR of 3.4 is referenced hereafter as 2CC-CFR with equal peak reduction applied to both CCs. Alternatively, the two CCs can be clipped proportionally to their contribution to the peak estimate, $S(n)$, as given in 3.5.
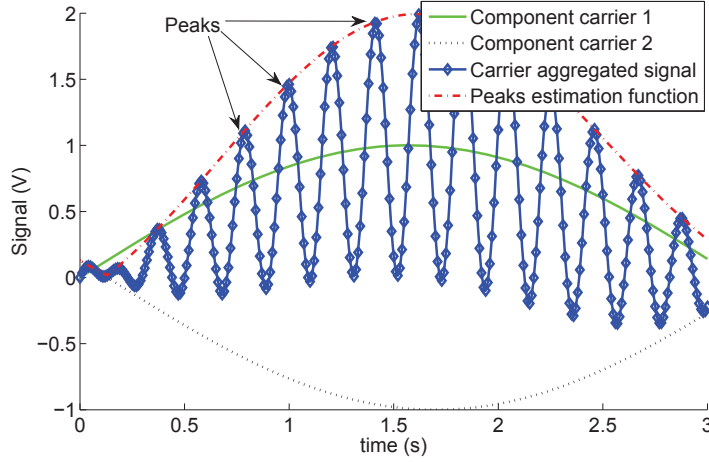
Figure 3.3: Envelop of carrier aggregated signal

$$If \ |\widetilde{x}_1(n)| + |\widetilde{x}_2(n)| > C$$
$$\Rightarrow \begin{cases} |\widetilde{x}_{1\_clipped}(n)| & = \frac{|\widetilde{x}_1(n)|}{(|\widetilde{x}_1(n)|+|\widetilde{x}_2(n)|)}C \\ |\widetilde{x}_{2\_clipped}(n)| & = \frac{|\widetilde{x}_2(n)|}{(|\widetilde{x}_1(n)|+|\widetilde{x}_2(n)|)}C \end{cases} \tag{3.5}$$

The CFR of 3.5 is referenced hereafter as 2CC-CFR with proportional peak reduction method.

3.2.2   2CC-CFR with Unequal Power Levels

The average power of each CC of a two CC aggregated signal can be significantly different in order to accommodate the radio link requirements. In such a case, the 2CC-CFR of 3.4 or 3.5 will be inadequate as the PE must consider the average power difference between the two bands. To ensure that an adequate clipping factor is applied to each of the CCs' envelopes, the 2CC-CFR of 3.4 or 3.5 should be applied to the scaled envelope signals, $G_1 \cdot |\widetilde{x}_1(n)|$ and $G_1 \cdot |\widetilde{x}_1(n)|$. The scaling factors are expressed as follows:

$$G_1 = \sqrt{\frac{P_1}{mean(|\widetilde{x}_1(n)|^2/100)}}; \ G_2 = \sqrt{\frac{P_2}{mean(|\widetilde{x}_2(n)|^2/100)}}$$

where P_1 and P_2 represent the average power levels of the two CCs. The PE of the carrier aggregated signal and the 2CC-CFR with unequal power levels can be implemented as follows:

$$If \ (G_1 \cdot |\widetilde{x}_1(n)| + G_2 \cdot |\widetilde{x}_2(n)|) > C$$
$$\Rightarrow \begin{cases} |\widetilde{x}_{1\_clipped}(n)| & = \frac{G_1 \cdot |\widetilde{x}_1(n)|}{(G_1 \cdot |\widetilde{x}_1(n)| + G_2 \cdot |\widetilde{x}_2(n)|)}C \\ |\widetilde{x}_{2\_clipped}(n)| & = \frac{G_2 \cdot |\widetilde{x}_2(n)|}{(G_1 \cdot |\widetilde{x}_1(n)| + G_2 \cdot |\widetilde{x}_2(n)|)}C \end{cases} \quad (3.6)$$

Note that in the case of equal power levels for the two bands, 3.6 could be simplified to 3.5.

3.2.3   2CC-CFR with Different EVM Requirements

In some carrier aggregation scenarios, different CCs may have different modulation schemes that impose different EVM requirements. One example is a carrier aggregated signal formed by a quadrature phase shift keying (QPSK) signal and a 64 quadrature amplitude modulated (64 QAM) signal. As per [1], the maximum tolerable EVM distortion is 17.5 % for the former signal and 8% for the latter. The 2CC-CFR solution in 3.4 applies the same peak reduction factor to both CCs, whereas the 2CC-CFR solution in 3.5 does not adapt to the signals' EVM requirements but to their contribution to the aggregated peak. Hence, in both methods 3.4 and 3.5, the clipping margin is limited by the lower EVM bound (8 % in this example). A better approach is to exploit the extra EVM margin offered by the simpler modulation scheme through unequal peak reduction factors, as given by 3.7.

$$If \ S(n) = |\widetilde{x}_1(n)| + |\widetilde{x}_2(n)| > C$$
$$\Rightarrow \begin{cases} |\widetilde{x}_{1\_clipped}(n)| & = |\widetilde{x}_1(n)| - \alpha_1 \cdot (S(n) - C)/2 \\ |\widetilde{x}_{2\_clipped}(n)| & = |\widetilde{x}_2(n)| - \alpha_2 \cdot (S(n) - C)/2 \end{cases} \quad (3.7)$$

In 3.7, α_1 and α_2 are the two peak reduction factors which satisfy the condition $\alpha_1 + \alpha_2 = 1$. Note that in 3.7, the computation of the peak reduced envelopes, $\widetilde{x}_{1\_clipped}(n)$ and $\widetilde{x}_{2\_clipped}(n)$ involves both α_1 and α_2, however, the PE remains the same as in 3.5, in other words α_1 and α_2 are not needed for the peak estimation. The values of α_1 and α_2 are jointly varied until the two EVM requirements are met.

3.2.4   MCC-CFR

A carrier aggregated signal over multi-bands is given by:

$$x(t) = \sum_{i=1}^{N} x_i(t) = Re\left(\sum_{i=1}^{N} \widetilde{x}_i(t)e^{(j\omega_i t)}\right),$$

where N is the number of carrier aggregated bands, $x(t)$ is the carrier aggregated signal, $x_i(t)$ is the mixed mode signals in the ith band, $\tilde{x}_i(t)$ denotes the baseband envelopes of $x_i(t)$ around the angular frequency ω_i.

In order to clip the signal $x(t)$ using the conventional way, it should be modeled as one envelop signal around a carrier angular frequency ω_0 given by middle point of the two spectrum extremes

$$\omega_0 = \frac{1}{2}\left(max\left(\omega_i\,,\,i = 1\cdots N\right) + min\left(\omega_i\,,\,i = 1\cdots N\right)\right)$$

In this case, sampling rate of the signal should be

$$f_s' \geq 2\cdot\left(S + max\left(\frac{B_i}{2}\right)\right)$$

where f_s' is the required sampling rate for the mixed signal,

$$S = \frac{1}{2\cdot\pi}\left(max\left(\omega_i,\,i = 1\cdots N\right) - min\left(\omega_i,\,i = 1\cdots N\right)\right)$$

and B_i is the bandwidth of signal $\tilde{x}_i(t)$. Alternatively, using similar proof to section 3.2, it can be shown that,

$$envelop\left(\sum_{i=1}^{N}\tilde{x}_i(t)e^{(j\omega_i t)}\right) \cong |\sum_{i=1}^{N}\tilde{x}_i(t)|.$$

As a result, the CF of the carrier aggregated signal can be estimated by monitoring the magnitude of the different carriers' baseband signals. The envelope of $\tilde{x}(t)$ can be obtained using the envelopes of $\tilde{x}_i(t)$ sampled at a rate

$$f_s = max\left(f_{s_i} = \frac{1}{B_i}; i = 1..N\right),$$

where B_i is the bandwidth of signal $\left|\tilde{x}_i(t)\right|$. Hence, given an arbitrary clipping threshold C, the CFR of carrier aggregated signal can be obtained by clipping each carrier baseband signal as follows:

$$\begin{cases}\forall k \in \{1..N\}, & If\ \sum_{i=1}^{N}\tilde{x}_i(t) > C \\ |\tilde{x}_{k\_clipped}(n)| & = \frac{|\tilde{x}_k(n)|}{\sum_{i=1}^{N}\tilde{x}_i(t)}C\end{cases} \tag{3.8}$$

For the case of tri-band signal, the 3CC-CFR is implemented as per 3.9

$$If \ (|\widetilde{x}_1(n)| + |\widetilde{x}_2(n)| + |\widetilde{x}_3(n)|) > C$$

$$\Rightarrow \begin{cases} |\widetilde{x}_{1\_clipped}(n)| & = \frac{|\widetilde{x}_1(n)|}{(|\widetilde{x}_1(n)|+|\widetilde{x}_2(n)|+|\widetilde{x}_3(n)|)}C \\ |\widetilde{x}_{2\_clipped}(n)| & = \frac{|\widetilde{x}_2(n)|}{(|\widetilde{x}_1(n)|+|\widetilde{x}_2(n)|+|\widetilde{x}_3(n)|)}C \\ |\widetilde{x}_{2\_clipped}(n)| & = \frac{|\widetilde{x}_3(n)|}{(|\widetilde{x}_1(n)|+|\widetilde{x}_2(n)|+|\widetilde{x}_3(n)|)}C \end{cases} \tag{3.9}$$

3.3 Experimental Validation

In this section the performance of the proposed CFR techniques are assessed and compared to the conventional SISO CFR one. Three clipping scenarios are presented in the following sub-sections.

3.3.1 2CC-CFR

An inter-band carrier aggregated signal was synthesized, composed of a $10\,MHz$ 2C WCDMA signal and a 15 MHz LTE signal, separated by $300\,MHz$. Both the 2CC-CFR and the conventional CFR approaches were applied to the synthesized carrier aggregated signal. The SISO CFR technique was carried out at a sampling rate equal to $f'_s = 610\,Msps$. Next, the 2CC-CFR technique was applied to the two separate baseband components and was performed at a sampling rate equal to $f_s = 92.16\,Msps$. EVM performance of the two approaches vs. targeted PAPR is shown in Fig. 3.4 and spectrum regrowth due to the nonlinear clipping operation is shown in Fig. 3.5.
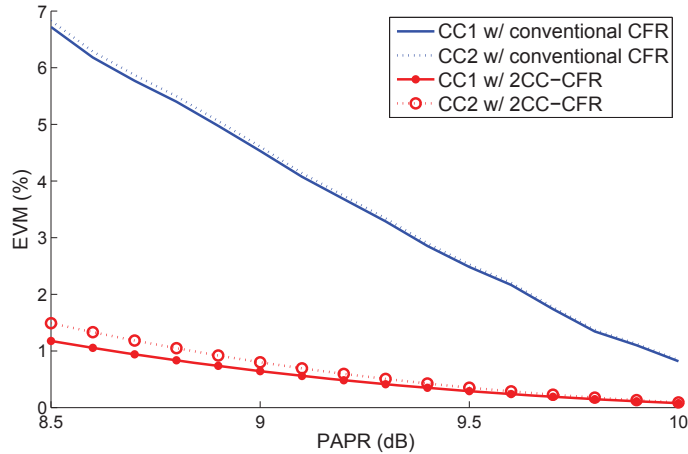
Figure 3.4: EVM of 2CC-CFR versus conventional CFR of 300 MHz dual-band signal

Table 3.1: PAPR and EVM of original and peak reduced signals - 2CC-CFR with equal power levels

	Signal	PAPR (dB)	EVM (%)	ACLR (dBc)
Original signal	2C WCDMA @ band 1	7.9	0	68
	LTE15 @ band 2	9.2	0	65
	Frequency aggregated	10.5		
Clipped signal	2C WCDMA @ band 1	7.9	0.6	48
	LTE15 @ band 2	9.2	0.8	50
	Frequency aggregated	9		
Clipped & filtered signal	2C WCDMA @ band 1	7.9	1.3	68
	LTE15 @ band 2	9.2	1.3	65
	Frequency aggregated	9.1		
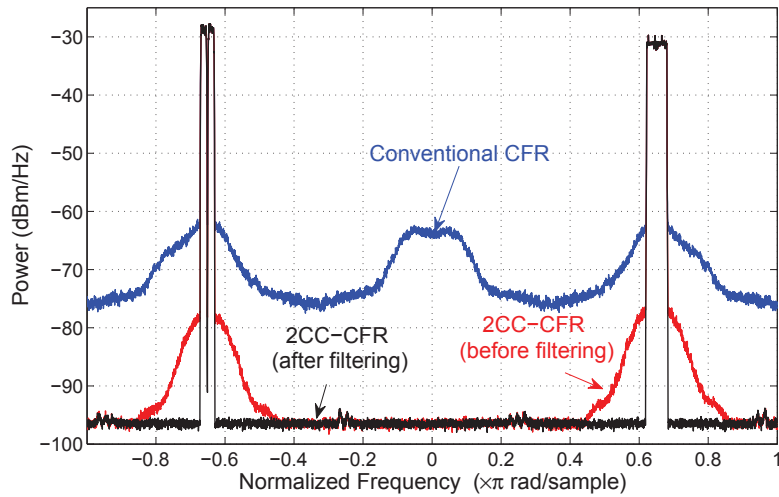
Figure 3.5: Simulated spectrum of 2CC-CFR versus conventional CFR of 300 MHz dual-band signal

In order to remove the out of band spectrum regrowth attributed to the 2CC-CFR (red curve in Fig. 3.5), the clipped signal is filtered as commonly known by filtering/windowing process [7]. Filtering result is given by the black curve in Fig. 3.5. It is noted that the filtering result is not applied to the SISO CFR due to its poor performance as explained later. Table 3.1 summarizes the original signal characteristics and the results of the 2CC-CFR with and without filtering. The PAPR of the original frequency aggregated signal is decreased from 10.5 dB to 9 dB with around 0.7% EVM distortion and 15 to 20 dB spectrum regrowth. The clipping/windowing iterations enabled the removal of the spectrum regrowth at the cost of increasing the EVM to 1.3 %, which is still acceptable by different modulation schemes [1].

Table 3.2: PAPR and EVM of original and Peak Reduced Signals - 2CC-CFR with equal power levels

	Signal	PAPR (dB)	EVM (%)	ACLR (dBc)
Original signal	2C WCDMA @ band 1	7.9	0	68
	LTE15 @ band 2	9.2	0	65
	Frequency aggregated	10.5		
Clipped signal	2C WCDMA @ band 1	7.9	0.9	45
	LTE15 @ band 2	9.2	1.1	48
	Frequency aggregated	9		
Clipped & filtered signal	2C WCDMA @ band 1	7.9	1.3	68
	LTE15 @ band 2	9.2	1.4	65
	Frequency aggregated	9.1		

Concerning the SISO CFR performance, in addition to its high sampling rate, it is shown in Fig. 3.4 and Fig. 3.5 that EVM and spectrum regrowth is significantly poor when compared to the 2CC-CFR case (blue vs red curves). In order to explain the reason, the two signals separation is lowered to 60 MHz and the same analysis is repeated. The EVM performance of the two approaches vs. targeted PAPR is shown in Fig. 3.6 and spectrum regrowth due to the nonlinear clipping operation is shown in Fig. 3.7 and the original, clipped, clipped and filtered signals characteristics are shown in Table 3.2. Although the results are comparable with the high frequency separation case, the spectrum plot of the SISO CFR signal in Fig. 3.7 (blue curve) reveals the existence of inter-modulation distortion components due to the nonlinear clipping operation acting on the two signals simultaneously, unlike the 2CC-CFR case where each signal is clipped separately. Hence, the SISO technique is more prone to generate more distortion, both in-band and out of band.
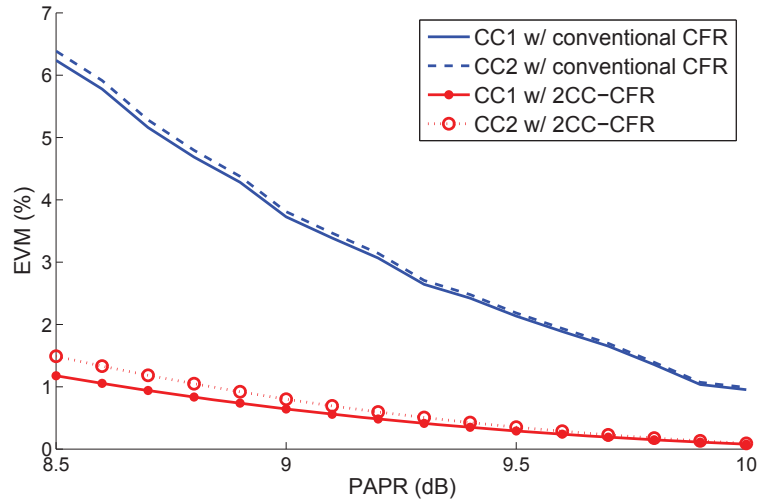
Figure 3.6: EVM of 2CC-CFR versus conventional CFR of a 60 MHz dual-band signal
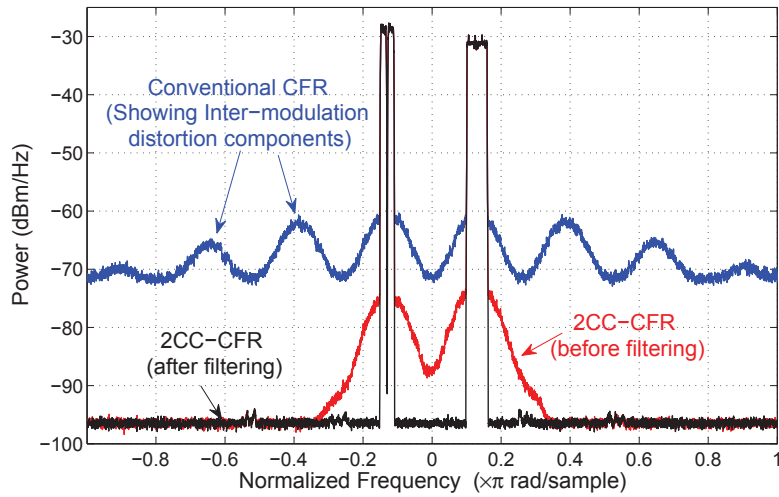
Figure 3.7: Simulated spectrum of 2CC-CFR versus conventional CFR of a 60 MHz dual-band signal

3.3.2 2CC-CFR with Unequal Power Levels

A test signal composed of the same CCs chosen in the previous sub-section is reused in this scenario. However, in this case, the two CC signals were assigned unequal average powers (the second CC's average power was set to be 10 dB higher than the first CC). Both the 2CC-CFR of 3.6 for carriers with unequal power levels, and the conventional CFR approach, were applied to the synthesized carrier aggregated signal. The conventional CFR technique was carried out at a sampling rate equal to $f'_s = 610\,Msps$. Next, the proposed CFR technique was applied to the two separate CCs and was performed at a sampling rate equal to $f_s = 92.16\,Msps$. The clipping/windowing iterations applied to the proposed 2CC-CFR enabled the removal of the spectrum regrowth engendered by the nonlinear clipping operation at the targeted CF. EVM performance of the two approaches versus the targeted CF is shown in Fig. 3.8 and spectrum regrowth due to the nonlinear clipping operation is shown in Fig. 3.9.

Table 3.3 summarizes the original signal characteristics and the results of the CFR with and without filtering. The CF of the original frequency aggregated signal was decreased from 9.9 dB to 7.9 dB with around 1.7 % and 2.7 % EVM distortion, and -50 dBc and -55 dBc ACLR for the first and second bands, respectively. It was found that the second band was slightly more distorted than the first band (1 % higher EVM and 5 dB higher ACLR). However, in the case of the conventional CFR, shown in Fig. 3.9, the first CC was severely distorted as compared to the second CC with 20 % more EVM distortion and 10 dB more ACLR distortion (-15 dBc and -25 dBc ACLR for band 1 and band 2, respectively).

Table 3.3: PAPR and EVM of original and peak reduced signals - carriers with unequal power levels

	Signal	PAPR (dB)	EVM (%)	ACLR (dBc)
	2C WCDMA @ band 1	7.9	0	-68
Original signal	LTE15 @ band 2	9.2	0	-65
	Frequency aggregated	9.9		
	2C WCDMA @ band 1	7.9	1.7	-50
Clipped signal	LTE15 @ band 2	9.2	2.7	-55
	Frequency aggregated	7.9		
	2C WCDMA @ band 1	7.9	1.8	-68
Clipped & filtered signal	LTE15 @ band 2	9.2	2.8	-65
	Frequency aggregated	8		
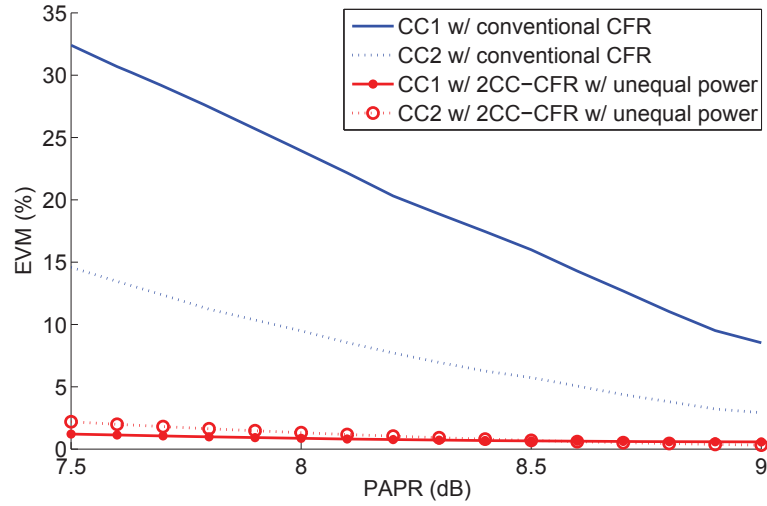
Figure 3.8: EVM of the 2CC-CFR – carriers with unequal power levels versus conventional CFR
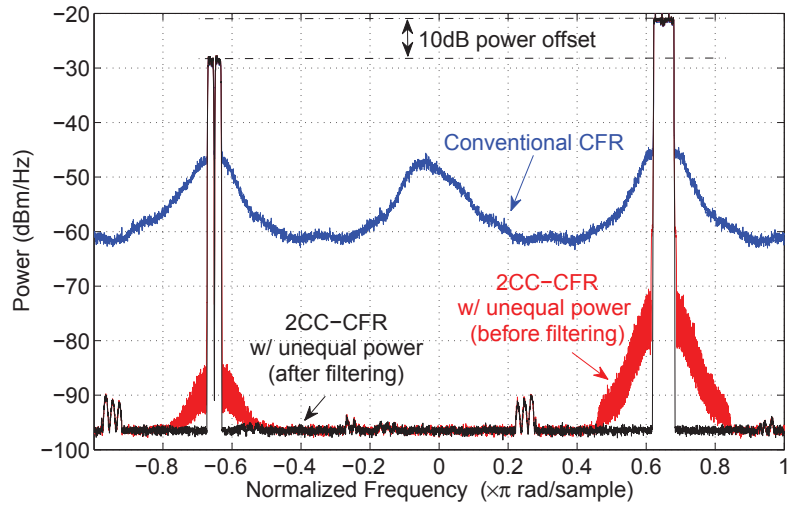
Figure 3.9: Simulated spectrum of the 2CC-CFR – carriers with unequal power levels versus conventional CFR

3.3.3   2CC-CFR with Different EVM Requirements

A carrier aggregated signal composed of a 15 MHz LTE 64 QAM signal and a 15 MHz LTE QPSK signal, separated by 300 MHz was synthesized. The EVM specification for the 64 QAM signal was 8% and for the QPSK signal was 17.5%. Both the CFR for carriers with equal EVM requirements of 3.4, and the CFR for carriers with different EVM requirements of 3.7, were applied to the synthesized carrier aggregated signal. Both 2CC-CFR techniques were applied to the two separate CCs and were performed at a sampling rate equal to $f_s = 92.16\,Msps$. In total, 4 clipping/windowing iterations were applied to enable the removal of the spectrum regrowth engendered by the nonlinear clipping operation at the targeted CF. EVM performance of the two approaches versus targeted CF is shown in Fig. 3.10 and spectrum regrowth due to the nonlinear clipping operation is shown in Fig. 3.11.

Table 3.4 summarizes the original, peak reduced and filtered signal characteristics of the proposed CFR for CCs with different EVM requirements. The CF of the original frequency aggregated signal was decreased from 11.8 dB to 9.05 dB with around 1.4 % and 3.2 % EVM distortion for the first and second bands, respectively, and -67 dBc ACLR for the two CCs. It is shown that that the QPSK signal was more distorted than the 64 QAM signal (2 % higher EVM and 7 dB higher ACLR before filtering). However, in the case of the 2CC-CFR of 3.4 with equal EVM requirements (blue curves in Fig. 10), the two bands were equally distorted with about -36 dBc ACLR distortion and the possible peak reduction was limited by the 64 QAM signal requirements.
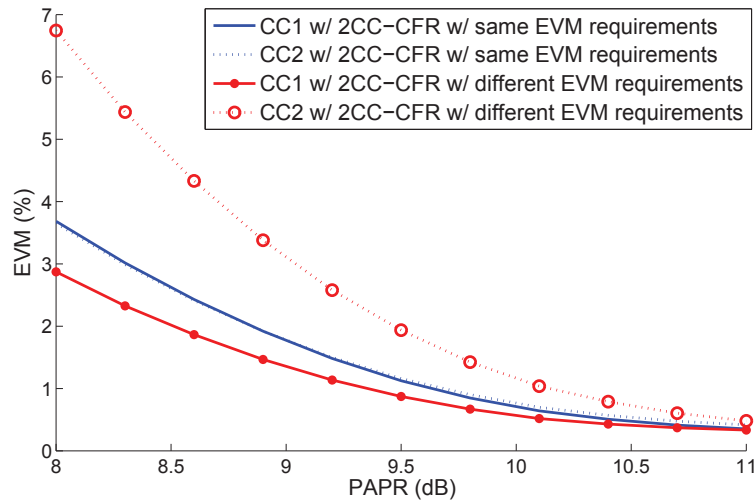
Figure 3.10: EVM of the 2CC-CFR – carriers with different EVM requirements versus conventional CFR
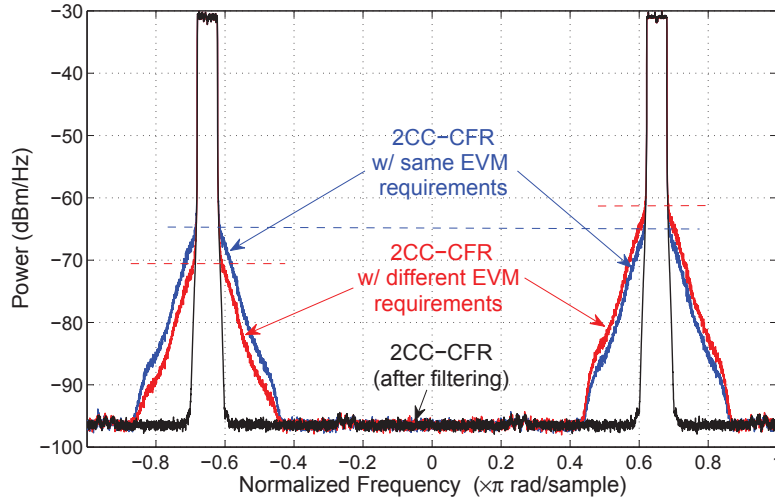
Figure 3.11: Simulated spectrum of the 2CC-CFR – carriers with different EVM requirements versus conventional CFR

Table 3.4: PAPR and EVM of original and peak reduced signals - carriers with different EVM requirements

	Signal	PAPR (dB)	EVM (%)	ACLR (dBc)
	64QAM LTE @ band 1	11.2	0	-67
Original signal	QPSK LTE @ band 1	10.9	0	-67
	Frequency aggregated	11.8		
	64QAM LTE @ band 1	11	1.4	-33
Clipped signal	QPSK LTE @ band 1	10.7	3.2	-40
	Frequency aggregated	9		
	64QAM LTE @ band 1z	11.1	1.4	-67
Clipped & filtered signal	QPSK LTE @ band 1	10.8	3.2	-67
	Frequency aggregated	9.05		

3.3.4 3CC-CFR

An inter-band carrier aggregated signal was synthesized, composed of a 15 MHz LTE signal, 20 MHz WCDMA signal and 5 MHz LTE signal. The first and second signals are separated by 100 MHz. The second and third signals are separated by 100 MHz too. Hence, the overall signal separation is 200 MHz. Both the 3CC-CFR and SISO CFR approaches were applied to the synthesized carrier aggregated signal. The SISO CFR technique was carried out at a sampling rate equal to $f_s' = 420\,Msps$. Next, the 3CC-CFR technique was applied to the two separate baseband components and was performed at a sampling rate equal to $f_s = 92.16\,Msps$. EVM performance of the two approaches vs. targeted PAPR is shown in Fig. 3.12 and spectrum regrowth due to the nonlinear clipping operation is shown in Fig. 3.13. The original and clipped signals characteristics are summarized in Table 3.5. It is shown that the tri-band CFR has outperformed the SISO CFR for the same reason detailed in the previous sub-section.
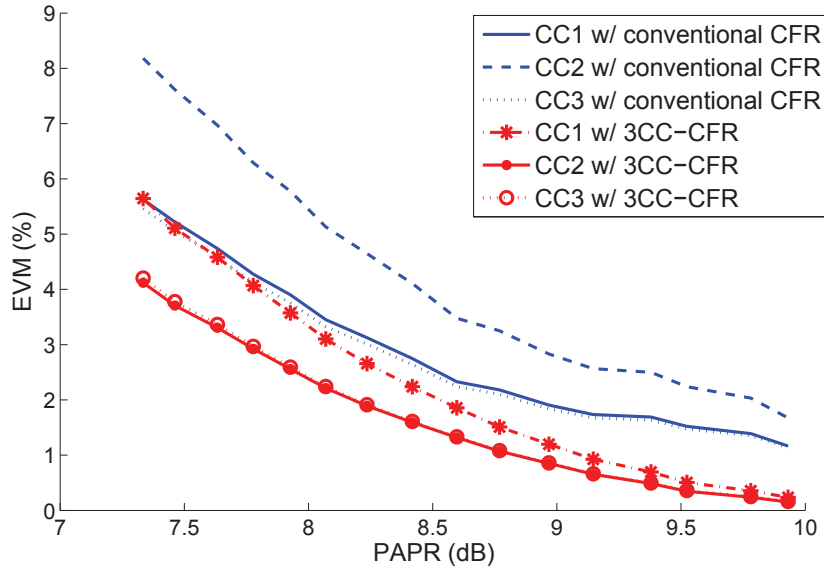
Figure 3.12: EVM of 3CC-CFR versus conventional CFR in the case of three CCs
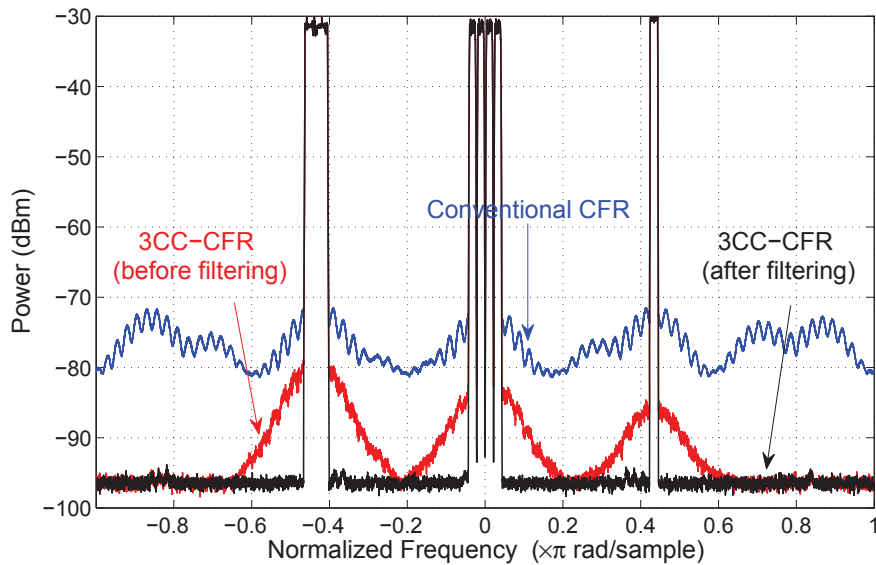
Figure 3.13: Simulated spectrum of 3CC-CFR versus conventional CFR in the case of three CCs

Table 3.5: PAPR and EVM of original and peak reduced signals − 3CC-CFR case

	Signal	PAPR (dB)	EVM (%)	ACLR (dBc)
Original signal	LTE15 @ band 2	9.2	0	65
	4C WCDMA @ band 1	9	0	65
	LTE5 @ band 3	9.1	0	65
	Frequency aggregated	11.3		
Clipped signal	LTE15 @ band 2	9.2	0.6	48
	4C WCDMA @ band 1	9	0.7	51
	LTE5 @ band 3	9.1	0.5	50
	Frequency aggregated	9.4		
Clipped & filtered signal	LTE15 @ band 2	9.2	1.3	65
	4C WCDMA @ band 1	9	1.4	65
	LTE5 @ band 3	9.1	1.7	65
	Frequency aggregated	9.5		

As an application for the proposed technique, the output signal of the CFR was applied to two power amplifiers, a 45 W gallium nitride (GaN) single ended PA and a 250 W laterally diffused metal oxide semiconductor (LDMOS) Doherty PA. Hence, using the threshold of 2% as a maximum tolerable EVM, the tri-band CFR allowed for about 2 dB reduction in PAPR while the SISO approach was limited to a 0.5 dB reduction in PAPR. Efficiency results are reported in Table 3.6. It is shown that the achieved CFR on the test signal allows for significant improvement of the effective average power level by about 2 dB, and an increase in power efficiency, by up to 5%, when the test signal is applied to two amplifiers under test.

Table 3.6: Effective power and efficiency increase of 2CC-CFR

	PAPR (dB)	EVM(%) Band 1	EVM(%) Band 2	EVM(%) Band 3	Effective average power	Efficiency (%)
Single ended PA	11.3	0	0	0		16
	9.5	1.3	1.4	1.7	$+2$	20
Doherty PA	10.3	0	0	0		40
	8.6	1.3	1.4	1.7	$+2$	45

Chapter 4

Digital PreDistortion of Multi-band Power Amplifiers

Two RF PA modeling approaches exist in the literature [16]. The first approach approximates the behavior of the PA using its pass band input and output signals. The inherent complexity associated with this approach has limited the pass band model's adoption in the area of RF PA modeling and linearization. Instead, the LPE modeling approach is preferred [22]. It is applied to the complex envelope of the RF input/output signals and requires much simpler measurement hardware and reduced computation as compared to its pass band counterpart. In fact, the LPE modeling approach capitalizes on the band limited characteristics of communication signals, thus limiting approximation efforts to the PA distortions which affect the signal envelope around the carrier frequency. Essentially, the PA is treated as an envelope processing system [16]. Therefore, if the real RF PA behavior is expressed as 4.1:

$$y(t) = f(x(t)), \tag{4.1}$$

where $x(t)$ is the real RF input signal, $y(t)$ is the real RF output signal and f is a describing function (modeling the RF PA behavior), then the LPE methodology, as shown in Fig. 4.1, consists of modeling the equivalent envelope behavior of the PA. This is illustrated in 4.2

$$\widetilde{y}(n) = \widetilde{f}(\widetilde{x}(n)), \tag{4.2}$$

where $\widetilde{x}(n)$ and $\widetilde{y}(n)$ denote the envelopes of the input and output signals, respectively, around the carrier and $\widetilde{f}$ designates the LPE model.

Since a PA can be treated as a nonlinear dynamic system with fading memory, the Volterra series outlined in 4.3 is a very suitable modeling framework to approximate its behavior and/or synthesize the corresponding predistortion module [19].
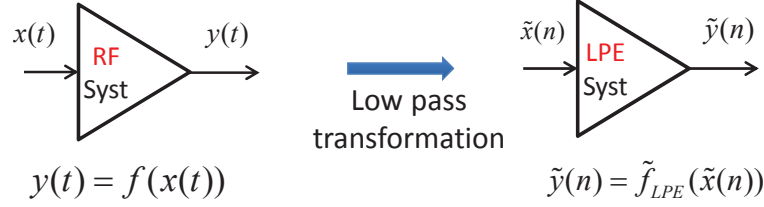
Figure 4.1: Classical low pass equivalent modeling approach

$$y(t) = \sum_{p=1}^{NL} \int_{-\infty}^{\infty} \cdots \int_{-\infty}^{\infty} h_p\big(\tau_1, \cdots, \tau_p\big) \cdot \prod_{j=1}^{p} x(t - \tau_j) d\tau. \tag{4.3}$$

In this model, $x(t)$ and $y(t)$ designate the input and output RF pass band signals respectively, and h_p denotes the Volterra series' kernels. The direct application of the LPE strategy to the discrete input and output signals' envelopes yields the expression 4.4 which is commonly used for RF PA behavioral modeling.

$$\widetilde{y}(n) = \sum_{p=1;p=p+2}^{NL} \sum_{i_1=0}^{M} \cdots \sum_{i_{\frac{p+1}{2}}=i_{\frac{p-1}{2}}}^{M} \cdot \sum_{i_{\frac{p+1}{2}}=0}^{M} \cdots \sum_{i_p=i_{p-1}}^{M} \widetilde{h}_{i_1,\cdots,i_p} \cdot \prod_{j=1}^{\frac{p+1}{2}} \widetilde{x}(n-i_j) \cdot \prod_{j=\frac{p+3}{2}}^{p} \widetilde{x}^*(n-i_j). \tag{4.4}$$

In 4.4, $\widetilde{x}(n)$ and $\widetilde{y}(n)$ designate the input and output signals' envelopes around the carrier, with n, NL, M and $\widetilde{h}$ representing the sample index, the nonlinearity order, the memory depth and the LPE complex Volterra kernels respectively.

The LPE Volterra model of 4.4 has been used extensively in RF research. The model has been applied to develop solutions related to nonlinear communication system modeling and estimation [24], satellite communication [25], digital transmission channel equalization [26], multichannel nonlinear CDMA system equalization [27], analysis and cancellation of the inter-carrier interference in nonlinear OFDM systems [28], decision feedback equalization [29], nonlinear system and circuit analysis [30], data predistortion [31], PA modeling [32, 33, 34], and DPD [35, 36, 37]. Although computationally more efficient than its pass band counterpart, the LPE Volterra series in its classical form 4.4 still suffers from a large number of kernels. As stated earlier, this impediment has been the key limitation to its widespread adoption for RF PA behavioral modeling and predistortion. Various attempts [16, 21, 20] have been made to reduce the number of kernels required (e.g., Hammerstein, Wiener, Parallel Hammerstein, Parallel Wiener, DDR based Pruned Volterra series) but at the cost of reduced modeling accuracy.

In the following section, a novel baseband equivalent (BBE) expression of the Volterra series will be presented and the procedure to derive this new expression will be described in detail. Then the complexity and performance of this compact BBE Volterra series will be compared to those of the widely used LPE Volterra series expression. For purposes of clarity, a simplified version of the LPE Volterra series 4.4, with nonlinearity order $NL = 3$ and memory effects order $M = 1$ (i.e. $\widetilde{x}(t - T_s)$), will be used henceforward as per 4.5.

$$
\begin{aligned}
\widetilde{y}(n) &= \sum_{i_1=0}^{1} \widetilde{h}_{i_1} \widetilde{x}(n - i_1) + \sum_{i_1=0}^{1} \sum_{i_2=0}^{1} \sum_{i_3=0}^{1} \widetilde{h}_{i_1} \widetilde{x}(n - i_1) \widetilde{x}(n - i_2) \widetilde{x}^*(n - i_3) \\
&= \widetilde{h}_0 \widetilde{x}(n) + \widetilde{h}_1 \widetilde{x}(n - 1) + \widetilde{h}_{0,0,0} \widetilde{x}(n) \widetilde{x}(n) \widetilde{x}^*(n) + \widetilde{h}_{0,0,1} \widetilde{x}(n) \widetilde{x}(n) \widetilde{x}^*(n - 1) \\
&+ \widetilde{h}_{0,1,0} \widetilde{x}(n) \widetilde{x}(n - 1) \widetilde{x}^*(n) + \widetilde{h}_{0,1,1} \widetilde{x}(n) \widetilde{x}(n - 1) \widetilde{x}^*(n - 1) \\
&+ \widetilde{h}_{1,1,0} \widetilde{x}(n - 1) \widetilde{x}(n - 1) \widetilde{x}^*(n) + \widetilde{h}_{1,1,1} \widetilde{x}(n - 1) \widetilde{x}(n - 1) \widetilde{x}^*(n - 1).
\end{aligned} \tag{4.5}
$$

4.1 Novel Baseband Equivalent Volterra Series Formulation

4.1.1 Derivation of BBE Volterra Model

The investigation of the novel BBE Volterra series, suitable for the behavioral modeling and predistortion of RF PAs, requires a number of steps as shown Fig. 4.2.

Step 1: Continuous-time real-valued Volterra series modeling

The Volterra series framework [23] is initially used to describe the relationship between the real passband signals located at the system input and output stages as follows:

$$
y(t) = \sum_{p=1}^{NL} \int_{-\infty}^{\infty} \cdots \int_{-\infty}^{\infty} h_p\big(\tau_1, \cdots, \tau_p\big) \cdot \prod_{j=1}^{p} x(t - \tau_j) d\tau. \tag{4.6}
$$

where $x(t)$ and $y(t)$ represent the PA input and output RF signals and NL is the nonlinearity order.

Step 2: Real-valued to complex-valued envelope signal transformation

The input signal $x(t)$ is a band limited modulated signal that can be expressed as a function of its envelope around the carrier angular frequency ω_c as follows:

$$
x(t) = Re\Big\{ \widetilde{x}(t) e^{j\omega_c t} \Big\} = \frac{1}{2} \Big(\widetilde{x}^*(t) e^{-j\omega_c t} + \widetilde{x}(t) e^{j\omega_c t} \Big), \tag{4.7}
$$
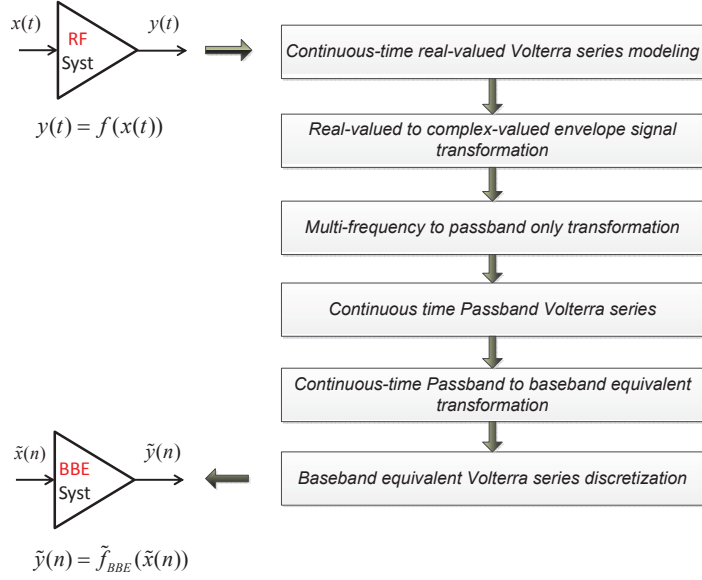
Figure 4.2: Baseband equivalent modeling approach

In 4.7, $\widetilde{x}(t)$ represents the complex baseband envelope signal that modulates the angular frequency ω_c. Substituting 4.7 into 4.6 yields an expression relating the output signal $y(t)$ to $\widetilde{x}(t)$ and ω_c as follows:

$$y(t) = f\left(\widetilde{x}(t), e^{\pm jp\omega_c t}\right); \, p \in \left\{1, .., NL\right\}, \tag{4.8}$$

where the describing function f is used to represent the real valued Volterra series of 4.6. Since the output signal $y(t)$ in 4.8 has been altered by the application of a nonlinear function to a band-limited RF signal, it now contains several spectrum components that involve multiple envelopes, represented by $\widetilde{y}_p(t)$. The spectrum components modulate the mixing products of ω_c as follows:

$$\begin{aligned}
y(t) &= \sum_{p=-NL}^{p=NL} \frac{1}{2}\left(\widetilde{y}_p^*(t)e^{-jp\omega_c t} + \widetilde{y}_p(t)e^{jp\omega_c t}\right) \\
&= \frac{1}{2}\left(\widetilde{y}_0^*(t)e^{-j0\omega_c t} + \widetilde{y}_0(t)e^{j0\omega_c t}\right) \\
&+ \frac{1}{2}\left(\widetilde{y}_1^*(t)e^{-j1\omega_c t} + \widetilde{y}_1(t)e^{j1\omega_c t}\right) \\
&+ \frac{1}{2}\left(\widetilde{y}_2^*(t)e^{-j2\omega_c t} + \widetilde{y}_2(t)e^{j2\omega_c t}\right)
\end{aligned}$$

$$\vdots$$
$$+ \quad \frac{1}{2}\Big(\widetilde{y}_{NL}^*(t)e^{-jNL\omega_c t} + \widetilde{y}_{NL}(t)e^{jNL\omega_c t}\Big), \tag{4.9}$$

where $\widetilde{y}_0(t)$ denotes the envelope at DC, $\widetilde{y}_1(t)$ denotes the envelopes of the first order in-band signals, $\widetilde{y}_2(t)$ denotes the envelopes of the second order harmonic signals and $\widetilde{y}_{NL}(t)$ represents the NL^{th} order harmonics signal.

Step 3: Multi-frequency to passband only transformation

By equating the terms that share the same frequency range (fundamental, mixing product) from the right sides of 4.8 and 4.9, a multi-frequency model is derived which consists of several distinct equations relating the output envelopes $\widetilde{y}_p(t)$ to $\widetilde{x}(t)$ and ω_c. Since we are mainly interested in the relationship between the envelopes of the output and input signals around the carrier frequency, only the passband component of the PA output is considered in the equation below:

$$
\begin{aligned}
y_{pb}(t) &= \frac{1}{2}\Big(\widetilde{y}_1^*(t)e^{-j\omega_c t} + \widetilde{y}_1(t)e^{j\omega_c t}\Big) \\
&= \frac{1}{2}\left(y_1^*(t) + y_1(t)\right), \tag{4.10}
\end{aligned}
$$

where $y_1(t) = \widetilde{y}_1(t)e^{j\omega_c t}$. The output signal envelope y_{pb} (t) in 4.10 has the form of a band limited signal similar to 4.7.

Step 4: Continuous time passband Volterra series.

The following derivation is presented for the term around $e^{j\omega_c t}$only; however, the same equation can be used to derive the conjugate term. The PA passband signal $y_1(t)$ can be modeled as a summation of the Volterra series nonlinear order responses $y_{1,2k+1}(t)$, or as the nonlinear order envelope responses $\widetilde{y}_{1,2k+1}(t)$, around the angular frequency ω_c as follows:

$$y_1(t) = \sum_{k=0}^{\infty} y_{1,2k+1}(t) = \left(\sum_{k=0}^{\infty} \widetilde{y}_{1,2k+1}(t)\right) e^{j\omega_c t} \tag{4.11}$$

Note that only odd powered terms are retained; even terms are discarded since they do not appear around the carrier frequency. Equating the terms on the right sides of the expanded equations in 4.8 and 4.10 yields a continuous BBE Volterra series that expresses $y_{1,2k+1}(t)$ as a function of $\widetilde{x}(t)$ and ω_c. Below is the expression derived using $y_{1,1}(t)$ and $y_{1,3}(t)$:

$$y_{1,1}(t) = \int_{-\infty}^{\infty} h_1\left(\tau_1\right) \cdot \widetilde{x}\left(t - \tau_1\right) \cdot e^{j\omega_c(t-\tau_1)} \cdot d\tau_1 \tag{4.12}$$

$$
\begin{aligned}
y_{1,3}(t) \;=\; & \int_{-\infty}^{\infty} \int_{-\infty}^{\infty} \int_{-\infty}^{\infty} h_3\left(\tau_1, \tau_2, \tau_3\right) \cdot \Bigg\{ \\
& \left(\widetilde{x}\left(t - \tau_1\right) \cdot e^{j\omega_c(t-\tau_1)}\right)\left(\widetilde{x}\left(t - \tau_2\right) \cdot e^{j\omega_c(t-\tau_2)}\right)\left(\widetilde{x}\left(t - \tau_3\right) \cdot e^{j\omega_c(t-\tau_3)}\right)^* \\
& + \left(\widetilde{x}\left(t - \tau_1\right) \cdot e^{j\omega_c(t-\tau_1)}\right)\left(\widetilde{x}\left(t - \tau_2\right) \cdot e^{j\omega_c(t-\tau_2)}\right)^*\left(\widetilde{x}\left(t - \tau_3\right) \cdot e^{j\omega_c(t-\tau_3)}\right) \\
& + \left(\widetilde{x}\left(t - \tau_1\right) \cdot e^{j\omega_c(t-\tau_1)}\right)^*\left(\widetilde{x}\left(t - \tau_2\right) \cdot e^{j\omega_c(t-\tau_2)}\right)\left(\widetilde{x}\left(t - \tau_3\right) \cdot e^{j\omega_c(t-\tau_3)}\right) \\
& \Bigg\} \cdot d\tau_3 d\tau_2 d\tau_1
\end{aligned}
\tag{4.13}
$$

Step 5: Continuous-time passband to baseband equivalent transformation.

In order to be computed by a digital processor, with manageable complexity, a passband model must be transformed to a BBE model. A BBE model includes the RF nonlinear dynamic distortion and computes the terms in baseband with a low sampling rate. To translate the passband model to baseband, the continuous time passband Volterra series of 4.12 is first rewritten using convolution form. The convolution form for $y_{1,1}(t)$ is given by:

$$y_{1,1}(t) = h_1\left(t\right) \star \left(\widetilde{x}\left(t\right) \cdot e^{j\omega_c t}\right) \tag{4.14}$$

As the kernel h_3 is tri-variate, $h_3(\tau_1, \tau_2, \tau_3)$, and the output $y_{1,3}(t)$ of 4.13 is mono-variate, the output function is re-assigned as follows: $y_{1,3}(t) = y_{1,3}(t_1, t_2, t_3)_{|t_1 = t_2 = t_3 = t} \triangleq y_{1,3}(t, t, t)$ [38]. The convolution form is given below.

$$
\begin{aligned}
y_{1,3}(t_1, t_2, t_3) \;=\; & h_3(t_1, t_2, t_3) \star \Bigg\{ \\
& \left(\widetilde{x}\left(t\right) \cdot e^{j\omega_c t_1}\right)\left(\widetilde{x}\left(t\right) \cdot e^{j\omega_c t_2}\right)\left(\widetilde{x}\left(t\right) \cdot e^{j\omega_c t_3}\right)^* \\
& + \left(\widetilde{x}\left(t\right) \cdot e^{j\omega_c t_1}\right)\left(\widetilde{x}\left(t\right) \cdot e^{j\omega_c t_2}\right)^*\left(\widetilde{x}\left(t\right) \cdot e^{j\omega_c t_3}\right) \\
& + \left(\widetilde{x}\left(t\right) \cdot e^{j\omega_c t_1}\right)^*\left(\widetilde{x}\left(t\right) \cdot e^{j\omega_c t_2}\right)\left(\widetilde{x}\left(t\right) \cdot e^{j\omega_c t_3}\right) \Bigg\}
\end{aligned}
\tag{4.15}
$$

Next, the Laplace transformation is applied to the convolution form of the Volterra series nonlinear order responses. The Laplace domain representation of (4.14-4.15) is given by:

$$
\begin{aligned}
Y_{1,1}(s) &= L\left(y_{1,1}(t)\right) \\
&= L\left(h_1(t)\right) \cdot L\left(\widetilde{x}(t)e^{j\omega_c t}\right) \\
&= H_1(s) \cdot \widetilde{X}(s - j\omega_c). \qquad\qquad (4.16)
\end{aligned}
$$

$$
\begin{aligned}
Y_{1,3}(s_1, s_2, s_3) &= L\left(y_{1,3}(t_1, t_2, t_3)\right) \\
&= L\left(h_3(t_1, t_2, t_3)\right) \cdot \Bigg\{ \\
&\quad L\left(\left(\widetilde{x}(t)\cdot e^{j\omega_c t_1}\right)\left(\widetilde{x}(t)\cdot e^{j\omega_c t_2}\right)\left(\widetilde{x}(t)\cdot e^{j\omega_c t_3}\right)^*\right) \\
&\quad + L\left(\left(\widetilde{x}(t)\cdot e^{j\omega_c t_1}\right)\left(\widetilde{x}(t)\cdot e^{j\omega_c t_2}\right)^*\left(\widetilde{x}(t)\cdot e^{j\omega_c t_3}\right)\right) \\
&\quad + L\left(\left(\widetilde{x}(t)\cdot e^{j\omega_c t_1}\right)^*\left(\widetilde{x}(t)\cdot e^{j\omega_c t_2}\right)\left(\widetilde{x}(t)\cdot e^{j\omega_c t_3}\right)\right) \Bigg\} \\
&= L\left(h_3(t_1, t_2, t_3)\right) \cdot \Bigg\{ \\
&\quad L\left(\left(\widetilde{x}(t)\cdot e^{j\omega_c t_1}\right)\right) \cdot L\left(\left(\widetilde{x}(t)\cdot e^{j\omega_c t_2}\right)\right) \cdot L\left(\left(\widetilde{x}(t)\cdot e^{j\omega_c t_3}\right)^*\right) \\
&\quad + L\left(\left(\widetilde{x}(t)\cdot e^{j\omega_c t_1}\right)\right) \cdot L\left(\left(\widetilde{x}(t)\cdot e^{j\omega_c t_2}\right)^*\right) \cdot L\left(\left(\widetilde{x}(t)\cdot e^{j\omega_c t_3}\right)\right) \\
&\quad + L\left(\left(\widetilde{x}(t)\cdot e^{j\omega_c t_1}\right)^*\right) \cdot L\left(\left(\widetilde{x}(t)\cdot e^{j\omega_c t_2}\right)\right) \cdot L\left(\left(\widetilde{x}(t)\cdot e^{j\omega_c t_3}\right)\right) \Bigg\}
\end{aligned}
$$

$$
\begin{aligned}
Y_{1,3}(s_1, s_2, s_3) &= H_3(s_1, s_2, s_3) \cdot \Bigg\{ \\
&\quad \widetilde{X}(s_1 - j\omega_c) \cdot \widetilde{X}(s_2 - j\omega_c) \cdot \widetilde{X}^*\left((s_3 - j\omega_c)^*\right) \\
&\quad + \widetilde{X}(s_1 - j\omega_c) \cdot \widetilde{X}^*\left((s_2 - j\omega_c)^*\right) \cdot \widetilde{X}(s_3 - j\omega_c) \\
&\quad + \widetilde{X}^*\left((s_1 - j\omega_c)^*\right) \cdot \widetilde{X}(s_2 - j\omega_c) \cdot \widetilde{X}(s_3 - j\omega_c) \Bigg\}. \qquad (4.17)
\end{aligned}
$$

The above derivation uses the distributivity and product transforms properties of multivariate Laplace transform [38]. he BBE form of 4.16 and 4.17 can be derived by applying a frequency translation of $j\omega_c$ to the constituent terms $Y_{1,1}$ and $Y_{1,3}$ as follows:

$$\begin{aligned}
\widetilde{Y}_{1,1}(s) &= Y_{1,1}(s + j\omega_c) \\
&= H_1(s + j\omega_c) \cdot \widetilde{X}(s) \\
&= \widetilde{H}_1(s) \cdot \widetilde{X}(s).
\end{aligned} \qquad (4.18)$$

$$\begin{aligned}
\widetilde{Y}_{1,3}(s_1, s_2, s_3) &= Y_{1,3}(s_1 + j\omega_c, s_2 + j\omega_c, s_3 + j\omega_c) \\
&= H_3(s_1 + j\omega_c, s_2 + j\omega_c, s_3 + j\omega_c) \cdot \Bigg\{ \\
&\quad \widetilde{X}(s_1) \cdot \widetilde{X}(s_2) \cdot \widetilde{X}^*((s_3)^*) \\
&\quad + \widetilde{X}(s_1) \cdot \widetilde{X}^*((s_2)^*) \cdot \widetilde{X}(s_3) \\
&\quad + \widetilde{X}^*((s_1)^*) \cdot \widetilde{X}(s_2) \cdot \widetilde{X}(s_3) \Bigg\} \\
&= \widetilde{H}_3(s_1, s_2, s_3) \cdot \Bigg\{ \\
&\quad \widetilde{X}(s_1) \cdot \widetilde{X}(s_2) \cdot \widetilde{X}^*((s_3)^*) \\
&\quad + \widetilde{X}(s_1) \cdot \widetilde{X}^*((s_2)^*) \cdot \widetilde{X}(s_3) \\
&\quad + \widetilde{X}^*((s_1)^*) \cdot \widetilde{X}(s_2) \cdot \widetilde{X}(s_3) \Bigg\}.
\end{aligned} \qquad (4.19)$$

where $\widetilde{Y}_{1,1}$ and $\widetilde{Y}_{1,3}$ designate the BBE outputs and $\widetilde{H}_1$ and $\widetilde{H}_3$ denote the BBE kernels, respectively. Applying the inverse Laplace to 4.18 and 4.19 yields the continuous-time BBE model as follows:

$$\widetilde{y}_{1,1}(t) = \int_{-\infty}^{\infty} \widetilde{h}_1(\tau_1) \cdot \widetilde{x}(t - \tau_1) \cdot d\tau_1 \qquad (4.20)$$

$$\begin{aligned}
\widetilde{y}_{1,3}(t) &= \int_{-\infty}^{\infty} \int_{-\infty}^{\infty} \int_{-\infty}^{\infty} \widetilde{h}_3(\tau_1, \tau_2, \tau_3) \cdot \Bigg\{ \\
&\quad (\widetilde{x}(t - \tau_1))(\widetilde{x}(t - \tau_2))(\widetilde{x}(t - \tau_3))^* \\
&\quad + (\widetilde{x}(t - \tau_1))(\widetilde{x}(t - \tau_2))^*(\widetilde{x}(t - \tau_3)) \\
&\quad + (\widetilde{x}(t - \tau_1))^*(\widetilde{x}(t - \tau_2))(\widetilde{x}(t - \tau_3)) \\
&\quad \Bigg\} \cdot d\tau_3 d\tau_2 d\tau_1
\end{aligned} \qquad (4.21)$$

Step 6: Discrete-time baseband equivalent Volterra series model.

Using the signal and system causality, the integral bounds of model 4.20 and 4.21 are adjusted to $\infty \to t$ and $-\infty \to 0$, respectively. The model is then given by:

$$\widetilde{y}_{1,1}(t) = \int_0^t \widetilde{h}_1\left(\tau_1\right) \cdot \widetilde{x}\left(t - \tau_1\right) \cdot d\tau_1$$

$$
\begin{aligned}
\widetilde{y}_{1,3}(t) \;=\; & \int_0^t \int_0^t \int_0^t \widetilde{h}_3\left(\tau_1, \tau_2, \tau_3\right) \cdot \Big\{ \\
& \left(\widetilde{x}\left(t - \tau_1\right)\right)\left(\widetilde{x}\left(t - \tau_2\right)\right)\left(\widetilde{x}\left(t - \tau_3\right)\right)^* \\
& + \left(\widetilde{x}\left(t - \tau_1\right)\right)\left(\widetilde{x}\left(t - \tau_2\right)\right)^*\left(\widetilde{x}\left(t - \tau_3\right)\right) \\
& + \left(\widetilde{x}\left(t - \tau_1\right)\right)^*\left(\widetilde{x}\left(t - \tau_2\right)\right)\left(\widetilde{x}\left(t - \tau_3\right)\right) \\
& \Big\} \cdot d\tau_3 d\tau_2 d\tau_1
\end{aligned}
$$

Using the fading memory assumption for the steady-state $(t > T_\infty)$ (the transient-response, time-invariant Volterra series is defined as $t < T_\infty$), the model response can be represented as:

$$\widetilde{y}_{1,1}(t) = \int_0^{T_\infty} \widetilde{h}_1\left(\tau_1\right) \cdot \widetilde{x}\left(t - \tau_1\right) \cdot d\tau_1$$

$$
\begin{aligned}
\widetilde{y}_{1,3}(t) \;=\; & \int_0^{T_\infty} \int_0^{T_\infty} \int_0^{T_\infty} \widetilde{h}_3\left(\tau_1, \tau_2, \tau_3\right) \cdot \Big\{ \\
& \left(\widetilde{x}\left(t - \tau_1\right)\right)\left(\widetilde{x}\left(t - \tau_2\right)\right)\left(\widetilde{x}\left(t - \tau_3\right)\right)^* \\
& + \left(\widetilde{x}\left(t - \tau_1\right)\right)\left(\widetilde{x}\left(t - \tau_2\right)\right)^*\left(\widetilde{x}\left(t - \tau_3\right)\right) \\
& + \left(\widetilde{x}\left(t - \tau_1\right)\right)^*\left(\widetilde{x}\left(t - \tau_2\right)\right)\left(\widetilde{x}\left(t - \tau_3\right)\right) \\
& \Big\} \cdot d\tau_3 d\tau_2 d\tau_1
\end{aligned}
$$

Using the symmetry of the integrated function (distortion components are symmetrical and Volterra kernels can be symmetrized [23]), the model can be simplified to:

$$\widetilde{y}_{1,1}(t) = \int_0^{T_\infty} \widetilde{h}_1\left(\tau_1\right) \cdot \widetilde{x}\left(t - \tau_1\right) \cdot d\tau_1$$

$$\widetilde{y}_{1,3}(t) \;=\; \int_0^{T_\infty} \int_{\tau_1}^{T_\infty} \int_{\tau_2}^{T_\infty} \widetilde{h}_3\left(\tau_1, \tau_2, \tau_3\right) \cdot \Big\{$$
$$\left(\widetilde{x}\left(t - \tau_1\right)\right)\left(\widetilde{x}\left(t - \tau_2\right)\right)\left(\widetilde{x}\left(t - \tau_3\right)\right)^*$$
$$+ \left(\widetilde{x}\left(t - \tau_1\right)\right)\left(\widetilde{x}\left(t - \tau_2\right)\right)^*\left(\widetilde{x}\left(t - \tau_3\right)\right)$$
$$+ \left(\widetilde{x}\left(t - \tau_1\right)\right)^*\left(\widetilde{x}\left(t - \tau_2\right)\right)\left(\widetilde{x}\left(t - \tau_3\right)\right)$$
$$\Big\} \cdot d\tau_3 d\tau_2 d\tau_1$$

Digitization of the model yields:

$$\widetilde{y}_{1,1}(n) = \sum_{i_1=0}^{M_1} \widetilde{h}_{i_1} \cdot \widetilde{x}_1\left(n, i_1\right)$$

$$\widetilde{y}_{1,3}(n) = \sum_{i_1=0}^{M_3} \sum_{i_2=i_1}^{M_3} \sum_{i_3=i_2}^{M_3} \widetilde{h}_{i_1,i_2,i_3} \cdot \widetilde{x}_3\left(n, i_1, i_2, i_3\right)$$

$$\widetilde{x}_1\left(n, i_1\right) = \widetilde{x}\left(n - i_1\right)$$

$$\widetilde{x}_3\left(n, i_1, i_2, i_3\right) \;=\; \widetilde{x}\left(n - i_1\right)\widetilde{x}\left(n - i_2\right)\widetilde{x}^*\left(n - i_3\right)$$
$$+\; \widetilde{x}\left(n - i_1\right)\widetilde{x}^*\left(n - i_2\right)\widetilde{x}\left(n - i_3\right)$$
$$+\; \widetilde{x}^*\left(n - i_1\right)\widetilde{x}\left(n - i_2\right)\widetilde{x}\left(n - i_3\right)$$

where M_1, M_3 denote the memory depth of the first and third order Volterra series. Similarly to the above derivation, it could be shown that the fifth order Volterra kernel, $\widetilde{y}_{1,5}(n)$, is given by:

$$\widetilde{y}_{1,5}(n) = \sum_{i_1=0}^{M_5} \sum_{i_2=i_1}^{M_5} \sum_{i_3=i_2}^{M_5} \sum_{i_4=i_3}^{M_5} \sum_{i_5=i_4}^{M_5} \widetilde{h}_{i_1,i_2,i_3,i_4,i_5} \cdot \widetilde{x}_5\left(n, i_1, i_2, i_3, i_4, i_5\right)$$

$$\widetilde{x}_5\left(n, i_1, i_2, i_3, i_4, i_5\right) \;=\; \widetilde{x}\left(n - i_1\right)\widetilde{x}\left(n - i_2\right)\widetilde{x}\left(n - i_3\right)\widetilde{x}^*\left(n - i_4\right)\widetilde{x}^*\left(n - i_5\right)$$
$$+\; \widetilde{x}\left(n - i_1\right)\widetilde{x}\left(n - i_2\right)\widetilde{x}^*\left(n - i_3\right)\widetilde{x}\left(n - i_4\right)\widetilde{x}^*\left(n - i_5\right)$$
$$+\; \widetilde{x}\left(n - i_1\right)\widetilde{x}^*\left(n - i_2\right)\widetilde{x}\left(n - i_3\right)\widetilde{x}\left(n - i_4\right)\widetilde{x}^*\left(n - i_5\right)$$
$$+\; \widetilde{x}^*\left(n - i_1\right)\widetilde{x}\left(n - i_2\right)\widetilde{x}\left(n - i_3\right)\widetilde{x}\left(n - i_4\right)\widetilde{x}^*\left(n - i_5\right)$$

$$\begin{aligned}
&+\quad \widetilde{x}\left(n-i_1\right)\widetilde{x}\left(n-i_2\right)\widetilde{x}^*\left(n-i_3\right)\widetilde{x}^*\left(n-i_4\right)\widetilde{x}\left(n-i_5\right)\\
&+\quad \widetilde{x}\left(n-i_1\right)\widetilde{x}^*\left(n-i_2\right)\widetilde{x}\left(n-i_3\right)\widetilde{x}^*\left(n-i_4\right)\widetilde{x}\left(n-i_5\right)\\
&+\quad \widetilde{x}^*\left(n-i_1\right)\widetilde{x}\left(n-i_2\right)\widetilde{x}\left(n-i_3\right)\widetilde{x}^*\left(n-i_4\right)\widetilde{x}\left(n-i_5\right)\\
&+\quad \widetilde{x}\left(n-i_1\right)\widetilde{x}^*\left(n-i_2\right)\widetilde{x}^*\left(n-i_3\right)\widetilde{x}\left(n-i_4\right)\widetilde{x}\left(n-i_5\right)\\
&+\quad \widetilde{x}^*\left(n-i_1\right)\widetilde{x}\left(n-i_2\right)\widetilde{x}^*\left(n-i_3\right)\widetilde{x}\left(n-i_4\right)\widetilde{x}\left(n-i_5\right)\\
&+\quad \widetilde{x}^*\left(n-i_1\right)\widetilde{x}^*\left(n-i_2\right)\widetilde{x}\left(n-i_3\right)\widetilde{x}\left(n-i_4\right)\widetilde{x}\left(n-i_5\right)
\end{aligned}$$

where M_5 denotes the memory depth of the fifth order Volterra series. The complex valued BBE Volterra series up to nonlinear distortion products 5 is then given by:

$$\widetilde{y}_1(n) = \widetilde{y}_{1,1}(n) + \widetilde{y}_{1,3}(n) + \widetilde{y}_{1,5}(n) \tag{4.22}$$

Higher order distortion products can be similarly derived. In addition, only odd powered terms are retained. The terms $\widetilde{x}_3(n, i_1, i_2, i_3)$ and $\widetilde{x}_5(n, i_1, i_2, i_3, i_4, i_5)$ are linear combinations of 3 third order and 10 fifth order distortion products. An example of the BBE Volterra model of 4.22 is given for $NL = 3$ and $M = 1$ as follows

$$\begin{aligned}
\widetilde{y}(n) \;=\; & \frac{1}{2}h_0\widetilde{x}(n) + \frac{1}{2}h_1\widetilde{x}(n-1) + \frac{3}{8}h_{0,0,0}\widetilde{x}(n)\widetilde{x}(n)\widetilde{x}^*(n)\\
& + \frac{1}{8}h_{0,0,1}\left(2\widetilde{x}(n)\widetilde{x}(n-1)\widetilde{x}^*(n) + \widetilde{x}(n)\widetilde{x}(n)\widetilde{x}^*(n-1)\right)\\
& + \frac{1}{8}h_{0,1,1}\left(2\widetilde{x}(n)\widetilde{x}(n-1)\widetilde{x}^*(n-1) + \widetilde{x}(n-1)\widetilde{x}(n-1)\widetilde{x}^*(n)\right)\\
& + \frac{3}{8}h_{1,1,1}\widetilde{x}(n-1)\widetilde{x}(n-1)\widetilde{x}^*(n-1) \tag{4.23}
\end{aligned}$$

Comparison of the classical expression 4.5 with the newly proposed BBE Volterra expression 4.23 results in several conclusions. For example, the different distortion products which were assigned distinct kernels in 4.5 have been linearly combined to form a novel term in the new model space proposed by 4.23, and hence, share the same kernel.

Table 4.1 summarizes the number of kernels needed for four different modeling scenarios where the nonlinearity order has been set to seven and the memory depth M, equals $M_1 = M_3 = M_5 = M$. The expressions for the number of coefficients were used to plot Fig. 4.3. As can be seen, the newly proposed, compact model involved a significantly lower number of coefficients than the full classical LPE Volterra series, especially as the memory depth increased. However, the pruned LPE Volterra using the DDR approach also required a smaller number of coefficients as it discarded distortion products with a dynamic order $\geq$ three [21]. It is worth mentioning that the proposed model included all of the distortion products, while maintaining a similar number of coefficients due to its compact expression,

Table 4.1: Complexity analysis for nonlinearity order of 7

Model	Number of coefficients for NL=7
Classical LPE Volterra	$4 + \frac{43}{4}M + \frac{451}{36}M^2 + \frac{1213}{144}M^3 + \frac{121}{36}M^4$ $+ \frac{59}{72}M^5 + \frac{1}{9}M^6 + \frac{1}{144}M^7$
Proposed BBE Volterra	$4 + \frac{1619}{210}M + \frac{1973}{360}M^2 + \frac{1597}{720}M^3 + \frac{37}{72}M^4$ $+ \frac{13}{180}M^5 + \frac{1}{180}M^6 + \frac{1}{5040}M^7$
DDR LPE Volterra R=2	$4 + \frac{25}{2}M + \frac{11}{2}M^2$
DDR LPE Volterra R=3	$4 + \frac{131}{6}M + \frac{39}{2}M^2 + \frac{14}{3}M^3$
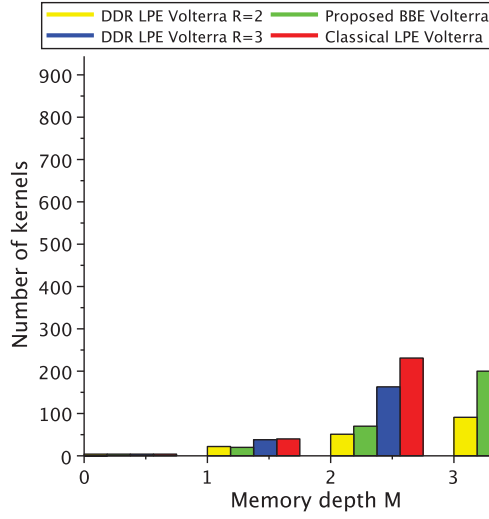
Figure 4.3: Illustration of the complexity of different Volterra formulations of NL=7

and did not require any pruning which could compromise its modeling and linearization capability as memory effects intensify.

4.1.2 Model Identification

The signal transformations used to derive the new BBE expression 4.22 preserved the linear property of the Volterra series with respect to its coefficients. Therefore, commonly used model identification algorithms such as the least square error (LSE) can be applied to identify the kernels in 4.22 for a given RF PA. Equation 4.24 suggests the expression used to deduce the LSE solution of 4.22

$$X \cdot h = Y \tag{4.24}$$

where X, h and Y denote the input signal non-square matrix, the vector that contains the unknown kernels and the output signal vector as described below:

$$X = \begin{pmatrix} \widetilde{x}_0(1) & \cdots & \widetilde{x}_M(1) & \widetilde{x}_{0,0,0}(1) & \cdots & \widetilde{x}_{M,M,M}(1) \\ \vdots & \ddots & \vdots & \vdots & \ddots & \vdots & \cdots \\ \widetilde{x}_0(N) & \cdots\cdots & \widetilde{x}_M(N) & \widetilde{x}_{0,0,0}(N) & \cdots\cdots & \widetilde{x}_{M,M,M}(N) \end{pmatrix}$$

$$h = \begin{pmatrix} h_0 \\ \vdots \\ h_M \\ \vdots \end{pmatrix}$$

$$Y = \begin{pmatrix} \widetilde{y}(1) \\ \vdots \\ \widetilde{y}(N) \end{pmatrix},$$

In the above expression, N represents the total number of measurement data. The solution to the problem defined in 4.24 is:

$$\hat{h} = \left(X^t \cdot X\right)^{-1} \cdot X^t \cdot Y$$

where $\hat{h}$ is the estimate of h.

4.1.3   Validation

To assess the performance of the newly proposed compact BBE Volterra model, the model was used to linearize two RF PAs driven with different signals. Its linearization performance was compared with that of the LPE Volterra model's (pruned using the DDR approach). Fig. 4.4 shows the mixed signal linearization test bench used. It consisted of i) an arbitrary wave generator (N8241A) which was connected to a vector signal generator (E8267D) for test signal generation, ii) a vector signal analyzer (N9030A) for output signal capture, and iii) a host computer for test signal synthesis and upload, delay estimation and alignment, and output signal download, in addition to model identification.

Tables 4.2 and 4.3 summarize the linearization results found with each demonstrator amplifier using both the proposed compact and the pruned LPE Volterra models. For all testing, the nonlinearity order was set to seven and the memory depth was set two and
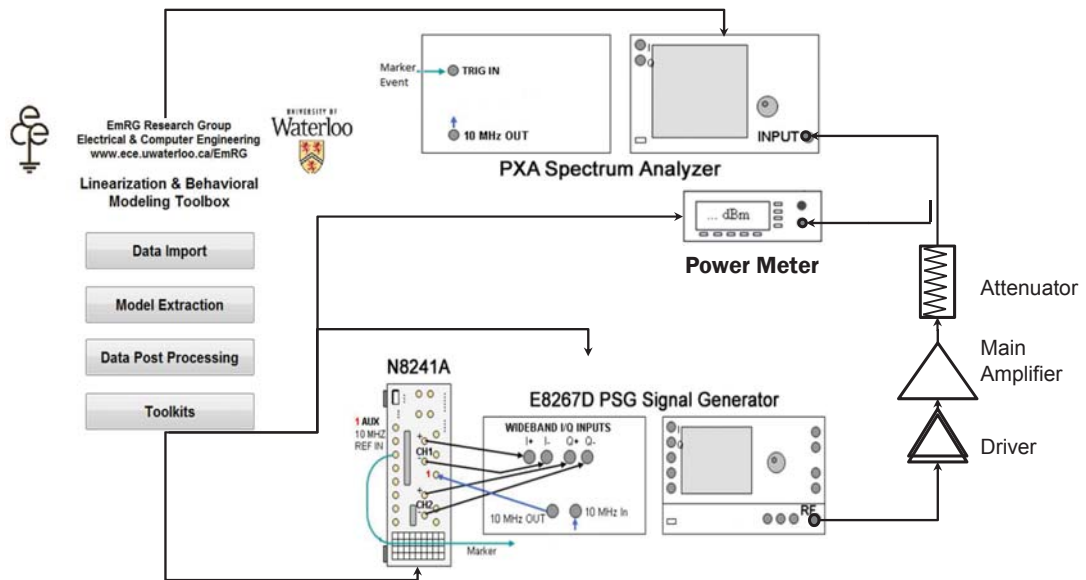
Figure 4.4: Broadband mixed signal linearization platform

Table 4.2: Linearization performance of a class AB GaN PA

Model	Parameters	Number of Coefficients	EVM (%)	ACLR (dBc)
Without DPD			5.5	-35
Classical LPE Volterra	NL=7 ; M=2	231	2	-48
DDR LPE Volterra	NL=7 ; M=3 ; r=2	91	2.1	-48
Proposed BBE Volterra	NL=7 ; M=2	70	2	-48
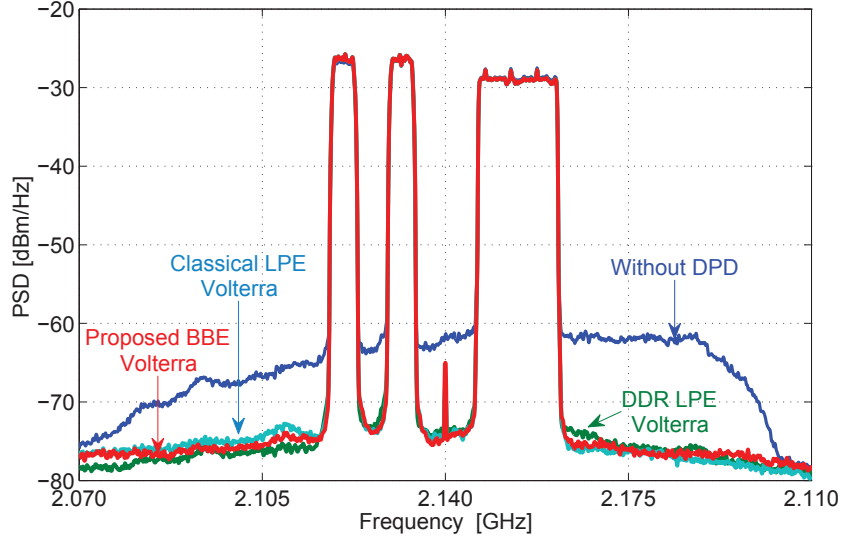
Figure 4.5: Linearization performance of a single ended GaN PA driven with 40 MHz multi-standard signal using different Volterra series expressions

three. According to Table 4.2, both the pruned LPE Volterra and the compact models allowed for similar linearization performance as the EVM was reduced from 5.5% to 2% and the ACLR was increased from 35 dB to about 50 dB (after application of the linearization). This excellent linearization capacity was successfully achieved despite the significant reduction in the number of kernels required by the compact model (91 in the pruned LPE Volterra model vs. 70 in the proposed model). It is worth mentioning that the full LPE Volterra model required 231 kernels.

The linearization performance was further confirmed (see Fig. 4.5) by examining the spectrum of the 45 W GaN PA output signals with and without predistortion. In the case of the second RF PA demonstrator (see Table 4.3), the pruned LPE Volterra and the proposed

Table 4.3: Linearization performance of LDMOS Doherty PA

Model	Parameters	Number of Coefficients	EVM (%)	ACLR (dBc)
Without DPD			5.5	-35
Classical LPE Volterra	NL=7 ; M=2	231	1.9	-50
DDR LPE Volterra	NL=7 ; M=3 ; r=2	91	2.3	-46
Proposed BBE Volterra	NL=7 ; M=2	70	1.9	-50
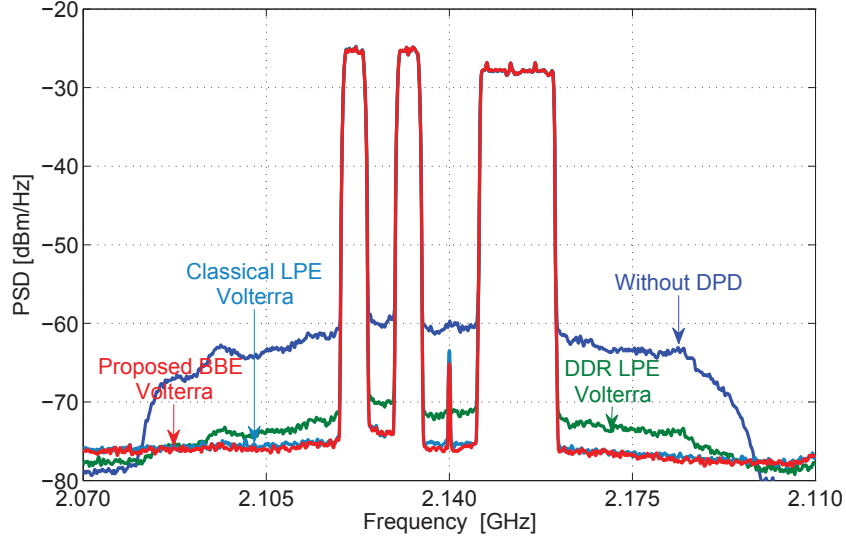
Figure 4.6: Linearization performance of an LDMOS DPA driven with 40 MHz multi-standard signal using different Volterra series expressions

model showed different linearization performance. While both the classical LPE Volterra model and the compact BBE Volterra model achieved similar linearization results in terms of ACLR (-50 dBc) and EVM (1.9%), the DDR LPE Volterra led to a 4 dB lower ACLR and 0.4% higher EVM. The superiority of the linearization capacity of the new compact model is confirmed in Fig. 4.6 which displays the spectra of the Doherty RF PA with and without linearization. One can clearly observe a noticeable residual out of band spectrum regrowth in the signal obtained using the pruned DDR LPE. As previously mentioned, the DDR pruning approach while elegant, may suffer from reduced linearization capability when the dynamic order is set to two as it eliminates a large number of distortion products. The new compact BBE Volterra model did not suffer from this limitation as it maintained all the distortion products. The pruned LPE Volterra linearization performance could be improved if the dynamic order R were increased further, however, this would result in a larger number of kernels (e.g., the number of kernels would be 162 for r=3).

4.2 BBE Volterra Formulation for Concurrent Dual-band PA

For simplicity purposes, the provided analysis in this thesis illustrates the dual-band case; however, it can be easily generalized to the multi-band scenario. A dual-band signal can be expressed as follows:

A carrier aggregated signal over two bands, as the one shown in Fig. 3.1, can be expressed as

$$
\begin{aligned}
x(t) &= x_1(t) + x_2(t) \\
&= Re\left(\widetilde{x}_1(t)e^{(j\omega_1 t)} + \widetilde{x}_2(t)e^{(j\omega_2 t)}\right)
\end{aligned}
$$

where $x(t)$ is the carrier aggregated signal, $x_1(t)$ and $x_2(t)$ are the mixed mode signals in each band, $\widetilde{x}_1(t)$ and $\widetilde{x}_2(t)$ denote the baseband envelopes of $x_1(t)$ and $x_2(t)$ around the angular frequencies ω_1 and ω_2, respectively. The carrier aggregated signal can be represented as a broadband signal with an angular carrier frequency $((\omega_1+\omega_2)/2)$ as given by:

$$
\begin{aligned}
x(t) &= Re\left(\widetilde{x}(t)\cdot e^{\left(j\frac{(\omega_1+\omega_2)}{2}t\right)}\right) \\
&= Re\left(\left(\widetilde{x}_1(t)e^{\left(j\frac{(\omega_1-\omega_2)}{2}t\right)} + \widetilde{x}_2(t)e^{\left(j\frac{(\omega_2-\omega_1)}{2}t\right)}\right)e^{\left(j\frac{(\omega_1+\omega_2)}{2}t\right)}\right)
\end{aligned}
$$

where $\widetilde{x}(t)$ is the baseband envelope of the carrier aggregated signal given by

$$
\widetilde{x}(t) = \widetilde{x}_1(t)e^{\left(j\frac{(\omega_1-\omega_2)}{2}t\right)} + \widetilde{x}_2(t)e^{\left(j\frac{(\omega_2-\omega_1)}{2}t\right)}.
$$

When the dual-band signal is amplified by a PA, the passband component of the output signal, $y_{pb}(t)$, can be described as:

$$
\begin{aligned}
y(t) &= y_1(t) + y_2(t) \\
&= Re\left(\widetilde{y}(t)\cdot e^{\left(j\frac{(\omega_1+\omega_2)}{2}t\right)}\right) \\
&= Re\left(\left(\widetilde{y}_1(t)e^{\left(j\frac{(\omega_1-\omega_2)}{2}t\right)} + \widetilde{y}_2(t)e^{\left(j\frac{(\omega_2-\omega_1)}{2}t\right)}\right)e^{\left(j\frac{(\omega_1+\omega_2)}{2}t\right)}\right)
\end{aligned}
$$

where $y_1(t)$ and $y_2(t)$ are multi-carrier output signals modulated around the angular frequencies ω_1 and ω_2 respectively, and $\widetilde{y}_1(t)$ and $\widetilde{y}_2(t)$ denote the baseband envelopes of $y_1(t)$ and $y_2(t)$, respectively.

In the classical PA behavioral modeling approach, the PA behavior is modeled as a single-input single-output (SISO) system where the PA output $\widetilde{y}_{pb}(t)$ is a function of the PA input $\widetilde{x}(t)$, as given in 4.25:

$$\widetilde{y}_{pb}(t) = \widetilde{f}\left(\widetilde{x}(t)\right) \tag{4.25}$$

where $\widetilde{f}$ is the SISO describing function of the PA (see Fig. 4.7). Digitization of the SISO model requires sampling both $\widetilde{x}(t)$ and $\widetilde{y}_{pb}(t)$ at a high frequency rate as follows:

$$f_{s,SiSo} \geq \left(S + 5{\cdot}max\left(\frac{B_1}{2}, \frac{B_2}{2}\right)\right)$$

where B_1 and B_2 represent the bandwidths of $\widetilde{x}_1(t)$ and $\widetilde{x}_2(t)$, respectively, and S denotes the frequency spacing between the two signals (i.e., $S = f_2 - f_1 = \frac{(\omega_2 - \omega_1)}{2\Pi}$), where f_1 and f_2 are the two bands' carrier frequencies, respectively. The factor of 5 represents the spectrum regrowth due to PA nonlinearity which is assumed equal to 5.

Alternatively, a dual-input dual-output (DIDO) approach would require a significantly lower sampling rate. In such a formulation, the PA output in each band (i.e., $\widetilde{y}_1(t)$ and $\widetilde{y}_2(t)$), is expressed separately as a function of the two input signals' envelopes $\widetilde{x}_1(t)$ and $\widetilde{x}_2(t)$, as given by:

$$\begin{cases} \widetilde{y}_1(t) &= \widetilde{f}_1(\widetilde{x}_1(t), \widetilde{x}_2(t)) \\ \widetilde{y}_2(t) &= \widetilde{f}_2(\widetilde{x}_1(t), \widetilde{x}_2(t)) \end{cases}$$

where $\widetilde{f}_1$ and $\widetilde{f}_2$ form the PA's dual-band describing functions (shown in Fig. 4.7). The construction of the two describing functions, $\widetilde{f}_1$ and $\widetilde{f}_2$, needed to model and/or to linearize the dual-band PA, is performed in the digital domain. This requires the sampling of $\widetilde{x}_1(t)$, $\widetilde{x}_2(t)$, $\widetilde{y}_1(t)$ and $\widetilde{y}_2(t)$ at a frequency rate given by

$$f_{s,DiDo} \geq \left(5{\cdot}max\left(\frac{B_1}{2}, \frac{B_2}{2}\right)\right)$$

This sampling rate is independent of the frequency separation, S, which may be very large. Hence, $f_{s,DiDo}$ is significantly lower than $f_{s,SiSo}$. For example, if we assume a dual-band signal composed of a $15MHz$ WCDMA signal rate required for the SISO model. The ratio between the two sampling rates is equal to $\frac{f_{s,DiDo}}{f_{s,SiSo}} = 0.11$.
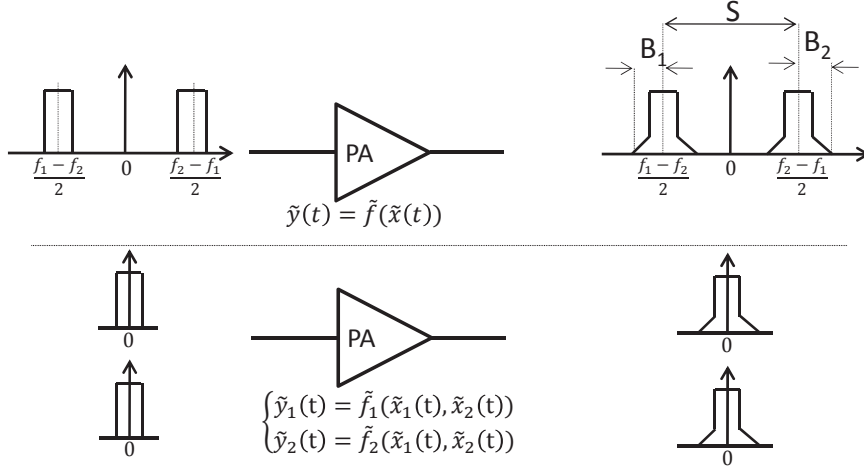
Figure 4.7: SISO (upper) vs. DIDO (bottom) PA behavioral modeling approach

4.2.1 Derivation of BBE DIDO Volterra Model

The behavior modeling and linearization approaches outlined in the literature to date, have been restricted to generalizing low complexity schemes for single-band PAs. Volterra series has been avoided due to the unmanageable number of coefficients and consequent complexity. However, theoretically, the Volterra series is a more appropriate modeling framework for dual-band PAs which are recursive nonlinear dynamic systems with fading memory [19]. In [22], Benedetto presented a series of transformations to derive the well-known LPE Volterra series. The empirically pruned LPE Volterra series has been successfully applied to model and linearize single-band PAs. In this section, a new BBE dual-band Volterra series formulation is derived from the original passband real-valued Volterra series [23] to model and linearize dual-band PAs. This approach does not require pruning and the proposed derivation is particularly attentive to the problem of exponential growth in the number of coefficients experienced with the LPE approach. In the subsequent paragraphs, the steps followed to derive the proposed model are described:

Step 1: Continuous-time real-valued Volterra series modeling:

The Volterra series framework [23] is initially used to describe the relationship between the real pass-band signals at the system input and output:

$$y(t) = \sum_{p=1}^{NL} \int_{-\infty}^{\infty} \cdots \int_{-\infty}^{\infty} h_p(\tau_1, \cdots, \tau_p) \cdot \prod_{j=1}^{p} x(t - \tau_j) d\tau. \tag{4.26}$$

57

where $x(t)$ and $y(t)$ represent the PA input and output RF signals and NL is the nonlinearity order.

Step 2: Real-valued to complex-valued envelope signal transformation:

In the case of a dual-band PA, the band-limited input signal $x(t)$ can be expressed as:

$$
\begin{aligned}
x(t) &= Re\left\{\widetilde{x}_1(t)e^{j\omega_1 t} + \widetilde{x}_2(t)e^{j\omega_2 t}\right\} \\
&= \frac{1}{2}\left(\widetilde{x}_1^*(t)e^{-j\omega_1 t} + \widetilde{x}_1(t)e^{j\omega_1 t}\right) \\
&+ \frac{1}{2}\left(\widetilde{x}_2^*(t)e^{-j\omega_2 t} + \widetilde{x}_2(t)e^{j\omega_2 t}\right)
\end{aligned}
\tag{4.27}
$$

where $\widetilde{x}_1(t)$ and $\widetilde{x}_2(t)$ represent the two complex baseband envelope signals that modulate the two different angular frequencies, ω_1 and ω_2. Substituting 4.27 into 4.26 yields an expression relating the output signal $y(t)$ to $\widetilde{x}_1(t)$, $\widetilde{x}_2(t)$, ω_1 to ω_2 as follows:

$$
y(t) = f\left(\widetilde{x}_1(t), \widetilde{x}_2(t), e^{\pm jp\omega_1 t}, e^{\pm jq\omega_2 t}\right) \; ; \; (p,q) \in \left\{1, .., NL\right\}^2,
\tag{4.28}
$$

where the describing function f is used to represent the real valued Volterra series 4.26. Since the output signal $y(t)$ in 4.28 is a result of the application of a nonlinear function to a band-limited RF signal, it contains several spectrum components that involve multiple envelopes, $\widetilde{y}_{p,q}(t)$, which modulate the mixing products, $p\omega_1 \pm q\omega_2$, of ω_1 and ω_2 as shown in 4.29:

$$
\begin{aligned}
y(t) &= \sum_{p,q=-NL,-NL}^{p,q=NL,NL} \frac{1}{2}\left(\widetilde{y}_{p,q}^*(t)e^{-j(p\omega_1+q\omega_2)t} + \widetilde{y}_{p,q}(t)e^{j(p\omega_1+q\omega_2)t}\right) \\
&= \frac{1}{2}\left(\widetilde{y}_{0,0}^*(t)e^{-j0t} + \widetilde{y}_{0,0}(t)e^{j0t}\right) \\
&+ \frac{1}{2}\left(\widetilde{y}_{1,0}^*(t)e^{-j1\omega_1 t} + \widetilde{y}_{1,0}(t)e^{j1\omega_1 t}\right) \\
&+ \frac{1}{2}\left(\widetilde{y}_{0,1}^*(t)e^{-j1\omega_2 t} + \widetilde{y}_{0,1}(t)e^{j1\omega_2 t}\right) \\
&+ \frac{1}{2}\left(\widetilde{y}_{2,-1}^*(t)e^{-j(2\omega_1-\omega_2)t} + \widetilde{y}_{2,-1}(t)e^{j(2\omega_1-\omega_2)t}\right) \\
&+ \frac{1}{2}\left(\widetilde{y}_{-1,2}^*(t)e^{-j(2\omega_2-\omega_1)t} + \widetilde{y}_{-1,2}(t)e^{j(2\omega_2-\omega_1)t}\right) \\
&\;\vdots
\end{aligned}
\tag{4.29}
$$

$$+ \quad \frac{1}{2}\left(\widetilde{y}^*_{NL,0}(t)e^{-jNL\omega_1 t} + \widetilde{y}_{NL,0}(t)e^{jNL\omega_1 t}\right)$$

$$+ \quad \frac{1}{2}\left(\widetilde{y}^*_{0,NL}(t)e^{-jNL\omega_2 t} + \widetilde{y}_{0,NL}(t)e^{jNL\omega_2 t}\right),$$

Here, $\widetilde{y}_{0,0}(t)$ denotes the envelope at DC, $\widetilde{y}_{1,0}(t)$ and $\widetilde{y}_{0,1}(t)$ denote the envelopes of the first order in-band signals, and $\widetilde{y}_{2,-1}(t)$ and $\widetilde{y}_{-1,2}(t)$, denote the envelopes of the third order inter-band signals. Finally, $\widetilde{y}_{0,NL}(t)$ and $\widetilde{y}_{NL,0}(t)$, represent the first and second NL^{th} harmonics, respectively.

Step 3: Multi-frequency to passband only transformation:

Equating the terms on the right sides of 4.28 and 4.29 that share the same frequency range (fundamental, mixing products) yields a multi-frequency model consisting of several distinct equations that relate the output envelopes $\widetilde{y}_{p,q}(t)$ to $\widetilde{x}_1(t)$, $\widetilde{x}_2(t)$, ω_1 and ω_2. Since we are mainly interested in the relationship between the envelopes of the output and input signals around the two carriers' frequencies, only the passband components of the PA output are considered in the equation below:

$$\begin{aligned} y_{pb}(t) &= \frac{1}{2}\left(\widetilde{y}^*_{\omega_1}(t)e^{-j\omega_1 t} + \widetilde{y}_{\omega_1}(t)e^{j\omega_1 t}\right) \\ &+ \frac{1}{2}\left(\widetilde{y}^*_{\omega_2}(t)e^{-j\omega_2 t} + \widetilde{y}_{\omega_2}(t)e^{j\omega_2 t}\right) \\ &= \frac{1}{2}\left(y^*_{\omega_1}(t) + y_{\omega_1}(t)\right) + \frac{1}{2}\left(y^*_{\omega_2}(t) + y_{\omega_2}(t)\right), \end{aligned} \tag{4.30}$$

where $y_{\omega_1}(t) = \widetilde{y}_{\omega_1}(t)e^{j\omega_1 t}$ and $y_{\omega_2}(t) = \widetilde{y}_{\omega_2}(t)e^{j\omega_2 t}$

In the following a number of additional derivations are applied to produce the detailed expression for the first term in 4.30,$y_{\omega_1}(t)$, around the first frequency. Similar derivations can be used to produce the expression of the second frequency term, $y_{\omega_2}(t)$.

$y_{\omega_1}(t)$can be modeled as a summation of the Volterra series nonlinear terms $y_{\omega_1,2k+1}(t)$ of order $2k+1$. It can also be expressed as function of the envelops of the nonlinear terms, $y_{\omega_1,2k+1}(t)$, denoted hereafter $\widetilde{y}_{\omega_1,2k+1}(t)$ and the angular frequency ω_1 as follows:

$$y_{\omega_1}(t) = \sum_{k=0}^{\infty} y_{\omega_1,2k+1}(t) = \left(\sum_{k=0}^{\infty} \widetilde{y}_{\omega_1,2k+1}(t)\right)e^{j\omega_1 t} \tag{4.31}$$

It is worth noting that only odd powered terms are retained and even terms are discarded since they do not appear in the passband response. Equating the terms on the right sides of expanded 4.28 and 4.31 yields a continuous BBE DIDO Volterra series that

expresses $y_{\omega_1,2k+1}(t)$ as functions of $\widetilde{x}(t)$, and ω_1. Below is the expression for $y_{\omega_1,1}(t)$ and $y_{\omega_1,3}(t)$.

$$y_{\omega_1,1}(t) = \int_{-\infty}^{\infty} h_1\left(\tau_1\right) \cdot \widetilde{x}_1\left(t - \tau_1\right) \cdot e^{j\omega_1(t-\tau_1)} \cdot d\tau_1 \tag{4.32}$$

$$
\begin{aligned}
y_{\omega_1,3}(t) \;=\; & \int_{-\infty}^{\infty}\int_{-\infty}^{\infty}\int_{-\infty}^{\infty} h_3\left(\tau_1,\tau_2,\tau_3\right)\cdot\Big\{ \\
& \left(\widetilde{x}_1\left(t-\tau_1\right)\cdot e^{j\omega_1(t-\tau_1)}\right)\left(\widetilde{x}_1\left(t-\tau_2\right)\cdot e^{j\omega_1(t-\tau_2)}\right)\left(\widetilde{x}_1\left(t-\tau_3\right)\cdot e^{j\omega_1(t-\tau_3)}\right)^* \\
& +\left(\widetilde{x}_1\left(t-\tau_1\right)\cdot e^{j\omega_1(t-\tau_1)}\right)\left(\widetilde{x}_1\left(t-\tau_2\right)\cdot e^{j\omega_1(t-\tau_2)}\right)^*\left(\widetilde{x}_1\left(t-\tau_3\right)\cdot e^{j\omega_1(t-\tau_3)}\right) \\
& +\left(\widetilde{x}_1\left(t-\tau_1\right)\cdot e^{j\omega_1(t-\tau_1)}\right)^*\left(\widetilde{x}_1\left(t-\tau_2\right)\cdot e^{j\omega_1(t-\tau_2)}\right)\left(\widetilde{x}_1\left(t-\tau_3\right)\cdot e^{j\omega_1(t-\tau_3)}\right) \\
& +\left(\widetilde{x}_1\left(t-\tau_1\right)\cdot e^{j\omega_1(t-\tau_1)}\right)\left(\widetilde{x}_2\left(t-\tau_2\right)\cdot e^{j\omega_2(t-\tau_2)}\right)\left(\widetilde{x}_2\left(t-\tau_3\right)\cdot e^{j\omega_2(t-\tau_3)}\right)^* \\
& +\left(\widetilde{x}_1\left(t-\tau_1\right)\cdot e^{j\omega_1(t-\tau_1)}\right)\left(\widetilde{x}_2\left(t-\tau_2\right)\cdot e^{j\omega_2(t-\tau_2)}\right)^*\left(\widetilde{x}_2\left(t-\tau_3\right)\cdot e^{j\omega_2(t-\tau_3)}\right) \\
& +\left(\widetilde{x}_2\left(t-\tau_1\right)\cdot e^{j\omega_2(t-\tau_1)}\right)^*\left(\widetilde{x}_1\left(t-\tau_2\right)\cdot e^{j\omega_1(t-\tau_2)}\right)\left(\widetilde{x}_2\left(t-\tau_3\right)\cdot e^{j\omega_2(t-\tau_3)}\right) \\
& +\left(\widetilde{x}_2\left(t-\tau_1\right)\cdot e^{j\omega_2(t-\tau_1)}\right)\left(\widetilde{x}_1\left(t-\tau_2\right)\cdot e^{j\omega_1(t-\tau_2)}\right)\left(\widetilde{x}_2\left(t-\tau_3\right)\cdot e^{j\omega_2(t-\tau_3)}\right)^* \\
& +\left(\widetilde{x}_2\left(t-\tau_1\right)\cdot e^{j\omega_2(t-\tau_1)}\right)\left(\widetilde{x}_2\left(t-\tau_2\right)\cdot e^{j\omega_2(t-\tau_2)}\right)^*\left(\widetilde{x}_1\left(t-\tau_3\right)\cdot e^{j\omega_1(t-\tau_3)}\right) \\
& +\left(\widetilde{x}_2\left(t-\tau_1\right)\cdot e^{j\omega_2(t-\tau_1)}\right)^*\left(\widetilde{x}_2\left(t-\tau_2\right)\cdot e^{j\omega_2(t-\tau_2)}\right)\left(\widetilde{x}_1\left(t-\tau_3\right)\cdot e^{j\omega_1(t-\tau_3)}\right) \\
& \Big\}\cdot d\tau_3 d\tau_2 d\tau_1
\end{aligned}
\tag{4.33}
$$

Step 4: Continuous-time Passband to baseband equivalent transformation:

In order to be implementable in digital processor with manageable complexity, a passband model needs to be transformed into a baseband equivalent model. Such model enables mimicking the RF nonlinear dynamic distortion while applying all the computations in baseband at low sampling rate. The baseband equivalent model is obtained by frequency translating the passband Volterra series model to baseband. For that purpose, the continuous time passband Volterra series expressions of 4.32 and 4.33 are first rewritten in convolution form. The convolution form for $y_{\omega_1,1}(t)$ is given by:

$$y_{\omega_1,1}(t) = h_1\left(t\right) \star \left(\widetilde{x}_1\left(t\right)\cdot e^{j\omega_1 t}\right) \tag{4.34}$$

As can be seen, the transform of $y_{\omega_1,3}(t)$ is one-variable. However, the integrand in the right-hand side consists of a multivariate kernel $h_3(\tau_1,\tau_2,\tau_3)$ and thus the relevant transform would be a function of three variables s_1,s_2,s_3. To overcome this difference, it is in order to reassign the output as follow $y(t) = y(t_1,t_2,t_3)_{|t_1=t_2=t_3=t} \triangleq y(t,t,t)$ [38] and the Laplace transform is given as below

60

$$y_{\omega_1,3}(t_1, t_2, t_3) = h_3(t_1, t_2, t_3) \star \Bigg\{$$

$$\left(\widetilde{x}_1(t_1) \cdot e^{j\omega_1 t_1}\right)\left(\widetilde{x}_1(t_2) \cdot e^{j\omega_1 t_2}\right)\left(\widetilde{x}_1(t_3) \cdot e^{j\omega_1 t_3}\right)^*$$
$$+ \left(\widetilde{x}_1(t_1) \cdot e^{j\omega_1 t_1}\right)\left(\widetilde{x}_1(t_2) \cdot e^{j\omega_1 t_2}\right)^*\left(\widetilde{x}_1(t_3) \cdot e^{j\omega_1 t_3}\right)$$
$$+ \left(\widetilde{x}_1(t_1) \cdot e^{j\omega_1 t_1}\right)^*\left(\widetilde{x}_1(t_2) \cdot e^{j\omega_1 t_2}\right)\left(\widetilde{x}_1(t_3) \cdot e^{j\omega_1 t_3}\right)$$
$$+ \left(\widetilde{x}_1(t_1) \cdot e^{j\omega_1 t_1}\right)\left(\widetilde{x}_2(t_2) \cdot e^{j\omega_2 t_2}\right)\left(\widetilde{x}_2(t_3) \cdot e^{j\omega_2 t_3}\right)^*$$
$$+ \left(\widetilde{x}_1(t_1) \cdot e^{j\omega_1 t_1}\right)\left(\widetilde{x}_2(t_2) \cdot e^{j\omega_2 t_2}\right)^*\left(\widetilde{x}_2(t_3) \cdot e^{j\omega_2 t_3}\right)$$
$$+ \left(\widetilde{x}_2(t_1) \cdot e^{j\omega_2 t_1}\right)^*\left(\widetilde{x}_1(t_2) \cdot e^{j\omega_1 t_2}\right)\left(\widetilde{x}_2(t_3) \cdot e^{j\omega_2 t_3}\right)$$
$$+ \left(\widetilde{x}_2(t_1) \cdot e^{j\omega_2 t_1}\right)\left(\widetilde{x}_1(t_2) \cdot e^{j\omega_1 t_2}\right)\left(\widetilde{x}_2(t_3) \cdot e^{j\omega_2 t_3}\right)^*$$
$$+ \left(\widetilde{x}_2(t_1) \cdot e^{j\omega_2 t_1}\right)\left(\widetilde{x}_2(t_2) \cdot e^{j\omega_2 t_2}\right)^*\left(\widetilde{x}_1(t_3) \cdot e^{j\omega_1 t_3}\right)$$

$$+ \left(\widetilde{x}_2(t_1) \cdot e^{j\omega_2 t_1}\right)^*\left(\widetilde{x}_2(t_2) \cdot e^{j\omega_2 t_2}\right)\left(\widetilde{x}_1(t_3) \cdot e^{j\omega_1 t_3}\right) \Bigg\} \qquad (4.35)$$

The application of the Laplace transform to 4.34 and 4.35 yield the following expressions:

$$\begin{aligned}
Y_{\omega_1,1}(s) &= L\left(y_{\omega_1,1}(t)\right) \\
&= L\left(h_1(t)\right) \cdot L\left(\widetilde{x}_1(t) e^{j\omega_1 t}\right) \\
&= H_1(s) \cdot \widetilde{X}_1(s - j\omega_1).
\end{aligned} \qquad (4.36)$$

$$Y_{\omega_1,3}(s_1, s_2, s_3) = L\left(y_{\omega_1,3}(t_1, t_2, t_3)\right)$$

$$= L\left(h_3(t_1, t_2, t_3)\right) \cdot \Bigg\{$$

$$L\left(\left(\widetilde{x}_1(t_1) \cdot e^{j\omega_1 t_1}\right)\left(\widetilde{x}_1(t_2) \cdot e^{j\omega_1 t_2}\right)\left(\widetilde{x}_1(t_3) \cdot e^{j\omega_1 t_3}\right)^*\right)$$
$$+ L\left(\left(\widetilde{x}_1(t_1) \cdot e^{j\omega_1 t_1}\right)\left(\widetilde{x}_1(t_2) \cdot e^{j\omega_1 t_2}\right)^*\left(\widetilde{x}_1(t_3) \cdot e^{j\omega_1 t_3}\right)\right)$$
$$+ L\left(\left(\widetilde{x}_1(t_1) \cdot e^{j\omega_1 t_1}\right)^*\left(\widetilde{x}_1(t_2) \cdot e^{j\omega_1 t_2}\right)\left(\widetilde{x}_1(t_3) \cdot e^{j\omega_1 t_3}\right)\right)$$
$$+ L\left(\left(\widetilde{x}_1(t_1) \cdot e^{j\omega_1 t_1}\right)\left(\widetilde{x}_2(t_2) \cdot e^{j\omega_2 t_2}\right)\left(\widetilde{x}_2(t_3) \cdot e^{j\omega_2 t_3}\right)^*\right)$$
$$+ L\left(\left(\widetilde{x}_1(t_1) \cdot e^{j\omega_1 t_1}\right)\left(\widetilde{x}_2(t_2) \cdot e^{j\omega_2 t_2}\right)^*\left(\widetilde{x}_2(t_3) \cdot e^{j\omega_2 t_3}\right)\right)$$
$$+ L\left(\left(\widetilde{x}_2(t_1) \cdot e^{j\omega_2 t_1}\right)^*\left(\widetilde{x}_1(t_2) \cdot e^{j\omega_1 t_2}\right)\left(\widetilde{x}_2(t_3) \cdot e^{j\omega_2 t_3}\right)\right)$$

$$+L\left(\left(\widetilde{x}_2\left(t_1\right)\cdot e^{j\omega_2 t_1}\right)\left(\widetilde{x}_1\left(t_2\right)\cdot e^{j\omega_1 t_2}\right)\left(\widetilde{x}_2\left(t_3\right)\cdot e^{j\omega_2 t_3}\right)^*\right)$$

$$\left.\begin{aligned}&+L\left(\left(\widetilde{x}_2\left(t_1\right)\cdot e^{j\omega_2 t_1}\right)\left(\widetilde{x}_2\left(t_2\right)\cdot e^{j\omega_2 t_2}\right)^*\left(\widetilde{x}_1\left(t_3\right)\cdot e^{j\omega_1 t_3}\right)\right)\\&+L\left(\left(\widetilde{x}_2\left(t_1\right)\cdot e^{j\omega_2 t_1}\right)^*\left(\widetilde{x}_2\left(t_2\right)\cdot e^{j\omega_2 t_2}\right)\left(\widetilde{x}_1\left(t_3\right)\cdot e^{j\omega_1 t_3}\right)\right)\end{aligned}\right\}\quad(4.37)$$

$$Y_{\omega_1,3}(s_1,s_2,s_3)\;=\;L\left(h_3(t_1,t_2,t_3)\right)\cdot\Bigg\{$$ (4.38)

$$\begin{aligned}&L\left(\widetilde{x}_1\left(t_1\right)\cdot e^{j\omega_1 t_1}\right)L\left(\widetilde{x}_1\left(t_2\right)\cdot e^{j\omega_1 t_2}\right)L\left(\left(\widetilde{x}_1\left(t_3\right)\cdot e^{j\omega_1 t_3}\right)^*\right)\\&+L\left(\widetilde{x}_1\left(t_1\right)\cdot e^{j\omega_1 t_1}\right)L\left(\left(\widetilde{x}_1\left(t_2\right)\cdot e^{j\omega_1 t_2}\right)^*\right)L\left(\widetilde{x}_1\left(t_3\right)\cdot e^{j\omega_1 t_3}\right)\\&+L\left(\left(\widetilde{x}_1\left(t_1\right)\cdot e^{j\omega_1 t_1}\right)^*\right)L\left(\widetilde{x}_1\left(t_2\right)\cdot e^{j\omega_1 t_2}\right)L\left(\widetilde{x}_1\left(t_3\right)\cdot e^{j\omega_1 t_3}\right)\\&+L\left(\widetilde{x}_1\left(t_1\right)\cdot e^{j\omega_1 t_1}\right)L\left(\widetilde{x}_2\left(t_2\right)\cdot e^{j\omega_2 t_2}\right)L\left(\left(\widetilde{x}_2\left(t_3\right)\cdot e^{j\omega_2 t_3}\right)^*\right)\\&+L\left(\widetilde{x}_1\left(t_1\right)\cdot e^{j\omega_1 t_1}\right)L\left(\left(\widetilde{x}_2\left(t_2\right)\cdot e^{j\omega_2 t_2}\right)^*\right)L\left(\widetilde{x}_2\left(t_3\right)\cdot e^{j\omega_2 t_3}\right)\\&+L\left(\left(\widetilde{x}_2\left(t_1\right)\cdot e^{j\omega_2 t_1}\right)^*\right)L\left(\widetilde{x}_1\left(t_2\right)\cdot e^{j\omega_1 t_2}\right)L\left(\widetilde{x}_2\left(t_3\right)\cdot e^{j\omega_2 t_3}\right)\\&+L\left(\widetilde{x}_2\left(t_1\right)\cdot e^{j\omega_2 t_1}\right)L\left(\widetilde{x}_1\left(t_2\right)\cdot e^{j\omega_1 t_2}\right)L\left(\left(\widetilde{x}_2\left(t_3\right)\cdot e^{j\omega_2 t_3}\right)^*\right)\\&+L\left(\widetilde{x}_2\left(t_1\right)\cdot e^{j\omega_2 t_1}\right)L\left(\left(\widetilde{x}_2\left(t_2\right)\cdot e^{j\omega_2 t_2}\right)^*\right)L\left(\widetilde{x}_1\left(t_3\right)\cdot e^{j\omega_1 t_3}\right)\\&+L\left(\left(\widetilde{x}_2\left(t_1\right)\cdot e^{j\omega_2 t_1}\right)^*\right)L\left(\widetilde{x}_2\left(t_2\right)\cdot e^{j\omega_2 t_2}\right)L\left(\widetilde{x}_1\left(t_3\right)\cdot e^{j\omega_1 t_3}\right)\Bigg\}\end{aligned}$$

$$=\;H_3(s_1,s_2,s_3)\cdot\Bigg\{$$

$$\begin{aligned}&\widetilde{X}_1\left(s_1-j\omega_1\right)\cdot\widetilde{X}_1\left(s_2-j\omega_1\right)\cdot\widetilde{X}_1^*\left((s_3-j\omega_1)^*\right)\\&+\widetilde{X}_1\left(s_1-j\omega_1\right)\cdot\widetilde{X}_1^*\left((s_2-j\omega_1)^*\right)\cdot\widetilde{X}_1\left(s_3-j\omega_1\right)\\&+\widetilde{X}_1^*\left((s_1-j\omega_1)^*\right)\cdot\widetilde{X}_1\left(s_2-j\omega_1\right)\cdot\widetilde{X}_1\left(s_3-j\omega_1\right)\\&+\widetilde{X}_1\left(s_1-j\omega_1\right)\cdot\widetilde{X}_2\left(s_2-j\omega_2\right)\cdot\widetilde{X}_2^*\left((s_3-j\omega_2)^*\right)\\&+\widetilde{X}_1\left(s_1-j\omega_1\right)\cdot\widetilde{X}_2^*\left((s_2-j\omega_2)^*\right)\cdot\widetilde{X}_2\left(s_3-j\omega_2\right)\\&+\widetilde{X}_2^*\left((s_1-j\omega_2)^*\right)\cdot\widetilde{X}_1\left(s_2-j\omega_1\right)\cdot\widetilde{X}_2\left(s_3-j\omega_2\right)\\&+\widetilde{X}_2\left(s_1-j\omega_2\right)\cdot\widetilde{X}_1\left(s_2-j\omega_1\right)\cdot\widetilde{X}_2^*\left((s_3-j\omega_2)^*\right)\\&+\widetilde{X}_2\left(s_1-j\omega_2\right)\cdot\widetilde{X}_2^*\left((s_2-j\omega_2)^*\right)\cdot\widetilde{X}_1\left(s_3-j\omega_1\right)\\&+\widetilde{X}_2^*\left((s_1-j\omega_2)^*\right)\cdot\widetilde{X}_2\left(s_2-j\omega_2\right)\cdot\widetilde{X}_1\left(s_3-j\omega_1\right)\Bigg\}\end{aligned}$$ (4.39)

The above derivation utilizes the distributivity and product transformation properties of the multi-variate Laplace function [38]. Since $\widetilde{X}_1$ and $\widetilde{X}_2$ are band limited signals, the third order distortion terms in 4.39 are non-zero only in a range of a frequency intervals. For example, $\widetilde{X}_1\left(s_1 - j\omega_1\right) \cdot \widetilde{X}_2\left(s_2 - j\omega_2\right) \cdot \widetilde{X}_2^*\left((s_3 - j\omega_2)^*\right)$ is non-zero only when $s_1 \in I_1$, $s_2 \in I_2$, $s_3 \in I_2$, where

$$I_1 = \left[\omega_1 - \frac{B}{2}, \omega_1 + \frac{B}{2}\right] \;\; ; \;\; I_2 = \left[\omega_2 - \frac{B}{2}, \omega_2 + \frac{B}{2}\right]$$

where B designates the bandwidth of the distortion term. Accordingly, one can redefine $H_3(s_1, s_2, s_3)$ as follows:

$$H_3(s_1, s_2, s_3) = \left\{ \begin{array}{l} H_{3,s}(s_1, s_2, s_3) \;\; for \;\; s_i \in I_1 \,, \, i = 1,2,3 \\ H_{3,d1}(s_1, s_2, s_3) \;\; for \;\; s_1 \in I_1 \,, \, s_i \in I_2 \,, \, i = 2,3 \\ H_{3,d2}(s_1, s_2, s_3) \;\; for \;\; s_2 \in I_1 \,, \, s_i \in I_2 \,, \, i = 1,3 \\ H_{3,d3}(s_1, s_2, s_3) \;\; for \;\; s_3 \in I_1 \,, \, s_i \in I_2 \,, \, i = 1,2 \end{array} \right\}$$

Hence, 4.39 can be rewritten as

$$Y_{\omega_1,3}(s_1, s_2, s_3) = Y_{\omega_1,3,\,1}(s_1, s_2, s_3) + Y_{\omega_1,,3,\,2}(s_1, s_2, s_3) + Y_{\omega_1,3,\,3}(s_1, s_2, s_3) + Y_{\omega_1,3,\,4}(s_1, s_2, s_3)$$

where

$$\begin{aligned} Y_{\omega_1,3,\,1}(s_1, s_2, s_3) \;\; = \;\; & H_{3,s}(s_1, s_2, s_3) \cdot \Big\{ \\ & \widetilde{X}_1\left(s_1 - j\omega_1\right) \cdot \widetilde{X}_1\left(s_2 - j\omega_1\right) \cdot \widetilde{X}_1^*\left((s_3 - j\omega_1)^*\right) \\ & + \widetilde{X}_1\left(s_1 - j\omega_1\right) \cdot \widetilde{X}_1^*\left((s_2 - j\omega_1)^*\right) \cdot \widetilde{X}_1\left(s_3 - j\omega_1\right) \\ & + \widetilde{X}_1^*\left((s_1 - j\omega_1)^*\right) \cdot \widetilde{X}_1\left(s_2 - j\omega_1\right) \cdot \widetilde{X}_1\left(s_3 - j\omega_1\right) \Big\} \end{aligned}$$

$$\begin{aligned} Y_{\omega_1,3,\,2}(s_1, s_2, s_3) \;\; = \;\; & H_{3,d1}(s_1, s_2, s_3) \cdot \Big\{ \\ & \widetilde{X}_1\left(s_1 - j\omega_1\right) \cdot \widetilde{X}_2\left(s_2 - j\omega_2\right) \cdot \widetilde{X}_2^*\left((s_3 - j\omega_2)^*\right) \\ & + \widetilde{X}_1\left(s_1 - j\omega_1\right) \cdot \widetilde{X}_2^*\left((s_2 - j\omega_2)^*\right) \cdot \widetilde{X}_2\left(s_3 - j\omega_2\right) \Big\} \end{aligned}$$

$$Y_{\omega_1,3,3}(s_1, s_2, s_3) = H_{3,d2}(s_1, s_2, s_3) \cdot \Bigg\{$$

$$\widetilde{X}_2^* \left((s_1 - j\omega_2)^*\right) \cdot \widetilde{X}_1 \left(s_2 - j\omega_1\right) \cdot \widetilde{X}_2 \left(s_3 - j\omega_2\right)$$

$$+ \widetilde{X}_2 \left(s_1 - j\omega_2\right) \cdot \widetilde{X}_1 \left(s_2 - j\omega_1\right) \cdot \widetilde{X}_2^* \left((s_3 - j\omega_2)^*\right) \Bigg\}$$

$$Y_{\omega_1,3,4}(s_1, s_2, s_3) = H_{3,d3}(s_1, s_2, s_3) \cdot \Bigg\{$$

$$\widetilde{X}_2 \left(s_1 - j\omega_2\right) \cdot \widetilde{X}_2^* \left((s_2 - j\omega_2)^*\right) \cdot \widetilde{X}_1 \left(s_3 - j\omega_1\right)$$

$$+ \widetilde{X}_2^* \left((s_1 - j\omega_2)^*\right) \cdot \widetilde{X}_2 \left(s_2 - j\omega_2\right) \cdot \widetilde{X}_1 \left(s_3 - j\omega_1\right) \Bigg\} \quad (4.40)$$

Exploiting the symmetry of $H_3(s_1, s_2, s_3)$ [23], which yields the following relation

$$H_3(s_1, s_2, s_3) = H_3(s_2, s_1, s_3) = H_3(s_3, s_2, s_1) \forall s_1, s_2, s_3$$

One can deduce the following equalities

$$H_{3,d1}(s_1, s_2, s_3) = H_{3,d2}(s_2, s_1, s_3) = H_{3,d3}(s_3, s_2, s_1)$$

Consequently a single kernel $H_{3,d}$ can be used instead of the three separate ones where only the variable order is adjusted each time as shown below:

$$H_{3,d1}(s_1, s_2, s_3) = H_{3,d}(s_1, s_2, s_3)$$

$$H_{3,d2}(s_1, s_2, s_3) = H_{3,d}(s_2, s_1, s_3)$$

$$H_{3,d3}(s_1, s_2, s_3) = H_{3,d}(s_3, s_2, s_1) \quad (4.41)$$

Substituting 4.41 in 4.40 yields a new expression

$$Y_{\omega_1,3,1}(s_1, s_2, s_3) = H_{3,s}(s_1, s_2, s_3) \cdot \Bigg\{$$

64

$$\widetilde{X}_1\left(s_1 - j\omega_1\right) \cdot \widetilde{X}_1\left(s_2 - j\omega_1\right) \cdot \widetilde{X}_1^*\left((s_3 - j\omega_1)^*\right)$$

$$+\widetilde{X}_1\left(s_1 - j\omega_1\right) \cdot \widetilde{X}_1^*\left((s_2 - j\omega_1)^*\right) \cdot \widetilde{X}_1\left(s_3 - j\omega_1\right)$$

$$+\widetilde{X}_1^*\left((s_1 - j\omega_1)^*\right) \cdot \widetilde{X}_1\left(s_2 - j\omega_1\right) \cdot \widetilde{X}_1\left(s_3 - j\omega_1\right) \Bigg\}$$

$$Y_{\omega_1,3,\,2}(s_1, s_2, s_3) \;=\; H_{3,d}(s_1, s_2, s_3) \cdot \Bigg\{$$

$$\widetilde{X}_1\left(s_1 - j\omega_1\right) \cdot \widetilde{X}_2\left(s_2 - j\omega_2\right) \cdot \widetilde{X}_2^*\left((s_3 - j\omega_2)^*\right)$$

$$+\widetilde{X}_1\left(s_1 - j\omega_1\right) \cdot \widetilde{X}_2^*\left((s_2 - j\omega_2)^*\right) \cdot \widetilde{X}_2\left(s_3 - j\omega_2\right) \Bigg\}$$

$$Y_{\omega_1,3,\,3}(s_1, s_2, s_3) \;=\; H_{3,d}(s_2, s_1, s_3) \cdot \Bigg\{$$

$$\widetilde{X}_2^*\left((s_1 - j\omega_2)^*\right) \cdot \widetilde{X}_1\left(s_2 - j\omega_1\right) \cdot \widetilde{X}_2\left(s_3 - j\omega_2\right)$$

$$+\widetilde{X}_2\left(s_1 - j\omega_2\right) \cdot \widetilde{X}_1\left(s_2 - j\omega_1\right) \cdot \widetilde{X}_2^*\left((s_3 - j\omega_2)^*\right) \Bigg\}$$

$$Y_{\omega_1,3,\,4}(s_1, s_2, s_3) \;=\; H_{3,d}(s_3, s_2, s_1) \cdot \Bigg\{$$

$$\widetilde{X}_2\left(s_1 - j\omega_2\right) \cdot \widetilde{X}_2^*\left((s_2 - j\omega_2)^*\right) \cdot \widetilde{X}_1\left(s_3 - j\omega_1\right)$$

$$+\widetilde{X}_2^*\left((s_1 - j\omega_2)^*\right) \cdot \widetilde{X}_2\left(s_2 - j\omega_2\right) \cdot \widetilde{X}_1\left(s_3 - j\omega_1\right) \Bigg\} \qquad (4.42)$$

The application of a frequency translation in Laplace domain to 4.36 and 4.42 allows for passband to baseband equivalent transformation of $y_{\omega_1,1}$.and $y_{\omega_1,3}(t)$ in the time domain. The frequency translation of $j\omega_1$ is performed by replacing s_i in 4.36 an 4.42 with $u_i = s_i + j\omega_1$; i =1,2,3. Hence, the application of the frequency translation to $Y_{\omega_1,1}(s)$, $Y_{\omega_1,3}(s_1, s_2, s_3)$, $H_1(s)$, $H_{3,s}(s_1, s_2, s_3)$, and $H_{3,d}(s_1, s_2, s_3)$ yields the following baseband equivalent expressions in the Laplace domain:

$$\widetilde{Y}_{\omega_1,1}(u_1) \;=\; Y_{\omega_1,1}(u_1 + j\omega_1)$$

65

$$
\begin{aligned}
&= \ H_1(u_1 + j\omega_1) \cdot \widetilde{X}_1(u_1) \\
&= \ \widetilde{H}_1(u_1) \cdot \widetilde{X}_1(u_1).
\end{aligned}
\tag{4.43}
$$

$$
\begin{aligned}
\widetilde{Y}_{\omega_1,3}(u_1, u_2, u_3) \ &= \ \widetilde{Y}_{\omega_1,3,1}(u_1, u_2, u_3) + \widetilde{Y}_{\omega_1,,3,2}(u_1, u_2, u_3) \tag{4.44} \\
&+ \ \widetilde{Y}_{\omega_1,3,3}(u_1, u_2, u_3) + \widetilde{Y}_{\omega_1,3,4}(u_1, u_2, u_3) \tag{4.45}
\end{aligned}
$$

where

$$
\begin{aligned}
\widetilde{Y}_{\omega_1,3,1}(u_1, u_2, u_3) \ &= \ Y_{\omega_1,3,1}(u_1 + j\omega_1, u_2 + j\omega_1, u_3 + j\omega_1) \\
&= \ H_{3,s}(u_1 + j\omega_1, u_2 + j\omega_1, u_3 + j\omega_1) \cdot \Bigg\{ \\
&\qquad \widetilde{X}_1(u_1) \cdot \widetilde{X}_1(u_2) \cdot \widetilde{X}_1^*((u_3)^*) \\
&\quad + \widetilde{X}_1(u_1) \cdot \widetilde{X}_1^*((u_2)^*) \cdot \widetilde{X}_1(u_3) \\
&\quad + \widetilde{X}_1^*((u_1)^*) \cdot \widetilde{X}_1(u_2) \cdot \widetilde{X}_1(u_3) \Bigg\} \\
&= \ \widetilde{H}_{3,s}(u_1, u_2, u_3) \cdot \Bigg\{ \\
&\qquad \widetilde{X}_1(u_1) \cdot \widetilde{X}_1(u_2) \cdot \widetilde{X}_1^*((u_3)^*) \\
&\quad + \widetilde{X}_1(u_1) \cdot \widetilde{X}_1^*((u_2)^*) \cdot \widetilde{X}_1(u_3) \\
&\quad + \widetilde{X}_1^*((u_1)^*) \cdot \widetilde{X}_1(u_2) \cdot \widetilde{X}_1(u_3) \Bigg\}
\end{aligned}
$$

$$
\begin{aligned}
\widetilde{Y}_{\omega_1,3,2}(u_1, u_2, u_3) \ &= \ Y_{\omega_1,3,2}(u_1 + j\omega_1, u_2 + j\omega_2, u_3 + j\omega_2) \\
&= \ H_{3,d}(u_1 + j\omega_1, u_2 + j\omega_2, u_3 + j\omega_2) \cdot \Bigg\{ \\
&\qquad \widetilde{X}_1(u_1) \cdot \widetilde{X}_2(u_2) \cdot \widetilde{X}_2^*((u_3)^*) \\
&\quad + \widetilde{X}_1(u_1) \cdot \widetilde{X}_2^*((u_2)^*) \cdot \widetilde{X}_2(u_3) \Bigg\}
\end{aligned}
$$

$$
\begin{aligned}
&= \quad \widetilde{H}_{3,d}(u_1, u_2, u_3) \cdot \Bigg\{ \\
&\qquad \widetilde{X}_1(u_1) \cdot \widetilde{X}_2(u_2) \cdot \widetilde{X}_2^*((u_3)^*) \\
&\qquad + \widetilde{X}_1(u_1) \cdot \widetilde{X}_2^*((u_2)^*) \cdot \widetilde{X}_2(u_3) \Bigg\}
\end{aligned}
$$

$$
\begin{aligned}
\widetilde{Y}_{\omega_1,3,3}(u_1, u_2, u_3) &= \quad Y_{\omega_1,3,3}(u_1 + j\omega_2, u_2 + j\omega_1, u_3 + j\omega_2) \\
&= \quad H_{3,d}(u_2 + j\omega_1, u_1 + j\omega_2, u_3 + j\omega_2) \cdot \Bigg\{ \\
&\qquad \widetilde{X}_2^*((u_1)^*) \cdot \widetilde{X}_1(u_2) \cdot \widetilde{X}_2(u_3) \\
&\qquad + \widetilde{X}_2(u_1) \cdot \widetilde{X}_1(u_2) \cdot \widetilde{X}_2^*((u_3)^*) \Bigg\} \\
&= \quad \widetilde{H}_{3,d}(u_2, u_1, u_3) \cdot \Bigg\{ \\
&\qquad \widetilde{X}_2^*((u_1)^*) \cdot \widetilde{X}_1(u_2) \cdot \widetilde{X}_2(u_3) \\
&\qquad + \widetilde{X}_2(u_1) \cdot \widetilde{X}_1(u_2) \cdot \widetilde{X}_2^*((u_3)^*) \Bigg\}
\end{aligned}
$$

$$
\begin{aligned}
\widetilde{Y}_{\omega_1,3,4}(u_1, u_2, u_3) &= \quad Y_{\omega_1,3,4}(u_1 + j\omega_2, u_2 + j\omega_2, u_3 + j\omega_1) \\
&= \quad H_{3,d}(u_3 + j\omega_1, u_2 + j\omega_2, u_1 + j\omega_2) \cdot \Bigg\{ \\
&\qquad \widetilde{X}_2(u_1) \cdot \widetilde{X}_2^*((u_2)^*) \cdot \widetilde{X}_1(u_3) \\
&\qquad + \widetilde{X}_2^*((u_1)^*) \cdot \widetilde{X}_2(u_2) \cdot \widetilde{X}_1(u_3) \Bigg\} \\
&= \quad \widetilde{H}_{3,d}(u_3, u_2, u_1) \cdot \Bigg\{ \\
&\qquad \widetilde{X}_2(u_1) \cdot \widetilde{X}_2^*((u_2)^*) \cdot \widetilde{X}_1(u_3) \\
&\qquad + \widetilde{X}_2^*((u_1)^*) \cdot \widetilde{X}_2(u_2) \cdot \widetilde{X}_1(u_3) \Bigg\}
\end{aligned}
$$

The application of the inverse Laplace to 4.43 and 4.44 yields the following time domain expressions of the baseband equivalent terms:

$$\widetilde{y}_{\omega_1,1}(t) = \int_{-\infty}^{\infty} \widetilde{h}_1(\tau_1) \cdot \widetilde{x}_1(t - \tau_1) \cdot d\tau_1$$

$$\widetilde{y}_{\omega_1,3,1}(t) = \int_{-\infty}^{\infty}\int_{-\infty}^{\infty}\int_{-\infty}^{\infty} \widetilde{h}_{3,s}(\tau_1, \tau_2, \tau_3) \cdot \Big\{ \\ (\widetilde{x}_1(t-\tau_1))(\widetilde{x}_1(t-\tau_2))(\widetilde{x}_1(t-\tau_3))^* \\ + (\widetilde{x}_1(t-\tau_1))(\widetilde{x}_1(t-\tau_2))^*(\widetilde{x}_1(t-\tau_3)) \\ + (\widetilde{x}_1(t-\tau_1))^*(\widetilde{x}_1(t-\tau_2))(\widetilde{x}_1(t-\tau_3)) \Big\} \cdot d\tau_3 d\tau_2 d\tau_1$$

$$\widetilde{y}_{\omega_1,3,2}(t) = \int_{-\infty}^{\infty}\int_{-\infty}^{\infty}\int_{-\infty}^{\infty} \widetilde{h}_{3,d}(\tau_1, \tau_2, \tau_3) \cdot \Big\{ \\ (\widetilde{x}_1(t-\tau_1))(\widetilde{x}_2(t-\tau_2))(\widetilde{x}_2(t-\tau_3))^* \\ + (\widetilde{x}_1(t-\tau_1))(\widetilde{x}_2(t-\tau_2))^*(\widetilde{x}_2(t-\tau_3)) \Big\} \cdot d\tau_3 d\tau_2 d\tau_1$$

$$\widetilde{y}_{\omega_1,3,3}(t) = \int_{-\infty}^{\infty}\int_{-\infty}^{\infty}\int_{-\infty}^{\infty} \widetilde{h}_{3,d}(\tau_2, \tau_1, \tau_3) \cdot \Big\{ \\ (\widetilde{x}_2(t-\tau_1))^*(\widetilde{x}_1(t-\tau_2))(\widetilde{x}_2(t-\tau_3)) \\ + (\widetilde{x}_2(t-\tau_1))(\widetilde{x}_1(t-\tau_2))(\widetilde{x}_2(t-\tau_3))^* \Big\} \cdot d\tau_3 d\tau_2 d\tau_1$$

$$\widetilde{y}_{\omega_1,3,4}(t) = \int_{-\infty}^{\infty}\int_{-\infty}^{\infty}\int_{-\infty}^{\infty} \widetilde{h}_{3,d}(\tau_3, \tau_2, \tau_1) \cdot \Big\{ \\ (\widetilde{x}_2(t-\tau_1))(\widetilde{x}_2(t-\tau_2))^*(\widetilde{x}_1(t-\tau_3)) \\ + (\widetilde{x}_2(t-\tau_1))^*(\widetilde{x}_2(t-\tau_2))(\widetilde{x}_1(t-\tau_3)) \Big\} \cdot d\tau_3 d\tau_2 d\tau_1$$

Swapping τ_2 with τ_1 in $\widetilde{y}_{\omega_1,3,3}(t)$ and τ_3 with τ_1 in $\widetilde{y}_{\omega_1,3,4}$ yields the following equality

$$\widetilde{y}_{\omega_1,3,2}(t) = \widetilde{y}_{\omega_1,3,3}(t) = \widetilde{y}_{\omega_1,3,4}(t)$$

68
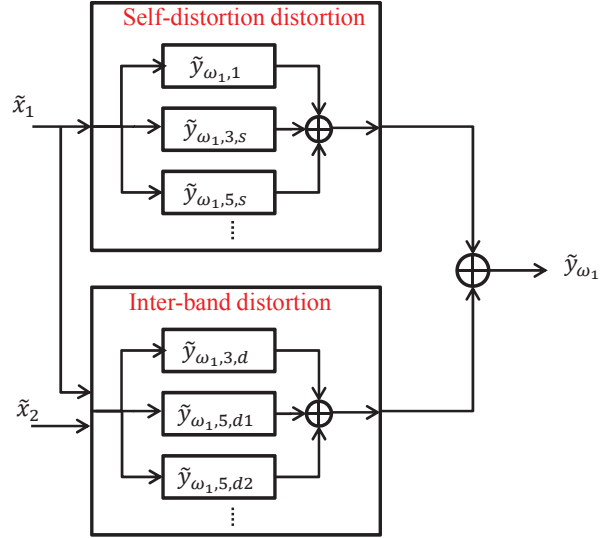
Figure 4.8: Dual band BBE Volterra model

Hence, the third order baseband equivalent Volterra term could be re-written as:

$$\widetilde{y}_{\omega_1,3}(t) = \widetilde{y}_{\omega_1,3,1}(t) + 3\widetilde{y}_{\omega_1,3,2}(t) = \widetilde{y}_{\omega_1,3,s}(t) + \widetilde{y}_{\omega_1,3,d}(t)$$

where $\widetilde{y}_{\omega_1,3,s}(t) = \widetilde{y}_{\omega_1,3,1}(t)$ designates the PA third order single-band self-distortion term and $\widetilde{y}_{\omega_1,3,d}(t) = 3\widetilde{y}_{\omega_1,3,2}(t)$ denotes the PA third order dual-band inter-band-distortion term, as shown in Fig. 4.8.

The same derivations were applied to construct the fifth order Volterra distortion term expression which is found to be

$$\widetilde{y}_{\omega_1,5}(t) = \widetilde{y}_{\omega_1,5,s}(t) + \widetilde{y}_{\omega_1,5,d1}(t) + \widetilde{y}_{\omega_1,5,d2}(t)$$

where

$$\widetilde{y}_{\omega_1,5,s}(t) = \int_{-\infty}^{\infty} \int_{-\infty}^{\infty} \int_{-\infty}^{\infty} \int_{-\infty}^{\infty} \int_{-\infty}^{\infty} \widetilde{h}_{5,s}\left(\tau_1, \tau_2, \tau_3, \tau_4, \tau_5\right) \cdot \Bigg\{$$

69

$$\widetilde{x}_1\left(t-\tau_1\right)\widetilde{x}_1\left(t-\tau_2\right)\widetilde{x}_1\left(t-\tau_3\right)\widetilde{x}_1^*\left(t-\tau_4\right)\widetilde{x}_1^*\left(t-\tau_5\right)$$
$$+\widetilde{x}_1\left(t-\tau_1\right)\widetilde{x}_1\left(t-\tau_2\right)\widetilde{x}_1^*\left(t-\tau_3\right)\widetilde{x}_1\left(t-\tau_4\right)\widetilde{x}_1^*\left(t-\tau_5\right)$$
$$+\widetilde{x}_1\left(t-\tau_1\right)\widetilde{x}_1^*\left(t-\tau_2\right)\widetilde{x}_1\left(t-\tau_3\right)\widetilde{x}_1\left(t-\tau_4\right)\widetilde{x}_1^*\left(t-\tau_5\right)$$
$$+\widetilde{x}_1^*\left(t-\tau_1\right)\widetilde{x}_1\left(t-\tau_2\right)\widetilde{x}_1\left(t-\tau_3\right)\widetilde{x}_1\left(t-\tau_4\right)\widetilde{x}_1^*\left(t-\tau_5\right)$$
$$+\widetilde{x}_1\left(t-\tau_1\right)\widetilde{x}_1\left(t-\tau_2\right)\widetilde{x}_1^*\left(t-\tau_3\right)\widetilde{x}_1^*\left(t-\tau_4\right)\widetilde{x}_1\left(t-\tau_5\right)$$
$$+\widetilde{x}_1\left(t-\tau_1\right)\widetilde{x}_1^*\left(t-\tau_2\right)\widetilde{x}_1\left(t-\tau_3\right)\widetilde{x}_1^*\left(t-\tau_4\right)\widetilde{x}_1\left(t-\tau_5\right)$$
$$+\widetilde{x}_1^*\left(t-\tau_1\right)\widetilde{x}_1\left(t-\tau_2\right)\widetilde{x}_1\left(t-\tau_3\right)\widetilde{x}_1^*\left(t-\tau_4\right)\widetilde{x}_1\left(t-\tau_5\right)$$
$$+\widetilde{x}_1\left(t-\tau_1\right)\widetilde{x}_1^*\left(t-\tau_2\right)\widetilde{x}_1^*\left(t-\tau_3\right)\widetilde{x}_1\left(t-\tau_4\right)\widetilde{x}_1\left(t-\tau_5\right)$$

$$+\widetilde{x}_1^*\left(t-\tau_1\right)\widetilde{x}_1\left(t-\tau_2\right)\widetilde{x}_1^*\left(t-\tau_3\right)\widetilde{x}_1\left(t-\tau_4\right)\widetilde{x}_1\left(t-\tau_5\right)$$

$$\left.+\widetilde{x}_1^*\left(t-\tau_1\right)\widetilde{x}_1^*\left(t-\tau_2\right)\widetilde{x}_1\left(t-\tau_3\right)\widetilde{x}_1\left(t-\tau_4\right)\widetilde{x}_1\left(t-\tau_5\right)\right\}$$

$$\widetilde{y}_{\omega_1,5,d1}(t)\;=\;\int_{-\infty}^{\infty}\int_{-\infty}^{\infty}\int_{-\infty}^{\infty}\int_{-\infty}^{\infty}\int_{-\infty}^{\infty}\widetilde{h}_{5,d1}\left(\tau_1,\tau_2,\tau_3,\tau_4,\tau_5\right)\cdot\left\{\vphantom{\int}\right.$$

$$\widetilde{x}_1\left(t-\tau_1\right)\widetilde{x}_1\left(t-\tau_2\right)\widetilde{x}_1^*\left(t-\tau_3\right)\widetilde{x}_2\left(t-\tau_4\right)\widetilde{x}_2^*\left(t-\tau_5\right)$$
$$+\widetilde{x}_1\left(t-\tau_1\right)\widetilde{x}_1^*\left(t-\tau_2\right)\widetilde{x}_1\left(t-\tau_3\right)\widetilde{x}_2\left(t-\tau_4\right)\widetilde{x}_2^*\left(t-\tau_5\right)$$
$$+\widetilde{x}_1^*\left(t-\tau_1\right)\widetilde{x}_1\left(t-\tau_2\right)\widetilde{x}_1\left(t-\tau_3\right)\widetilde{x}_2\left(t-\tau_4\right)\widetilde{x}_2^*\left(t-\tau_5\right)$$
$$+\widetilde{x}_1\left(t-\tau_1\right)\widetilde{x}_1\left(t-\tau_2\right)\widetilde{x}_1^*\left(t-\tau_3\right)\widetilde{x}_2^*\left(t-\tau_4\right)\widetilde{x}_2\left(t-\tau_5\right)$$
$$+\widetilde{x}_1\left(t-\tau_1\right)\widetilde{x}_1^*\left(t-\tau_2\right)\widetilde{x}_1\left(t-\tau_3\right)\widetilde{x}_2^*\left(t-\tau_4\right)\widetilde{x}_2\left(t-\tau_5\right)$$

$$\left.+\widetilde{x}_1^*\left(t-\tau_1\right)\widetilde{x}_1\left(t-\tau_2\right)\widetilde{x}_1\left(t-\tau_3\right)\widetilde{x}_2^*\left(t-\tau_4\right)\widetilde{x}_2\left(t-\tau_5\right)\right\}$$

$$\widetilde{y}_{\omega_1,5,d2}(t)\;=\;\int_{-\infty}^{\infty}\int_{-\infty}^{\infty}\int_{-\infty}^{\infty}\int_{-\infty}^{\infty}\int_{-\infty}^{\infty}\widetilde{h}_{5,d2}\left(\tau_1,\tau_2,\tau_3,\tau_4,\tau_5\right)\cdot\left\{\vphantom{\int}\right.$$

$$\widetilde{x}_1\left(t-\tau_1\right)\widetilde{x}_2\left(t-\tau_2\right)\widetilde{x}_2\left(t-\tau_3\right)\widetilde{x}_2^*\left(t-\tau_4\right)\widetilde{x}_2^*\left(t-\tau_5\right)$$
$$+\widetilde{x}_1\left(t-\tau_1\right)\widetilde{x}_2\left(t-\tau_2\right)\widetilde{x}_2^*\left(t-\tau_3\right)\widetilde{x}_2\left(t-\tau_4\right)\widetilde{x}_2^*\left(t-\tau_5\right)$$
$$+\widetilde{x}_1^*\left(t-\tau_1\right)\widetilde{x}_2^*\left(t-\tau_2\right)\widetilde{x}_2\left(t-\tau_3\right)\widetilde{x}_2\left(t-\tau_4\right)\widetilde{x}_2^*\left(t-\tau_5\right)$$
$$+\widetilde{x}_1\left(t-\tau_1\right)\widetilde{x}_2\left(t-\tau_2\right)\widetilde{x}_2^*\left(t-\tau_3\right)\widetilde{x}_2^*\left(t-\tau_4\right)\widetilde{x}_2\left(t-\tau_5\right)$$
$$+\widetilde{x}_1\left(t-\tau_1\right)\widetilde{x}_2^*\left(t-\tau_2\right)\widetilde{x}_2\left(t-\tau_3\right)\widetilde{x}_2^*\left(t-\tau_4\right)\widetilde{x}_2\left(t-\tau_5\right)$$

$$\left.+\widetilde{x}_1\left(t-\tau_1\right)\widetilde{x}_2^*\left(t-\tau_2\right)\widetilde{x}_2^*\left(t-\tau_3\right)\widetilde{x}_2\left(t-\tau_4\right)\widetilde{x}_2\left(t-\tau_5\right)\right\}$$

Hence, the continuous-time dual-band baseband equivalent Volterra series model for each band is given by:

$$\widetilde{y}_{\omega_1}(t) = \widetilde{y}_{\omega_1,1}(t) + \widetilde{y}_{\omega_1,3}(t) + \widetilde{y}_{\omega_1,5}(t) + \cdots \tag{4.46}$$

Step 5: Discrete-time baseband equivalent Volterra series model:

In order to implement the dual band BBE Volterra model in a digital processor, the following signal and systems properties and approximations are used to further simplify 4.46.

1. Truncation of the Volterra model to a finite nonlinearity order NL, generally in the range of 5 to 7.

2. Limitation of the integral bounds $(-\infty, +\infty)$ to $(0, T_\infty)$ using the signal and system causality, and the fading memory assumption (transient response time invariant Volterra series is defined as $t < T_\infty$). Since the impulse responses of different Volterra kernels, i.e. $\widetilde{h}_{\omega_1,1}, \widetilde{h}_{\omega_1,3,s}, \widetilde{h}_{\omega_1,3,d}, \widetilde{h}_{\omega_1,5,s}, \ldots$, represent different aspects of the system, the memory spans used in the computation of the different distortion terms can be set to be different.

3. Using the symmetry of the terms inside the integral (Distortion components are symmetrical and Volterra kernels can be symmetrized [23]), the number of required kernels is significantly reduced.

Digitizing the dual band BBE Volterra model yields:

$$\widetilde{y}_{\omega_1}(n) = \widetilde{y}_{\omega_1,1}(n) + \widetilde{y}_{\omega_1,3}(n) + \widetilde{y}_{\omega_1,5}(n) + \cdots \tag{4.47}$$

$$\widetilde{y}_{\omega_1,1}(n) = \sum_{i_1=0}^{M_1} \widetilde{h}_{\omega_1,1} \cdot \widetilde{x}_1(n, i_1)$$

$$\widetilde{y}_{\omega_1,3}(n) = \sum_{i_1=0}^{M_{3,S}} \sum_{i_2=i_1}^{M_{3,S}} \sum_{i_3=i_2}^{M_{3,S}} \widetilde{h}_{\omega_1,3,s} \cdot \widetilde{x}_{3,s}(n, i_1, i_2, i_3)$$
$$+ \sum_{i_1=0}^{M_{3,S}} \sum_{i_2=0}^{M_{3,S}} \sum_{i_3=i_2}^{M_{3,S}} \widetilde{h}_{\omega_1,3,d} \cdot \widetilde{x}_{3,d}(n, i_1, i_2, i_3)$$

71

$$\widetilde{y}_{\omega_1,5}(n) = \sum_{i_1=0}^{M_{5,S}} \sum_{i_2=i_1}^{M_{5,S}} \sum_{i_3=i_2}^{M_{5,S}} \sum_{i_4=i_3}^{M_{5,S}} \sum_{i_5=i_4}^{M_{5,S}} \widetilde{h}_{\omega_1,5,s} \cdot \widetilde{x}_{5,s}\left(n, i_1, i_2, i_3, i_4, i_5\right)$$

$$+ \sum_{i_1=0}^{M_{5,d1}} \sum_{i_2=i_1}^{M_{5,d1}} \sum_{i_3=i_2}^{M_{5,d1}} \sum_{i_4=0}^{M_{5,d1}} \sum_{i_5=i_4}^{M_{5,d1}} \widetilde{h}_{\omega_1,5,d1} \cdot \widetilde{x}_{5,d1}\left(n, i_1, i_2, i_3, i_4, i_5\right)$$

$$+ \sum_{i_1=0}^{M_{5,d2}} \sum_{i_2=0}^{M_{5,d2}} \sum_{i_3=i_2}^{M_{5,d2}} \sum_{i_4=i_3}^{M_{5,d2}} \sum_{i_5=i_4}^{M_{5,d2}} \widetilde{h}_{\omega_1,5,d2} \cdot \widetilde{x}_{5,d2}\left(n, i_1, i_2, i_3, i_4, i_5\right)$$

where

$$\widetilde{x}_1\left(n, i_1\right) = \widetilde{x}\left(n - i_1\right)$$

$$
\begin{aligned}
\widetilde{x}_{3,s}\left(n, i_1, i_2, i_3\right) &= \widetilde{x}_1\left(n - i_1\right) \widetilde{x}_1\left(n - i_2\right) \widetilde{x}_1^*\left(n - i_3\right) \\
&+ \widetilde{x}_1\left(n - i_1\right) \widetilde{x}_1^*\left(n - i_2\right) \widetilde{x}_1\left(n - i_3\right) \\
&+ \widetilde{x}_1^*\left(n - i_1\right) \widetilde{x}_1\left(n - i_2\right) \widetilde{x}_1\left(n - i_3\right)
\end{aligned}
$$

$$
\begin{aligned}
\widetilde{x}_{3,d}\left(n, i_1, i_2, i_3\right) &= \widetilde{x}_1\left(n - i_1\right) \widetilde{x}_2\left(n - i_2\right) \widetilde{x}_2^*\left(n - i_3\right) \\
&+ \widetilde{x}_1\left(n - i_1\right) \widetilde{x}_2^*\left(n - i_2\right) \widetilde{x}_2\left(n - i_3\right)
\end{aligned}
$$

$$
\begin{aligned}
\widetilde{x}_{5,s}\left(n, i_1, i_2, i_3, i_4, i_5\right) &= \widetilde{x}_1\left(n - i_1\right) \widetilde{x}_1\left(n - i_2\right) \widetilde{x}_1\left(n - i_3\right) \widetilde{x}_1^*\left(n - i_4\right) \widetilde{x}_1^*\left(n - i_5\right) \\
&+ \widetilde{x}_1\left(n - i_1\right) \widetilde{x}_1\left(n - i_2\right) \widetilde{x}_1^*\left(n - i_3\right) \widetilde{x}_1\left(n - i_4\right) \widetilde{x}_1^*\left(n - i_5\right) \\
&+ \widetilde{x}_1\left(n - i_1\right) \widetilde{x}_1^*\left(n - i_2\right) \widetilde{x}_1\left(n - i_3\right) \widetilde{x}_1\left(n - i_4\right) \widetilde{x}_1^*\left(n - i_5\right) \\
&+ \widetilde{x}_1^*\left(n - i_1\right) \widetilde{x}_1\left(n - i_2\right) \widetilde{x}_1\left(n - i_3\right) \widetilde{x}_1\left(n - i_4\right) \widetilde{x}_1^*\left(n - i_5\right) \\
&+ \widetilde{x}_1\left(n - i_1\right) \widetilde{x}_1\left(n - i_2\right) \widetilde{x}_1^*\left(n - i_3\right) \widetilde{x}_1^*\left(n - i_4\right) \widetilde{x}_1\left(n - i_5\right) \\
&+ \widetilde{x}_1\left(n - i_1\right) \widetilde{x}_1^*\left(n - i_2\right) \widetilde{x}_1\left(n - i_3\right) \widetilde{x}_1^*\left(n - i_4\right) \widetilde{x}_1\left(n - i_5\right) \\
&+ \widetilde{x}_1^*\left(n - i_1\right) \widetilde{x}_1\left(n - i_2\right) \widetilde{x}_1\left(n - i_3\right) \widetilde{x}_1^*\left(n - i_4\right) \widetilde{x}_1\left(n - i_5\right) \\
&+ \widetilde{x}_1\left(n - i_1\right) \widetilde{x}_1^*\left(n - i_2\right) \widetilde{x}_1^*\left(n - i_3\right) \widetilde{x}_1\left(n - i_4\right) \widetilde{x}_1\left(n - i_5\right) \\
&+ \widetilde{x}_1^*\left(n - i_1\right) \widetilde{x}_1\left(n - i_2\right) \widetilde{x}_1^*\left(n - i_3\right) \widetilde{x}_1\left(n - i_4\right) \widetilde{x}_1\left(n - i_5\right) \\
&+ \widetilde{x}_1^*\left(n - i_1\right) \widetilde{x}_1^*\left(n - i_2\right) \widetilde{x}_1\left(n - i_3\right) \widetilde{x}_1\left(n - i_4\right) \widetilde{x}_1\left(n - i_5\right)
\end{aligned}
$$

$$\begin{aligned}
\widetilde{x}_{5,d1}\left(n,i_1,i_2,i_3,i_4,i_5\right) =\ & \widetilde{x}_1\left(n-i_1\right)\widetilde{x}_1\left(n-i_2\right)\widetilde{x}_1^*\left(n-i_3\right)\widetilde{x}_2\left(n-i_4\right)\widetilde{x}_2^*\left(n-i_5\right)\\
+\ & \widetilde{x}_1\left(n-i_1\right)\widetilde{x}_1^*\left(n-i_2\right)\widetilde{x}_1\left(n-i_3\right)\widetilde{x}_2\left(n-i_4\right)\widetilde{x}_2^*\left(n-i_5\right)\\
+\ & \widetilde{x}_1^*\left(n-i_1\right)\widetilde{x}_1\left(n-i_2\right)\widetilde{x}_1\left(n-i_3\right)\widetilde{x}_2\left(n-i_4\right)\widetilde{x}_2^*\left(n-i_5\right)\\
+\ & \widetilde{x}_1\left(n-i_1\right)\widetilde{x}_1\left(n-i_2\right)\widetilde{x}_1^*\left(n-i_3\right)\widetilde{x}_2^*\left(n-i_4\right)\widetilde{x}_2\left(n-i_5\right)\\
+\ & \widetilde{x}_1\left(n-i_1\right)\widetilde{x}_1^*\left(n-i_2\right)\widetilde{x}_1\left(n-i_3\right)\widetilde{x}_2^*\left(n-i_4\right)\widetilde{x}_2\left(n-i_5\right)\\
+\ & \widetilde{x}_1^*\left(n-i_1\right)\widetilde{x}_1\left(n-i_2\right)\widetilde{x}_1\left(n-i_3\right)\widetilde{x}_2^*\left(n-i_4\right)\widetilde{x}_2\left(n-i_5\right)
\end{aligned}$$

$$\begin{aligned}
\widetilde{x}_{5,d2}\left(n,i_1,i_2,i_3,i_4,i_5\right) =\ & \widetilde{x}_1\left(n-i_1\right)\widetilde{x}_2\left(n-i_2\right)\widetilde{x}_2\left(n-i_3\right)\widetilde{x}_2^*\left(n-i_4\right)\widetilde{x}_2^*\left(n-i_5\right)\\
+\ & \widetilde{x}_1\left(n-i_1\right)\widetilde{x}_2\left(n-i_2\right)\widetilde{x}_2^*\left(n-i_3\right)\widetilde{x}_2\left(n-i_4\right)\widetilde{x}_2^*\left(n-i_5\right)\\
+\ & \widetilde{x}_1^*\left(n-i_1\right)\widetilde{x}_2^*\left(n-i_2\right)\widetilde{x}_2\left(n-i_3\right)\widetilde{x}_2\left(n-i_4\right)\widetilde{x}_2^*\left(n-i_5\right)\\
+\ & \widetilde{x}_1\left(n-i_1\right)\widetilde{x}_2\left(n-i_2\right)\widetilde{x}_2^*\left(n-i_3\right)\widetilde{x}_2^*\left(n-i_4\right)\widetilde{x}_2\left(n-i_5\right)\\
+\ & \widetilde{x}_1\left(n-i_1\right)\widetilde{x}_2^*\left(n-i_2\right)\widetilde{x}_2\left(n-i_3\right)\widetilde{x}_2^*\left(n-i_4\right)\widetilde{x}_2\left(n-i_5\right)\\
+\ & \widetilde{x}_1\left(n-i_1\right)\widetilde{x}_2^*\left(n-i_2\right)\widetilde{x}_2^*\left(n-i_3\right)\widetilde{x}_2\left(n-i_4\right)\widetilde{x}_2\left(n-i_5\right)
\end{aligned}$$

In 4.47, M_1, $M_{3,s}$, $M_{3,d}$, $M_{5,s}$, $M_{5,d1}$ and $M_{5,d2}$ denote the memory depth of the first, third, fifth order Volterra series distortion terms. The dual-band complex valued BBE Volterra Series in 4.47 includes only nonlinear distortion products of up to order 5. Expression of the dual band BBE Volterra model with higher nonlinearity can be similarly derived. In addition, only odd powered terms are retained and even terms are discarded since they do not appear in the passband. It is worth mentioning that the distortion terms $\widetilde{x}_{3,s}(n,i_1,i_2,i_3)$ and $\widetilde{x}_{5,s}(n,i_1,i_2,i_3,i_4,i_5)$ are linear combinations of three third and ten fifth order distortion products, respectively. An example of the dual band BBE Volterra model of 4.47 is given for $NL=3$ and $M_1 = M_{3,s} = M_{3,d} = 1$ in 4.48.

$$\begin{aligned}
\widetilde{y}(n) =\ & \widetilde{h}_{\omega_1,1}(0)\widetilde{x}_1(n) + \widetilde{h}_{\omega_1,1}(1)\widetilde{x}_1(n-1)3\widetilde{h}_{\omega_1,3,s}(0,0,0)\widetilde{x}_1(n)\widetilde{x}_1(n)\widetilde{x}_1^*(n)\\
+\ & \widetilde{h}_{\omega_1,3,s}(0,0,1)\left(2\widetilde{x}_1(n)\widetilde{x}_1(n-1)\widetilde{x}_1^*(n) + \widetilde{x}_1(n)\widetilde{x}_1(n)\widetilde{x}_1^*(n-1)\right)\\
+\ & \widetilde{h}_{\omega_1,3,s}(0,1,1)\left(2\widetilde{x}_1(n)\widetilde{x}_1(n-1)\widetilde{x}_1^*(n-1) + \widetilde{x}_1(n-1)\widetilde{x}_1(n-1)\widetilde{x}_1^*(n)\right)\\
+\ & 3\widetilde{h}_{\omega_1,3,s}(1,1,1)\widetilde{x}_1(n-1)\widetilde{x}_1(n-1)\widetilde{x}_1^*(n-1)2\widetilde{h}_{\omega_1,3,d}(0,0,0)\widetilde{x}_1(n)\widetilde{x}_2(n)\widetilde{x}_2^*(n)\\
+\ & \widetilde{h}_{\omega_1,3,d}(0,0,1)\left(\widetilde{x}_1(n)\widetilde{x}_2(n)\widetilde{x}_2^*(n-1) + \widetilde{x}_1(n)\widetilde{x}_2^*(n)\widetilde{x}_2(n-1)\right)\\
+\ & 2\widetilde{h}_{\omega_1,3,d}(0,1,1)\widetilde{x}_1(n)\widetilde{x}_2(n-1)\widetilde{x}_2^*(n-1) + 2\widetilde{h}_{\omega_1,3,d}(1,0,0)\widetilde{x}_1(n-1)\widetilde{x}_2(n)\widetilde{x}_2^*(n)\\
+\ & \widetilde{h}_{\omega_1,3,d}(1,0,1)\left(\widetilde{x}_1(n-1)\widetilde{x}_2(n)\widetilde{x}_2^*(n-1) + \widetilde{x}_1(n-1)\widetilde{x}_2^*(n)\widetilde{x}_2(n-1)\right)
\end{aligned}$$

$$+ \quad 2\widetilde{h}_{\omega_1,3,d}(1,1,1)\widetilde{x}_1(n-1)\widetilde{x}_2(n-1)\widetilde{x}_2^*(n-1) \tag{4.48}$$

The close examination of 4.47 reveals a number of important attributes of the proposed dual band BBE Volterra model: Inclusion of all the possible distortion terms attributed to the static and dynamic nonlinear behavior of the PA. These later involve either only the envelope of the first band signal, e.g. $\widetilde{x}_1^*(n)\widetilde{x}_1^2(n)$, and $\widetilde{x}_1^*(n)\widetilde{x}_1(n)\widetilde{x}_1(n-1)$, or result from the mixing between the two bands' envelopes, e.g. $\widetilde{x}_1(n)\widetilde{x}_2^*(n)\widetilde{x}_2(n)$, and $\widetilde{x}_1(n)\widetilde{x}_2^*(n-1)\widetilde{x}_2(n)$. A large number of the distortion terms included in 4.47 were not incorporated in the 2D-DPD model[61] (i.e., $\widetilde{x}_2^*(n)\widetilde{x}_2(n)\widetilde{x}_1(n-1)$ and $\widetilde{x}_2^*(n-1)\widetilde{x}_2(n)\widetilde{x}_1(n-1)$).

While the proposed dual band BBE Volterra model includes larger number of distortion products than other models, according to 4.47 these products are grouped into different sets. Each set forms a distortion term, e. g. the distortion term $\widetilde{x}_{3,s}(n,i_1,i_2,i_3)$ represents the grouping of the following distortion products $\widetilde{x}_1(n-i_1)\widetilde{x}_1(n-i_2)\widetilde{x}_1^*(n-i_3)$, $\widetilde{x}_1(n-i_1)\widetilde{x}_1^*(n-i_2)\widetilde{x}_1(n-i_3)$, $\widetilde{x}_1^*(n-i_1)\widetilde{x}_1(n-i_2)\widetilde{x}_1(n-i_3)$. The distortion products that belong to a given set share the same kernel. For example, for every possible triplet $(i_1,i_2,i_3) \in \{0..M\}^3$, three 3rd order distortion products are combined to form $\widetilde{x}_{3,s}(n,i_1,i_2,i_3)$ and consequently share one kernel $\widetilde{h}_{\omega_1,3,s}(i_1,i_2,i_3)$ in 4.47. Similarly, for every possible quintuplet $(i_1,i_2,i_3,i_4,i_5) \in \{0..M\}^5$, ten 5th order distortion products are combined to form $\widetilde{x}_{5,s}(n,i_1,i_2,i_3,i_4,i_5)$ and share one kernel $\widetilde{h}_{\omega_1,5,s}(i_1,i_2,i_3,i_4,i_5)$ in 4.47. Hence, despite the fact that the proposed models involves more distortion terms, it requires comparable number of kernels compare to the 2D-DPD scheme.

4.2.2   Model Identification

The expression of the proposed of the dual band BBE Volterra model, 4.47, preserved the linearity propriety with respect to its coefficients. Hence, the least square error (LSE) estimator can be applied to identify the kernels in 4.47 for a given RF PA. Equation 4.49 details the expression used to compute the LSE solution of 4.47:

$$X \cdot h = Y \tag{4.49}$$

where A denotes the distortion products matrix, h is the kernels' vector to be estimated and Y is the vector formed by the output signal sample. Each of these variables (A,h and Y) is defined in 4.50 where L representing the data stream size.

$$X \;=\; \begin{pmatrix} \widetilde{x}_{1,s}(M_1+1) & \cdots & \widetilde{x}_{1,s}(1) & \widetilde{x}_{3,s}(M_{3,s}+1,0,0,0) \\ \vdots & \ddots & \vdots & \vdots \\ \widetilde{x}_{1,s}(L) & \cdots & \widetilde{x}_{1,s}(L-M_1) & \widetilde{x}_{3,s}(L,0,0,0) \end{pmatrix}$$

$$\left. \begin{array}{cccc} \cdots & \widetilde{x}_{3,s}(1, M_{3,s}, M_{3,s}, M_{3,s}) & \widetilde{x}_{3,d}(M_{3,d}+1, 0, 0, 0) & \cdots \\ \ddots & \vdots & \vdots & \vdots \\ \cdots & \widetilde{x}_{3,s}(L - M_{3,s}, M_{3,s}, M_{3,s}, M_{3,s}) & \widetilde{x}_{3,d}(L, 0, 0, 0) & \cdots \end{array} \right)$$

$$h = \begin{pmatrix} h_0 \\ \vdots \\ h_{M_1} \\ h_{0,0,0} \\ \vdots \end{pmatrix} \ ; \ Y = \begin{pmatrix} \widetilde{y}_{1,0}(M_1+1) \\ \vdots \\ \widetilde{y}(L) \end{pmatrix}, \tag{4.50}$$

The LSE solution to 4.49 is computed using:

$$\hat{h} = \left(X^t \cdot X \right)^{-1} \cdot X^t \cdot Y \tag{4.51}$$

where $\hat{h}$ is the estimate of h.

4.2.3 Validation

To assess the performance of the proposed model, the novel formulation was used to model and linearize a high power dual-band RF PA. The device under test was a broadband 45 W single ended GaN PA [71] driven with a dual-band multi-standard signal. Three test scenarios are defined:

- Case 1: 15 MHz WCDMA and 10 MHz LTE signals centered @ 2.1 GHz and 2.4 GHz respectively

- Case 2: 20 MHz 4C WCDMA and 20 MHz LTE signals centered @ 2.1 GHz and 2.4 GHz, respectively

- Case 3: 20 MHz LTE and 20 MHz WCDMA signals centered @ 2.4 GHz and 2.1 GHz respectively

Fig. 4.9 shows the mixed signal linearization test bench used. It consisted of two vector signal generators (ESG4438C), a vector signal analyzer (N9030A) for output signal capture, and a host computer for test signal synthesis and upload, delay estimation/alignment, output signal download and model identification.
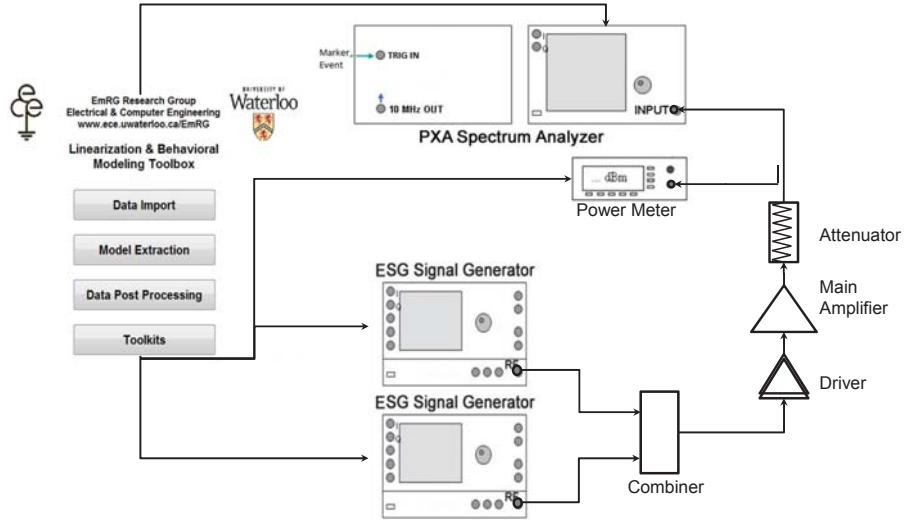
Figure 4.9: Dual-band DPD measurement setup

Both the proposed the dual band BBE Volterra model and the 2D DPD models are implemented and used to linearize the DUT. The nonlinearity order and memory depth of each model were individually set to achieve the best performance vs. complexity compromise in each case. For the two first scenarios, it was found that $NL = 7$ and $M = 3$ for the 2D DPD and $NL = 7$, $M_1 = 2$, $M_{3,s} = M_{3,d} = 1$, $M_{5,s} = M_{5,d1} = M_{5,d2} = 0$ and $M_7 = 0$ for the dual band BBE Volterra are suitable. However, for the third case, $NL = 7$ and $M = 3$ for the 2D DPD and $NL = 9$, $M_1 = 2$, $M_{3,s} = M_{3,d} = 1$, $M_{5,s} = M_{5,d1} = M_{5,d2} = 0$, $M_7 = 0$, $M_9 = 0$ for the dual band BBE Volterra were found adequate.

The linearization results for the three tests scenarios are shown in Fig. 4.10-4.12 and the corresponding performances are summarized in Table $4.4 - 4.6$. According to the linearization results obtained in all of the test scenarios, the dual band BBE Volterra model succeeded to linearize the PA and significantly outperformed the 2D DPD in terms of linearization capacity and model complexity. A reduction of the spectrum regrowth of about 20dB and an ACPR of about 50dBc were achieved by the dual band BBE Volterra in all test scenarios. However, the 2D-DPD linearization capacity was different in the three scenarios and in some cases very limited improvement on the spectrum regrowth was obtained.

Table 4.4: Dual-band dual-standard linearization results case 1

	Without DPD		With Volterra DPD		With 2D DPD	
	Band 1 @ 2.1GHz	Band 2 @ 2.4GHz	Band 1 @ 2.1GHz	Band 2 @ 2.4GHz	Band 1 @ 2.1GHz	Band 2 @ 2.4GHz
Number of coefficients			20	20	45	45
NMSE (dB)			-41	-40	-31	-28
ACLR (dBc)	35	29	-53	-51	-40	-37

Table 4.5: Dual-band dual-standard linearization results case 2

	Without DPD		With Volterra DPD		With 2D DPD	
	Band 1 @ 2.1GHz	Band 2 @ 2.4GHz	Band 1 @ 2.1GHz	Band 2 @ 2.4GHz	Band 1 @ 2.1GHz	Band 2 @ 2.4GHz
Number of coefficients			20	20	45	45
NMSE (dB)			-39	-39	-31	-28
ACLR (dBc)	-34	-28	-50	-50	-39	-34

Table 4.6: Dual-band dual-standard linearization results case 3

	Without DPD		With Volterra DPD		With 2D DPD	
	Band 1 @ 2.1GHz	Band 2 @ 2.4GHz	Band 1 @ 2.1GHz	Band 2 @ 2.4GHz	Band 1 @ 2.1GHz	Band 2 @ 2.4GHz
Number of coefficients			25	25	84	84
NMSE (dB)			-38	-33	-29	-32
ACLR (dBc)	-31	-37	-50	-51	-34	-39

(a)

(b)
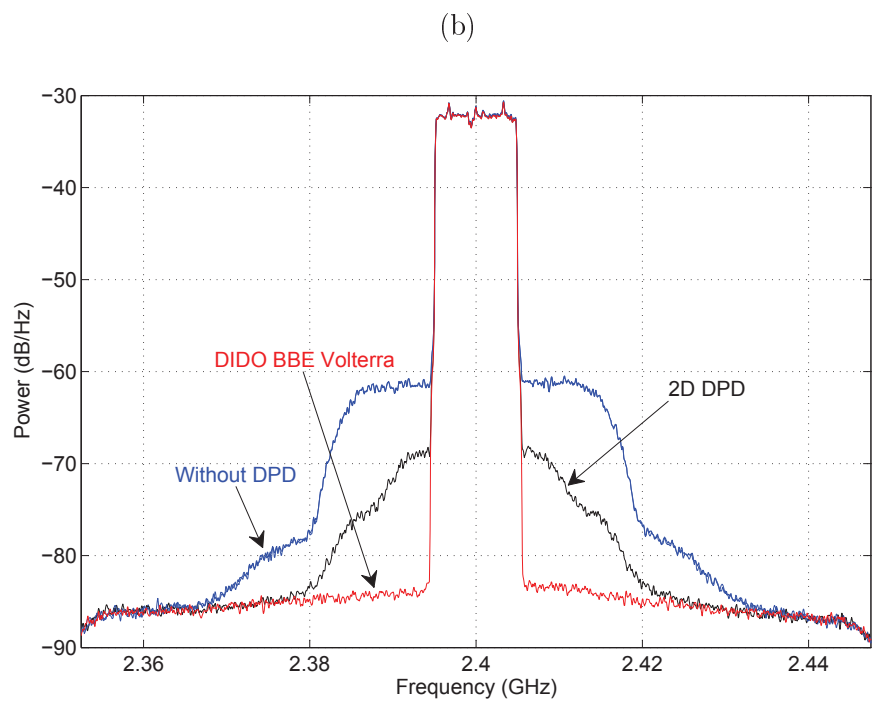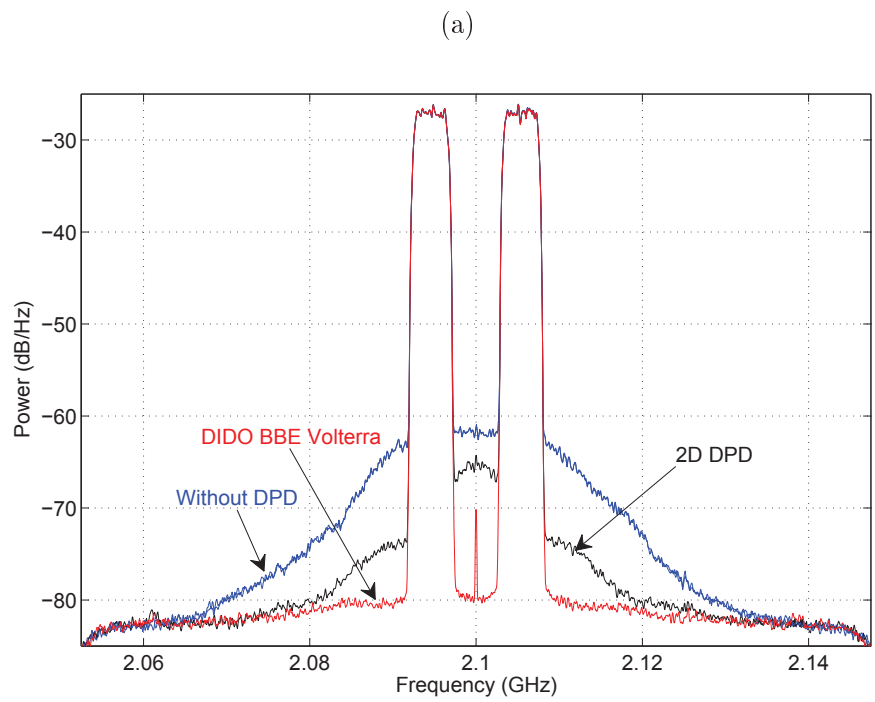
Figure 4.10: Dual-band predistortion results for case 1
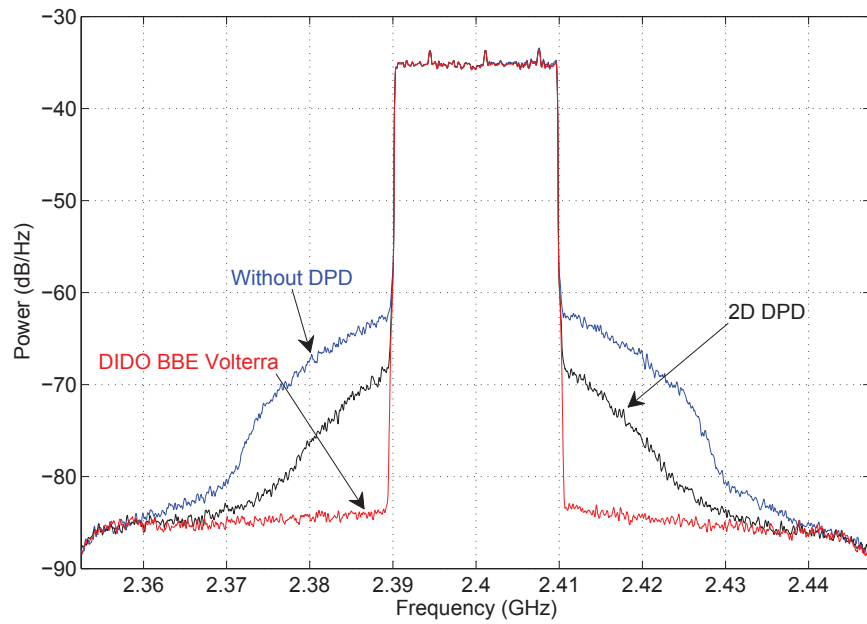
78

(a)
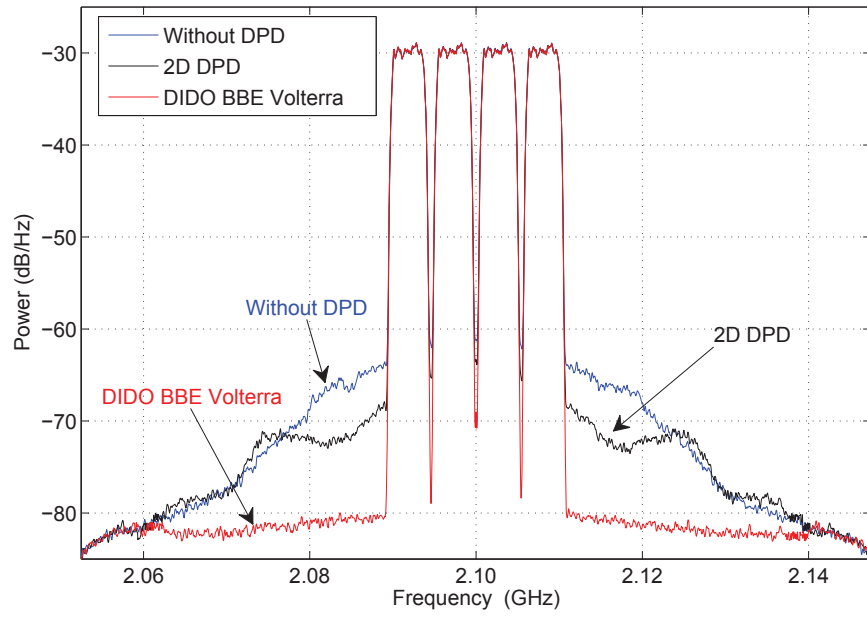
(b)

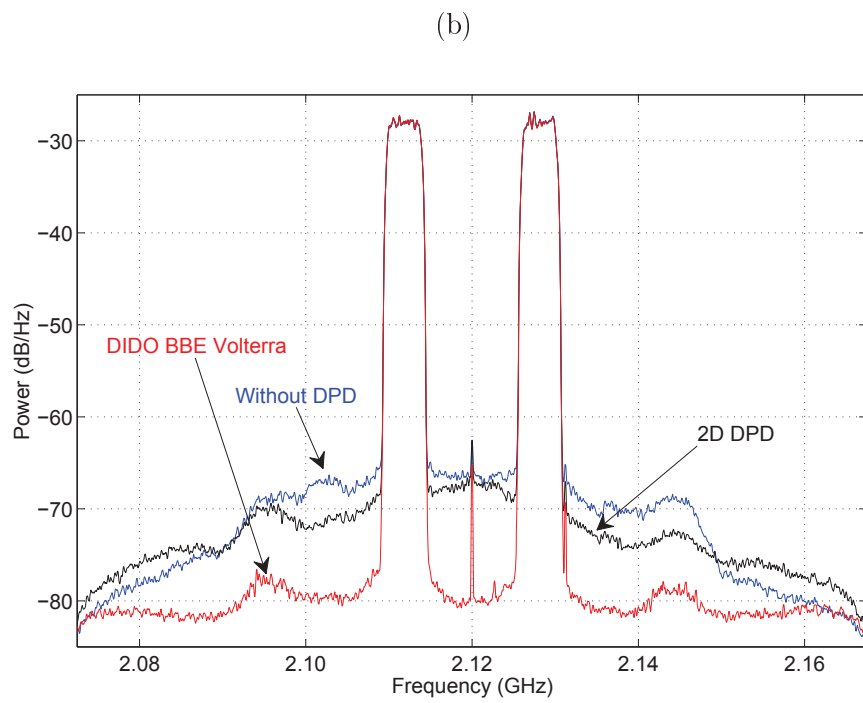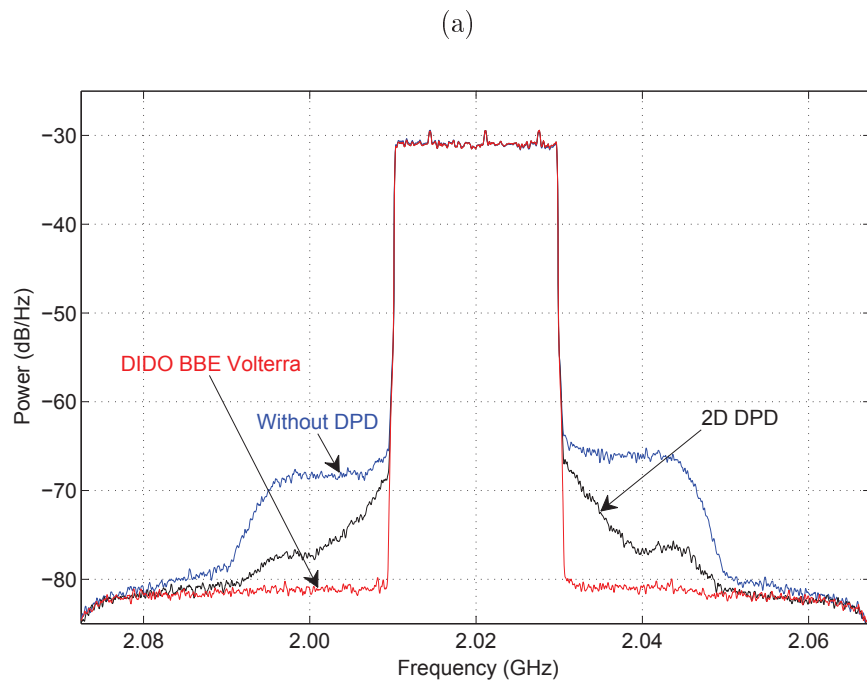Figure 4.11: Dual-band predistortion results for case 2

79

Figure 4.12: Dual-band predistortion results for case 3

Chapter 5

Automated Symbolic Optimization and High Level Synthesis of Single- and Multi- Band Digital Predistortion Hardware in an FPGA

The choice of digital predistortion (DPD) scheme for the real-time linearization of radio frequency (RF) power amplifiers (PA) is typically motivated by the hardware implementation complexity versus linearization capacity tradeoff. DPD schemes employing block-based representation, which consists of adequately arranging a number of simple modules (e.g., static nonlinear functions, finite impulse response filters), are generally adopted where possible to alleviate the computational and implementation complexity of some models (e.g., memory polynomial (MP) [17], Weiner/Hammerstein). Such block-based representation is geared towards complex-signal processing arithmetic rather than real-signal formulations and suffers from limited linearization capacity when deployed with advanced PA systems exhibiting significant distortions. This motivated the recent development of more sophisticated Volterra series based schemes, such as the complexity reduced Volterra (CRV) [76], baseband equivalent (BBE) Volterra [77] and dynamic deviation reduction (DDR) Volterra [18] schemes which don't have a simple block-based representation.

The trivial criteria to choosing a DPD scheme has typically been the number of coefficient involved. Accordingly, it has been widely accepted that a model with fewer coefficients is usually easier to implement. This assumption motivated, in part, the adoption of a number of Volterra series approximations where the cross terms were either completely discarded (e.g., MP) or partially pruned (e.g., generalized MP or GMP, DDR and CRV models). Yet in-depth analysis and extensive experimental investigation revealed the need to increase the nonlinearity order of the static nonlinear part of the model as the cross

terms are pruned to preserve the same linearization capacity. Hence, the apparent simplicity of the MP approach compared to the Volterra series may not translate into easier hardware implementation as it may actually require higher order nonlinear terms which call for higher resolution (number of bits) and more logic gate counts. Therefore, in this work, a non-pruned single- and dual-band BBE Volterra series [84, 77] DPD scheme was selected.

This chapter presents an automated optimization approach for single- and dual-band Volterra DPD hardware implementation in a field-programmable gate array (FPGA). This approach first employs a symbolic arithmetic tool to transform the DPD expression in order to minimize the arithmetic complexity, then uses a HLS tool to automate the hardware synthesis. The proposed approach is DPD model agnostic and can be applied to any variation of the reported Volterra series-based DPD schemes.

5.1 Review of Optimization Approaches

Three approaches are generally pursued to optimize DPD hardware implementation.

The first consists of substituting the nonlinear basis functions (or a subset of the equations) with Look-up Tables (LUT) in order to save on the number of multipliers and logic gates for a specific accuracy. The LUT size and the entries' length are determined based on the type of nonlinear function and the required signals' dynamic range [79, 78]. The LUT based implementation complexity increases significantly when dealing with significant memory effects and/or with multi-band DPD schemes (requiring multi-dimensional LUT). For example, Ding et al. [66] and Roblin et al. [80] employed two-dimensional LUT-based/spline-based representations of a 2D-DPD scheme [61] to simplify its implementation.

The second hardware implementation optimization approach relies on Time Domain Multiplexing (TDM) by sharing the same hardware resource across different signal processing blocks. TDM has been used to implement single-band [81] and dual-band DPD schemes [68]. Nonetheless, the resulting TDM based DPD engine must run at a higher speed to achieve the same latency and consequently trades circuit area for an increase in power consumption.

The third approach addresses the hardware implementation burden of DPD by reformulating its expression. This includes the application of Horner's rule to memoryless polynomials initially, then eventually to MP DPD schemes [82]. Alternatively, authors in [83] have suggested a reformulation of the polynomial DPD using a zero crossing approach to determine its polynomial roots. Unfortunately, none of these expression reformulation approaches are suited to Volterra series-based DPD schemes.

5.2 Arithmetic Optimization

In this section, a number of arithmetic optimization techniques are presented. These are used afterward for the symbolic optimization of section 5.3.

5.2.1 Complex Valued to Scalar Valued Conversion

The first step of optimization consists in transforming the complex-valued model into a scalar-valued one to facilitate the arithmetic implementation. The following example is provided to illustrate this concept.

$$E = x(n) \cdot x^*(n) = \left(I^2(n) + Q^2(n) \right) \tag{5.1}$$

where $x(n) = I(n) + j \cdot Q(n)$ and $*$ denotes the conjugate operator. Hence, instead of computing $x \cdot x^*$ using a complex multiplier, which would require 4 real multiplications and 2 real additions, one can obtain the same result using 2 real multiplications and 1 real addition. The real-valued expression is more suitable to the application of algebraic transformations which simplifies its hardware implementation.

5.2.2 Factorization

Subsequently, the resulting real-valued BBE Volterra series expression is transformed through factorization to reduce the number of arithmetic multiplications. The following example is provided to illustrate the benefit of this operation:

$$E = I^2(n) + I(n) \cdot I(n-1) = I(n) \cdot (I(n) + I(n-1)) \tag{5.2}$$

Equation 5.1 uses 2 multiplications and 1 addition, while 5.2 uses 1 multiplication and 1 addition.

5.2.3 Cascading

The factorized DPD expression undergoes cascading which consists of generating lower nonlinearity order monomials and reusing them to produce higher order nonlinearity terms. The following example is used for illustration purposes:

$$E = Q^2(n) + I^5(n) + I^3(n) \cdot Q^2(n) \tag{5.3}$$

83

Equation 5.3 requires 9 real multiplications and 2 additions. After factorization, this expression is rewritten as

$$E = Q^2(n) + I^3(n) \cdot (I^2(n) + Q^2(n)) \tag{5.4}$$

High Level Synthesiswhere 5.4 necessitates 5 multiplications and 2 additions. After cascading 5.4 is rewritten as 5.5, and only 4 multiplications and 2 additions will be used

$$E = t_3 + t_2 \cdot (t_1 + t_3) \tag{5.5}$$

with $t_1 = I^2(n)$; $t_2 = t_1 \cdot I(n)$; $t_3 = Q(n)$, where t_1, t_2 and t_3 represent the intermediate terms.

5.2.4 Streamlining

Streamlining consists of time shifting some nonlinear terms in order to generate nonlinear memory terms rather than re-computing them. When applied to the Volterra series, streamlining allows for the rearrangement of the series monomials in an efficient V-vector format [85]. The following example is used to illustrate this point:

$$E = I(n) \cdot I(n-1) + I(n-1) \cdot I(n-2) \tag{5.6}$$

Equation 5.6 uses 2 multiplications and 1 addition; after streamlining only 1 multiplication and 1 addition are needed.

$$S(n) = I(n) \cdot I(n-1); \ E = S(n) + S(n-1)$$

The reduction in the number of operations described in the previous sub-sections is significant when applied to Volterra series DPD, as will be shown in section 5.4.

5.3 Proposed Optimization and Implementation Flow

A systematic procedure for optimizing the implementation of Volterra series-based DPD schemes is proposed, as depicted in Fig. 5.1. First, the various arithmetic transformations, presented in section 5.2, are applied to the original DPD expression. These transformations are automatically performed using the symbolic math tool, Maple™ from Maplesoft. Then, an HLS tool, the HDL coder™ from Matlab®, is used to automatically generate the digital hardware code with the minimum number of multipliers, adders and memory size needed to
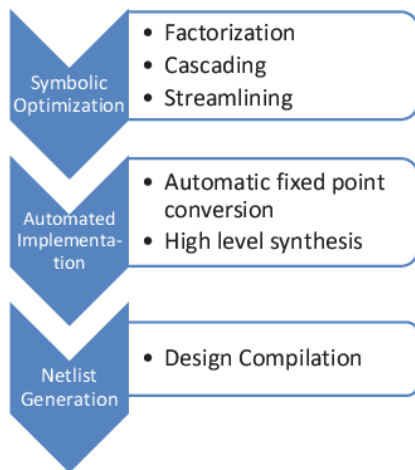
Figure 5.1: Proposed optimization and implementation flow

implement the model expression resulting from the previous step. Finally, the synthesized design is compiled.

It is of note that the optimization procedure is model independent and can be applied to any Volterra model.

Once the DPD expression undergoes the previously-mentioned transformations, the model is converted into a fixed point form then synthesized into HDL code using the HLS tool. The optimization steps enable successive multiplication and addition operations, avoiding the direct computation of high order terms (e.g., $I^5(n)$ is no longer explicitly computed), an approach characterized by more accurate and efficient fixed-point implementation. Simulation trials can then be conducted using a number of different signal stimuli and PAs under test to determine the optimal numerical representations (number of bits) for each of the intermediate terms (see Sub-section 5.2.3). The latter terms are optimized to fit, whenever possible, in one unique configuration of the digital signal processor (DSP) multiplier blocks (e.g., 18x18). One last optimization is then applied to the constant multiplications resulting from the model optimization (e.g., $I \cdot Q + Q \cdot I = 2 \cdot I \cdot Q$) or from the model preconditioning. Instead of using hardware multipliers, constant multiplications are implemented using minimal shift and adder operations.

5.4 Application to BBE Volterra Model

The proposed hardware optimization procedure was used to implement single- and dual-band BBE Volterra models [84, 77] in an FPGA and linearize a 45 W single-ended GaN

Table 5.1: Hardware implementation complexity of BBE Volterra

Optimization step	Tool	Number of multipliers/adders	
		Single-band	Dual-band
Original complexity		70 / 64 *	296 / 240 *
Complex to real conversion	Maple	280 / 268	1184 / 1072
Factorization		218 / 74	708 / 242
Cascading		100 / 65	234 / 158
Streamlining		95 / 65	224 / 158
Fixed-point conversion	Matlab	95 / 65	224 / 158
Constant multiplier optimization		71 / 89	170 / 197
RTL synthesis	Quartus	72 / 89	178 / 197

* Number of complex operations

Table 5.2: BBE Volterra series hardware resources

Model	4-input LUT	Register	Memory	DSP block
Single-band BBE Volterra	1680	1265	0	72
Dual-band BBE Volterra	2580	6185	0	178

PA. The experimental validation was conducted using the Altera Stratix IV professional development and the MS-DPD board from Analog Devices. The PA was driven by a 20 MHz LTE signal for the single-band case and an inter-band carrier aggregated signal formed by a 15 MHz WCDMA signal and 15 MHz LTE signal for the dual-band case (see Figs. 5.2 and 5.3). The models' hardware complexity at each stage of the proposed implementation flow is presented in table 5.1; the required hardware resources are reported in table 5.2. For the single-band case, it can be seen that the overall complexity decreased from 280/268 multipliers/adders to 72/89 multipliers/adders, whereas for the dual-band case, the overall complexity decreased from 1184/1072 multipliers/adders to 178/197 multipliers/adders. Note that the final number of DSP blocks would be manageable for mid-range FPGA families, and that no memory blocks were used in these experiments as the LUT approach was not used. The DPD hardware ran at the speed of signal's sampling rate (i.e., 122 Msps), as the time division multiplexing method was avoided.
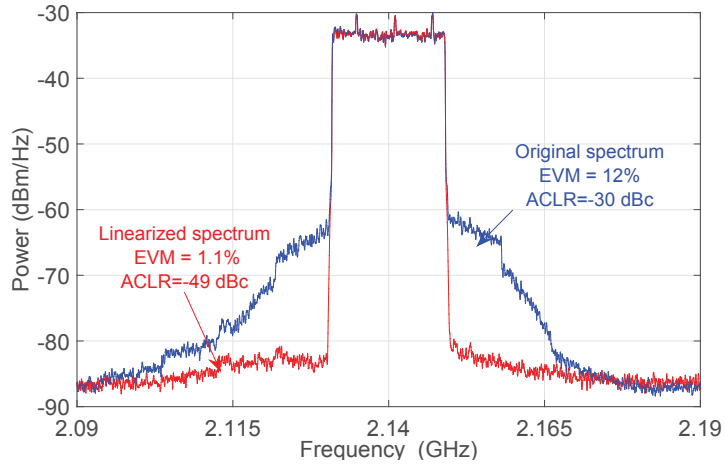
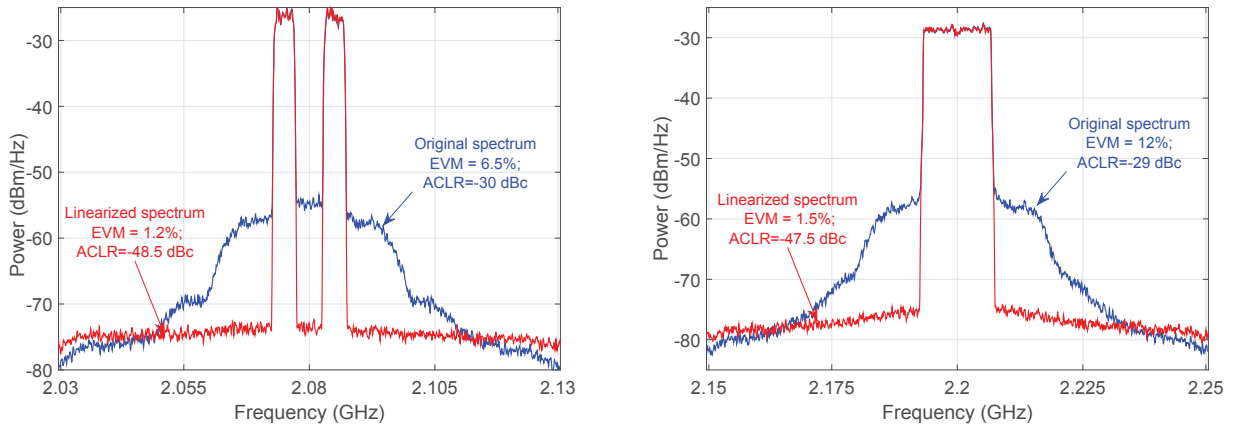Figure 5.2: Linearization results for single-band case

Figure 5.3: Linearization results for single-ended PA driven by (left) 101 WCDMA signal @ 2.08 GHz and (right) 15 MHz LTE signal @ 2.2 GHz

Chapter 6

Dual-band Digital Predistortion Using a Single Transmitter Observation Receiver and Single Training Engine

The carrier aggregation concept was recently adopted by wireless communication standardization bodies to meet the need for wider band communication signals and better spectrum resource utilization. Accordingly, wireless communication signals can now be composed of up to five component carriers (CC), each of which occupies up to 20 MHz. This may compromise the practical viability of wideband and multi-band DPD schemes. An intra-band CA signal with an aggregated bandwidth as high as 100 MHz, will yield a PA output spectrum that occupies up to 500 MHz, necessitating a very power hungry and expensive broadband transmitter observation receiver (TOR) to synthesize the DPD function. Researchers in [88] attempted to reduce the TOR bandwidth required by adopting a band limited DPD Volterra scheme. Alternatively, authors in [89] adopted an iterative approach for training the DPD function using a TOR with reduced bandwidth.

DPD in the case of inter-band carrier aggregation is even more complicated; as the number of CCs increases, it is not practical to dedicate one TOR per CC for real-time training of the multi-band DPD due to the power overhead. The usage of a single TOR, which captures the different CCs in alternation, is feasible in a controlled laboratory environment (fixed room temperature and average output power), as the distortions exhibited by the PA remain unchanged as long as the same input signal is applied. In this case, the input signal is repeated N times, where N is the number of CCs, and the single TOR is switched N times to capture all of the CC envelopes. However, in a real world environment, communication signals are not repeatable and consequently such an approach is impractical.

To tackle this issue, authors in [65] proposed a subsampling receiver to train a dual-band

2D-DPD. The subsampling receiver translated the two CCs to intermediate frequencies with a smallest frequency separation. The new frequencies were then digitized using an analog to digital converter (ADC). Although this approach needed only one TOR, and suppressed the large frequency separation in a realistic transmission scenario, it required an ADC with a sampling rate equal to 5N times the bandwidth of the CC (N is the number of CCs and a factor of 5 is needed due to the PA output spectrum regrowth). Alternatively, authors in [91] recently proposed a DPD system where the feedback receiver uses a single TOR that switches between the different CCs. While this approach effectively reduces the required number of TORs without increasing the required ADC sampling rate, it results in significant power consumption due to the additional step needed for the DPD training. This will be explained in the next section.

This chapter tackles the challenging hardware complexity of a dual-band DPD used to linearize PAs driven with realistic (non-periodic) inter-band CA signals. A novel DPD system employing one TOR is proposed which includes a single model-reference adaptive control (MRAC) based training engine (TE) to identify the coefficients of the two DPD functions needed to linearize the PA response (one function for each of the CCs).

6.1   Single Transmitter Observation Receiver System

While the previously mentioned works [65, 91, 90] succeeded in reducing the number of TORs needed to capture the individual CC envelopes at the output of a PA driven with inter-band CA signals, they suffered either from an increased ADC sampling rate [65], or signal processing overhead for training the DPD [91, 90]. For instance, the training of the DPD in [91] is preceded by the construction of a behavioral PA model based on its output signal's CC envelopes, successively captured while the PA is driven with real CA signals. This step is essential as the resulting PA behavioral model is used to generate a new set of input and output signal samples for training the multi-band DPD. A similar approach was suggested in [90] where the dual-band PA behavior was first modeled then its 2D-Quasi inverse deduced. Hence, both solutions [91, 90] pose additional signal processing burdens and require longer training phases.

Furthermore, all three works [65, 91, 90] utilized the self-tuning regulator (STR) approach, commonly called the indirect learning approach, to train the multi-band DPD. This approach relies on reversing the input and output signals of the PA to identify the inverse functions. This training approach has been applied widely and successfully in single-band DPD [92] due to its simplicity and effectiveness. However, when applied to training a dual-band DPD, this approach requires simultaneous access to both CCs of the PA output signal and one CC of its input signal in order to estimate the DPD for a given band. Therefore, if one were to reduce the number of TORs through switching or time
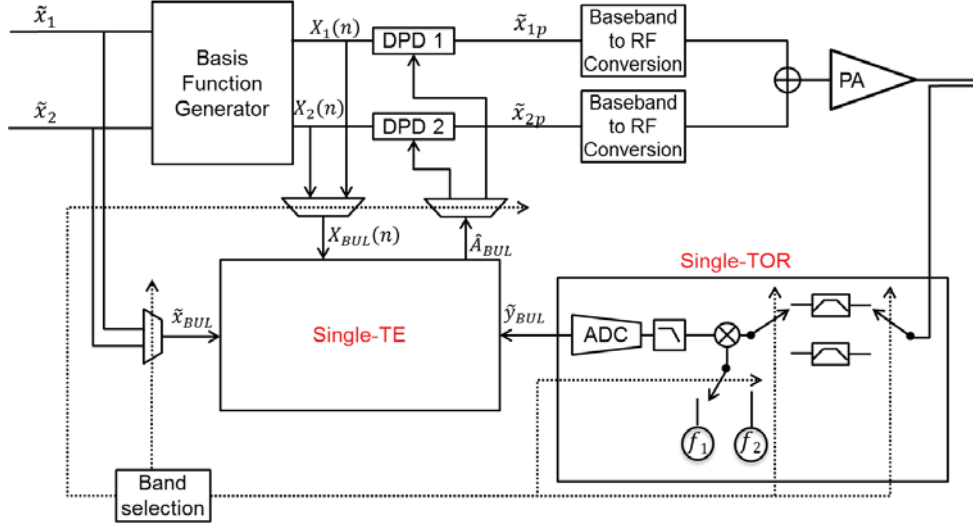
89

Figure 6.1: Single-transmitter observation receiver with single-training-engine dual-band linearizer

sharing a single TOR, the output signals would be captured at different time slots from the input signals thus not meeting the requirement for simultaneous CC access.

In this work, a single TOR based dual-band DPD is devised which does not require PA behavioral modeling [91, 90] or an increase to the ADC sampling rate [65]. The control algorithm is performed using an MRAC approach where the controller (the DPD function), is located inside of the feedback loop [92]. This is in opposition to the STR approach, which is an open loop system where the controller is located outside of the feedback loop. The MRAC approach has been applied previously in the context of single-band linearization [78, 79]. Also known as a direct learning, the MRAC based learning approach eliminates the requirement for simultaneous capture of the PA CCs' output signals.

Fig. 6.1 presents the proposed single TOR based DPD system. The single TOR module monitors and captures one CC output envelope signal at a time. A single TE module is used to iteratively train the DPD module corresponding to the captured CC. The training of the DPD modules corresponding to each of the CCs is performed using the same TE, while the single TOR is switched to cover all the bands. In Fig. 6.1, the two input CCs are noted $\tilde{x}_1$ and $\tilde{x}_2$ and their predistorted counterparts are denoted $\tilde{x}_{1p}$ and $\tilde{x}_{2p}$. $\tilde{x}_{BUL}$ designates the envelope of the input signal CC corresponding to the band under linearization (BUL). The BUL is determined by the band-selection module (see Fig. 6.1) to undergo predistortion training in the current iteration (i.e would be either $\tilde{x}_1$ or $\tilde{x}_2$ depending on the iteration). $\tilde{y}_{BUL}$ is the envelope of the output signal's CC corresponding to the BUL. The TE module iteratively adjusts the DPD coefficients until the distortions, d_{BUL}, introduced in the output signal CC's envelope, $\tilde{y}_{BUL}$, are fully cancelled.

90

$$d_{BUL}(n) = \widetilde{y}_{BUL}(n) - \widetilde{x}_{BUL}(n) \tag{6.1}$$

In Fig. 6.1, the two DPD modules work together to execute a dual-band predistortion function that pre-processes the two input CC envelopes according to the following equations

$$\widetilde{x}_{1p} = \sum_i^{N_1} \sum_j^{J_1} \sum_m^{M_1} \sum_v^{V_1} \hat{a}^1_{i,j,m,v} \varphi^1_{i,j,m,v} (\widetilde{x}_1(n), \widetilde{x}_2(n)) \tag{6.2}$$

$$\widetilde{x}_{2p} = \sum_i^{N_2} \sum_j^{J_2} \sum_m^{M_2} \sum_v^{V_2} \hat{a}^2_{i,j,m,v} \varphi^2_{i,j,m,v} (\widetilde{x}_1(n), \widetilde{x}_2(n)) \tag{6.3}$$

where $\varphi^1_{i,j,m,v}$ and $\varphi^2_{i,j,m,v}$ represent the basis functions of the DPD modules corresponding to each band and N_1 and J_1 (resp. N_2 and J_2) represent the nonlinearity orders of the inter-band and cross-band distortion in the first (resp. second) band DPD module. M_1 and V_1 (resp. M_2 and V_2) represent the memory depths of the inter-band and cross-band distortion in the first (resp. second) band DPD, and $\hat{a}^1_{i,j,m,v}$ and $\hat{a}^2_{i,j,m,v}$ denote the two DPD models' coefficients. Equations 6.2 and 6.3 can be rewritten in vector form as follows:

$$\widetilde{x}_{1p} = \hat{A}^1 \cdot X_1(n) \tag{6.4}$$
$$\widetilde{x}_{2p} = \hat{A}^2 \cdot X_2(n) \tag{6.5}$$

where $\hat{A}^1$ (resp. $\hat{A}^2$) is a vector comprising all the coefficients $\hat{a}^1_{i,j,m,v}$ (resp. $\hat{a}^2_{i,j,m,v}$) of the first band DPD (resp. the second band DPD). $X_1(n)$ (resp. $X_2(n)$) is a vector comprising all basis functions $\varphi^1_{i,j,m,v}$ (resp. $\varphi^2_{i,j,m,v}$) . The vectors $X_1(n)$ and $X_2(n)$ are computed in basis function generator module shown in Fig. 6.1.

It is to note that the proposed approach enables the reuse of the pre-computed basis functions vectors $X_1(n)$ and $X_2(n)$ in the two DPD engines and training branches. In Fig. 6.1, $X_{BUL}(n)$ is the basis functions vector for the band under linearization and can be equal to either $X_1(n)$ or $X_2(n)$ depending on the setting of the band selection module.

Different dual-band DPD schemes [61, 93, 84, 87] have used various forms of basis functions $\varphi^1_{i,j,m,v}$ and $\varphi^2_{i,j,m,v}$. In this work, for the purposes of illustration, the dual-band baseband equivalent (BBE) Volterra model defined in [84] is used. However, the proposed system in Fig. 6.1 can be applied to any of the dual-band DPD schemes reported in the literature.

Next section provides details of the dual-band recursive least squares (RLS) algorithm which was applied to identify the dual-band DPD coefficients using a single TOR path.

6.2   RLS Based MRAC Learning Approach

An RLS estimation algorithm was chosen to recursively adjust the DPD coefficients using (6) until cost function, J, [92] is minimized.

$$J = min \left(\sum_n \left| d_{BUL}(n) - \Delta \hat{A}_{BUL} \cdot X_{BUL}(n)^t \right|^2 \right) \qquad (6.6)$$

In 6.6, $d_{BUL}(n)$ is the linearization error defined in 6.1, $\hat{A}_{BUL}$ and $X(n)$ are two vectors comprised of the DPD modules' coefficients and basis functions, respectively. $\Delta \hat{A}_{BUL}$ denotes the DPD coefficients estimation error.

As the band selection module switches between the different bands, the corresponding blocks of data, which are formed by the input CC $\widetilde{x}_{BUL}(n)$, the basis functions $X_{BUL}(n)$ and the output CC $\widetilde{y}_{BUL}(n)$, are used to estimate the corresponding DPD coefficients. In each iteration, the estimated DPD coefficients error $\Delta \hat{A}_{BUL}$ is exploited to compute the new estimate of the DPD coefficients $\hat{A}_{BUL}$ using a forgetting factor γ according to 6.7.

$$\hat{A}_{BUL}(q+1) = \hat{A}_{BUL}(q) - \gamma \cdot \Delta \hat{A}_{BUL} \qquad (6.7)$$

The details of the developed dual-band RLS algorithm are presented in Algorithm I. The vector $W(n)$ represents the estimated error in the DPD's coefficients vector and matrix P is referred to as the inverse correlation matrix. The coefficients vector and the inverse correlation matrix are initially set to be equal to $W(0) = [1, 0, \ldots, 0]$ and $P(0) = \Delta \cdot I$, where I is the identity matrix and $\Delta = 1e5$. The gain vector $G(n)$ is computed for each time instance as

$$G(n) = \frac{P(n) \cdot X_{BUL}(n)^t}{1 + X_{BUL}(n) \cdot P(n) \cdot X_{BUL}(n)^t}$$

This gain vector is multiplied by the a priori estimation error $d(n) - X_{BUL}(n) \cdot W(n)$ and added to the coefficients vector to update the coefficients.

$$W(n+1) = W(n) + G(n) \cdot (d(n) - X_{BUL}(n) \cdot W(n))$$

Once the coefficients have been updated, the inverse correlation matrix is updated, and the estimation resumes with the new input CCs samples.

$$P(n+1) = (I - G(n) \cdot X_{BUL}(n)) \cdot P(n)$$

$$\Delta = 1e5$$

$$W(0) = \left\{ \begin{array}{l} [1, 0, ..., 0] \ if \ q = 0 \\ \hat{A}_{BUL}(q-1) \ if \ q \neq 0 \end{array} \right\}$$

$$P(0) = \Delta \cdot I$$

$for \ n = 1 : Q$

$$G(n) = \frac{P(n) \cdot X_{BUL}(n)^t}{1 + X_{BUL}(n) \cdot P(n) \cdot X_{BUL}(n)^t}$$

$$P(n+1) = (I - G(n) \cdot X_{BUL}(n)) \cdot P(n)$$

$$d(n) = \widetilde{y}_{BUL}(n) - \widetilde{x}_{BUL}(n)$$

$$W(n+1) = W(n) + G(n) \cdot (d(n) - X_{BUL}(n) \cdot W(n))$$

end

$$\Delta \hat{A}_{BUL} = W(Q+1)$$

$$\hat{A}_{BUL}(q+1) = \hat{A}_{BUL}(q) - \gamma \cdot \Delta \hat{A}_{BUL}$$

Algorithm I: RLS algorithm applied to MRAC learning approach

6.3   Experimental Validation

The performance assessment of the proposed approach was conducted here by applying it to linearize a PA under test fed with dual band signal. The measurement setup includes two vector signal generators (ESG3348C from Agilent Technologies) and Vector signal analyzer (PXA 9030A from Agilent Technologies) and a host computer that runs the RLS estimation algorithms and emulates the dual DPD engine. The device under test (DUT) was a 20W class F Doherty PA driven by CA signals. In addition the linearization performance of the proposed single TOR and single TE DPD system and the RLS/MRAC learning approach was compared to a conventional DPD system that exploits two TOR paths and two training engines together with a LSE/STR indirect learning approach. In the following experiments, an inter-band CA signal formed by a 15 MHz WCDMA signal at 1.8GHz and a 15 MHz LTE signal at 2.1 GHz was synthesized and served as first stimuli. As a second test signal, an intra-band CA signal was formed by a 15 MHz WCDMA signal at 1.96 GHz and a 20 MHz LTE signal at 2.035 GHz. The BBE Volterra based dual band DPD model which was used in these experiments has a nonlinearity order and memory depth equal to 7 and 3, respectively.

The PA output spectra obtained using the first test signal, with and without DPD, are shown in Fig. 6.2. According to Fig. 6.2, the proposed DPD system succeeded to cancel the out of band emission yielding an adjacent channel leakage ratio (ACLR) of better than -50dBc in both bands. Furthermore, as per Fig. 6.3, the proposed DPD system necessitated about 4 iterations, per band, in order to converge to the lowest error vector

magnitude (EVM) and ACLR values. In contrary, the DPD system that employed two TOR paths converged only after 2 iterations. Similar linearization results were obtained using the second test signal and shown in Fig. 6.4-6.5.

Hence one can conclude that the proposed single TOR and single TE DPD system along with RLS/MRAC algorithm provided a good trade off between arithmetic complexity and convergence speed with out compromising the linearization capacity.
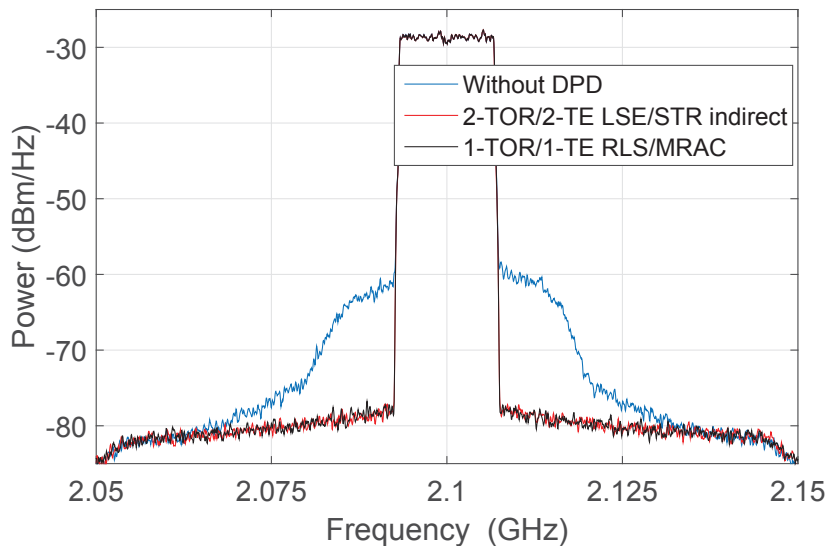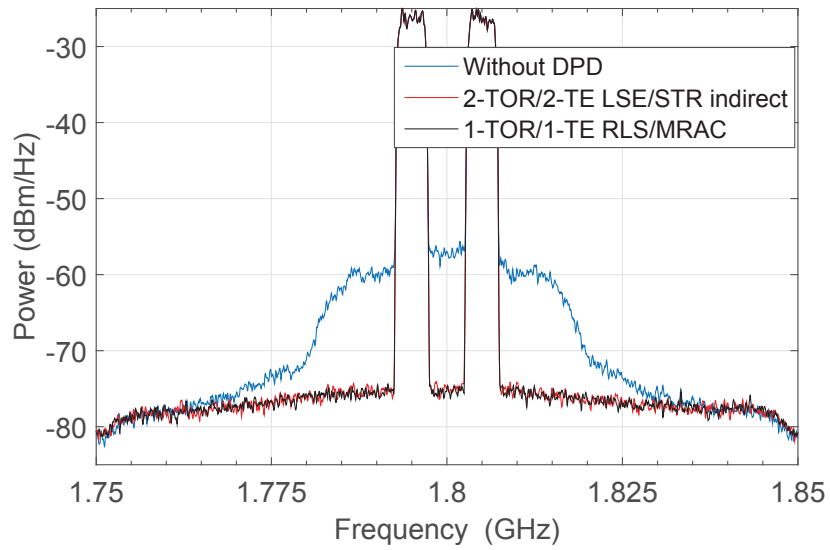
Figure 6.2: Linearization results for Class F Doherty PA driven by (upper) 15 MHz WCDMA signal @ 1.8 GHz and (lower) 15 MHz LTE signal @ 2.1 GHz
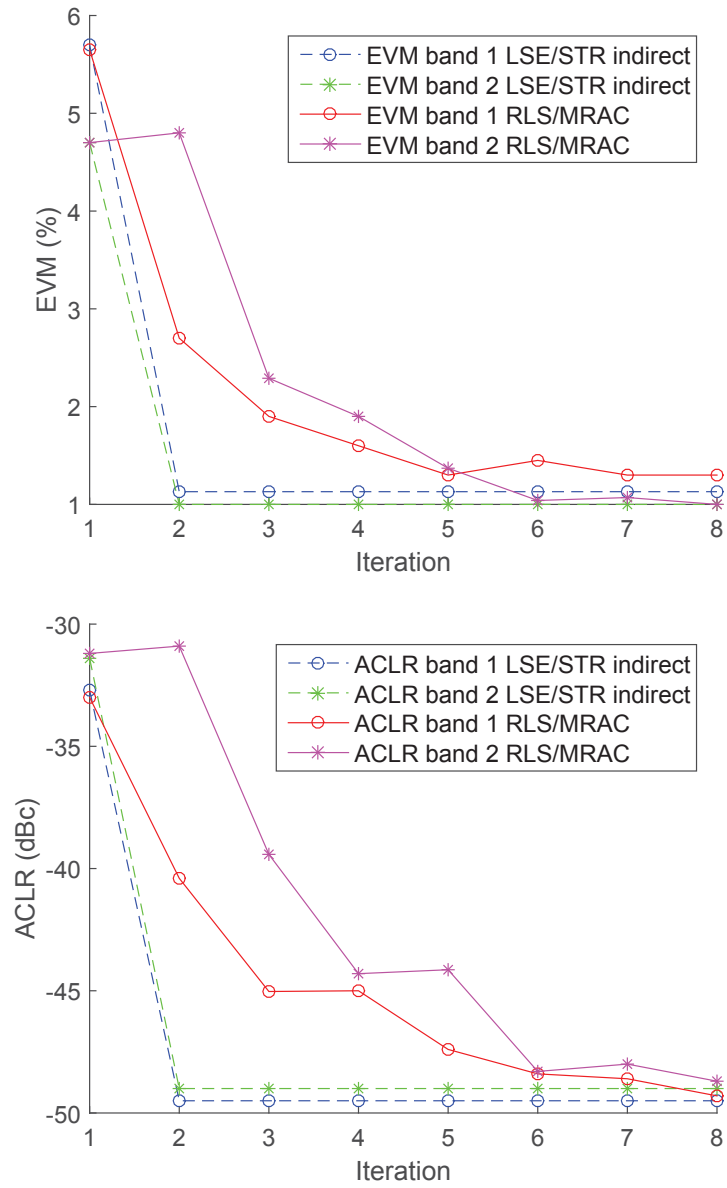
Figure 6.3: EVM (upper) and ACLR (lower) results for Class F Doherty PA driven by 15 MHz WCDMA signal @ 1.8 GHz and 15 MHz LTE signal @ 2.1 GHz
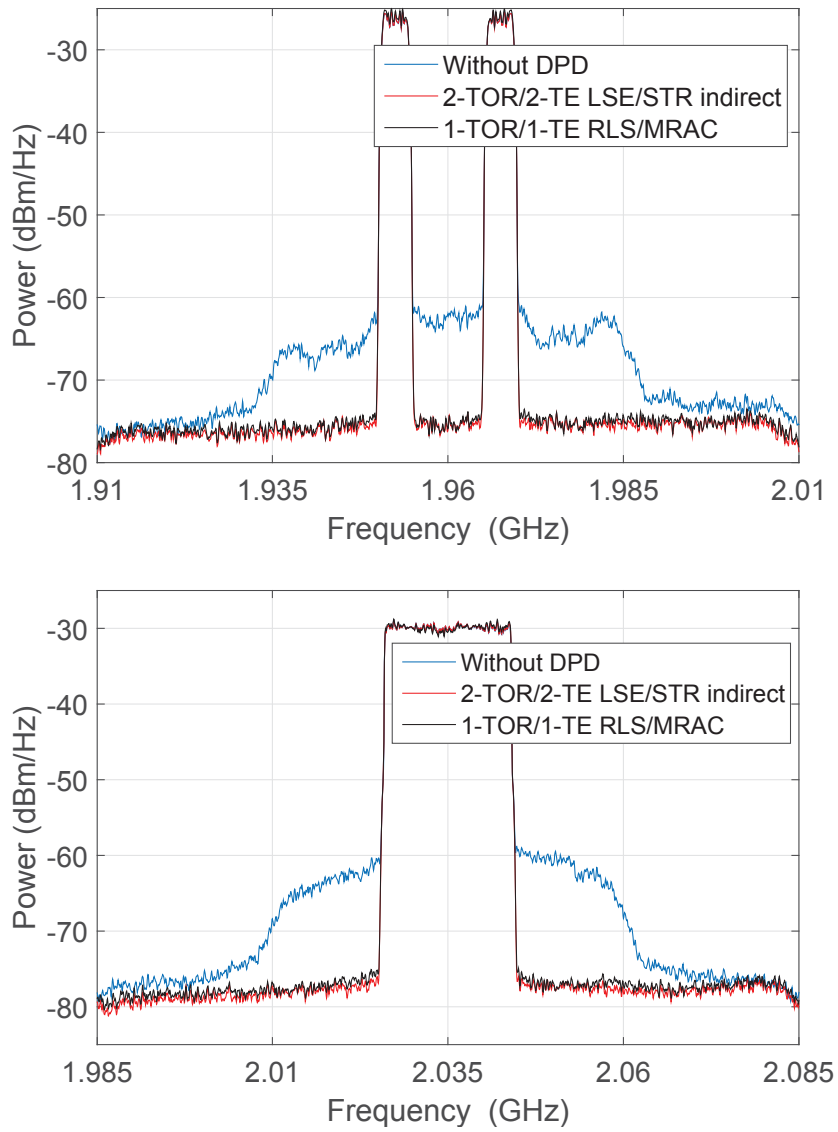
Figure 6.4: Linearization results for Class F Doherty PA driven by (upper) 20 MHz WCDMA signal @ 1.96 GHz and (lower) 20 MHz LTE signal @ 2.035 GHz
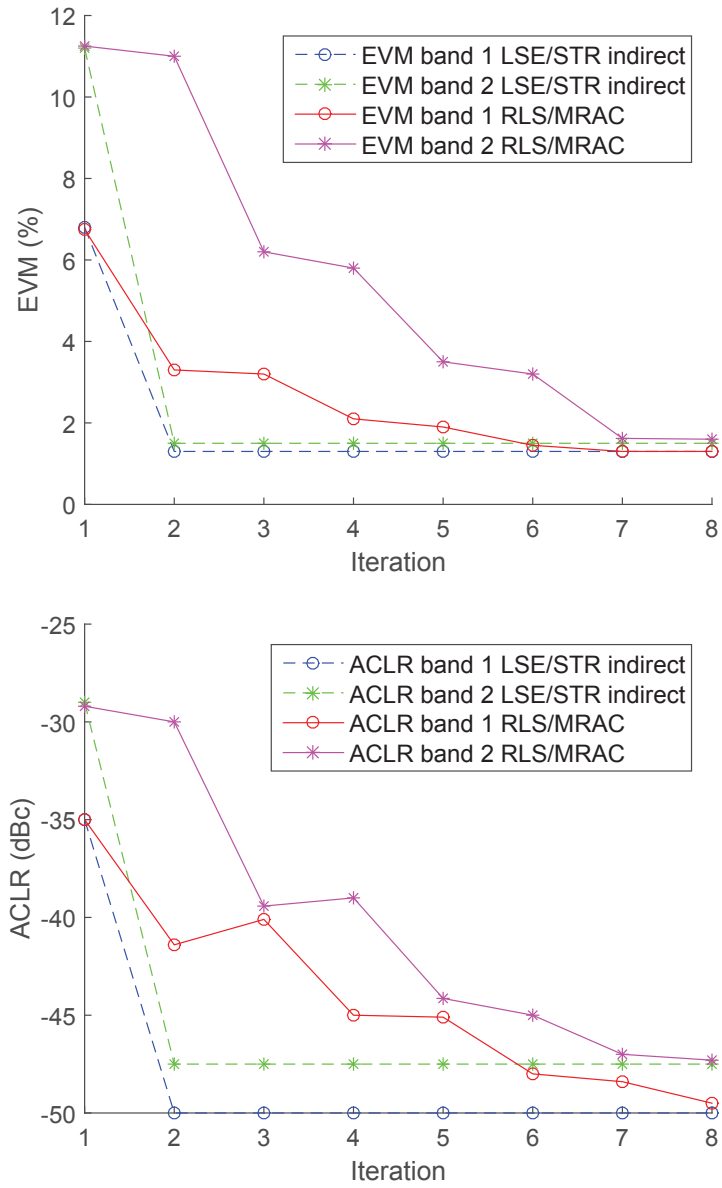
Figure 6.5: EVM (upper) and ACLR (lower) results for Class F Doherty PA driven by 20 MHz WCDMA signal @ 1.96 GHz and 20 MHz LTE signal @ 2.035 GHz

Chapter 7

Conclusion

The carrier aggregation concept was recently adopted by wireless communication standardization bodies to meet the need for wider band communication signals and better spectrum resource utilization. The component carriers are either deployed in the same communication band (i.e., intra-band carrier aggregation), or distributed over widely spaced frequency bands (i.e., inter-band carrier aggregation). Being dependent on the component carriers' frequency separation and requiring unpractical sampling rates, carrier aggregated signals challenged the application of conventional DPD and CFR techniques. This thesis proposed novel behavioral modeling schemes and CFR techniques which are independent of the component carriers' separation and run at low sampling rates.

A second challenge introduced by carrier aggregated signals, is the projected use of up to five component carriers requiring an equal number of predistorters, TORs and TEs. This thesis proposed a joint optimization approach for predistortion and a time sharing solution for the TOR and TE.

A summary of the different novel contributions made by this thesis work are presented in the following sections.

7.1   Summary of Contributions

The first research contribution is a novel CFR technique for carrier aggregated signals. The conventional SISO CFR approach was discussed and proven to be unsuitable for carrier aggregation scenarios. A peak estimator was proposed to enable CFR implementation with a significant decrease in the sampling rate proportional to the maximum of the bandwidth of the two carriers rather than the spacing between them. The proposed solution was extended to address carrier aggregation scenarios where the power levels and EVM requirements of the individual CCs are different. The proposed approach was also extended to the case of

an arbitrary number of CCs. The proposed solutions were demonstrated using multi-band carrier aggregated signals composed of LTE and WCDMA signals. The proposed approach appears suitable for driving RF PAs at higher efficiency and with effective average power.

Next, a novel BBE Volterra series formulation for the behavioral modeling of PAs was proposed. The model was developed by modeling the RF PA input-output behavior, then equating and demodulating both the input and output passband signals to baseband. The novel formulation is inherently compact and calls for significantly fewer coefficients then its LPE counterpart and, therefore, avoids the accuracy compromising pruning transformations widely applied to classical formulations in the literature. The experimental validation proved the excellent modeling and linearization performance of the novel method when compared to the classical non-pruned Volterra model. The new formulation also outperformed pruned Volterra models while using a lower number of coefficients.

Utilizing the single-band BBE Volterra model, a novel DIDO BBE Volterra series predistorter was proposed to linearize a dual-band PA driven by a carrier aggregated signal. Starting with a real-valued, continuous-time, pass-band Volterra series, and using a number of signal and system transformations, a low complexity complex-valued and discrete BBE Volterra formulation was derived. While the proposed formulation included all possible distortion terms, it involved fewer kernels than its 2D-DPD counterpart. The proposed model was successfully applied to digitally predistort and linearize a dual-band 45 W class AB GaN PA driven with different dual-band dual-standard test signals. For each band, the model needed less than 25 coefficients to reduce the ACLR by up to 25 dB.

Research efforts then targeted the efficient hardware implementation of the predistortion algorithm. An automated symbolic optimization methodology was proposed to optimize the arithmetic representation of Volterra based predistortion schemes. When used in conjunction with fixed point conversion tools and HLS tools, the proposed approach enabled an automated reduction of the predistortion hardware implementation burden. The proposed approach was applied to single- and dual-band BBE Volterra series schemes and used to linearize a 45W GaN PA driven by single and carrier aggregated signals. The proposed methodology yielded an HDL code for the Volterra based DPD that is manageable with typical commercial FPGAs and allowed the reduction of the total number of MAC operations from 584 to 161 in the case of the single-band BBE Volterra and from 2256 to 375 in the case of the dual band BBE Volterra.

The final contribution of this thesis is a 1-TOR/1-TE architecture for adaptive real-time predistortion of PAs driven by carrier aggregated signals. An RLS/MRAC observation and TE was proposed to alternately estimate and adapt each of the component carriers' predistorter coefficients. The presented concept was used to linearize a 20 W Class F Doherty PA under different multi-standard carrier aggregated signals with different bandwidths and frequency separations.

7.2 List of Publications

Refereed Journal Papers

1. B. Fehri, S. Boumaiza, "Baseband Equivalent Volterra Series for Digital Predistortion of Dual-Band Power Amplifiers," IEEE Transactions on Microwave Theory and Techniques, vol. 60, no. 3, pp. $700 - 714$, Mar. 2014.

2. B. Fehri, S. Boumaiza, "Baseband Equivalent Volterra Series for Behavioral Modeling and Digital Predistortion of Power Amplifiers Driven With Wideband Carrier Aggregated Signals," IEEE Transactions on Microwave Theory and Techniques, vol. 62, no. 11, pp. $2594 - 2603$, Nov. 2014.

3. B. Fehri, S. Boumaiza, "Crest Factor Reduction of Inter-band Multi-standard Carrier Aggregated Signals," IEEE Transactions on Microwave Theory and Techniques, vol. 62, no. 12, pp. 3286 - 3297, Dec. 2014.

4. B. Fehri, S. Boumaiza, "Single Transmitter Observation Receiver with Single Training Engine for Linearization of Multi-band Power Amplifiers," IEEE Transactions on Microwave Theory and Techniques, in review.

Conference Papers

1. B. Fehri, S. Boumaiza, "Systematic Estimation of Memory Effects Parameters in Power Amplifiers' Behavioral Models," IEEE MTT-S International Microwave Symposium, pp. 1–4, Baltimore MD, Jun. 2011.

2. B. Fehri, S. Boumaiza, "Joint Dual-band Crest Factor Reduction and Digital Predistortion of Power Amplifiers Driven by Inter-Band Carrier Aggregated Signals," IEEE MTT-S International Microwave Symposium Digest, pp. 1–4, Tampa Bay FL, Jun. 2014.

3. B. Fehri, S. Boumaiza, "Automated Symbolic Optimization and High Level Synthesis of Single- and Multi-band Digital Pre-distortion Hardware in an FPGA," IEEE MTT-S International Microwave Symposium, pp. 1–3, Phoenix AZ, May 2015.

Patent Applications

1. B. Fehri, S. Boumaiza, and E. Sich, "Crest Factor Reduction of Inter-band Multi-Standard Carrier Aggregated Signals," Country US, Provisional Application No: 61/886,317, File Date October 3, 2013.

2. B. Fehri, and S. Boumaiza, "Baseband Equivalent Volterra Series for Digital Predistortion in Multi-band Power Amplifiers," Country US, Provisional Application No: 61/886,907, File Date October 4, 2013.

3. B. Fehri, and S. Boumaiza, "Baseband Equivalent Volterra Series for Behavioral Modeling and Digital Predistortion of Wideband Transmitters," Country US, Provisional Application No: 61/887,012, File Date October 4, 2013.

4. B. Fehri, and S. Boumaiza, "Method and Apparatus for Multi-band Predistortion Using Time-Shared Adaptation Loop," Country US, File Date March 31, 2015.

7.3 Future Work

LTE-A standards project the use of up to five component carriers' communication signals. These component carriers can be deployed in different intra-band and inter-band aggregation scenarios. The radio unit is expected to support flexible deployment in terms of the number of component carriers, center frequencies and output power. The different processing units, among them the CFR and DPD modules, impose contradictory requirements on handling the different component carriers as intra-band or inter-band signals. Radios can be over-designed to handle the different scenarios separately, and inefficiently. A close examination of the different deployment scenarios should identify an adequate approach for efficient hardware implementation.

Predistortion models and CFR techniques are also challenged in pico and femto cells scenarios. Their power consumption currently makes them inefficient for use in small cells. The investigation of low power analog predistortion and CFR circuits may enable those techniques to be altered and made appropriate for use in small cell radios.

Above all, research work towards 5G standards predicts a massive deployment of MIMO systems. Dedicating one CFR and DPD module per antenna would be impractical. Innovative approaches must be developed.

Bibliography

[1] ETSI TS 136 104, "Evolved Universal Terrestrial Radio Access (EUTRA); Base Station (BS) radio transmission and reception", V11.3.1, Feb. 2013.

[2] K. Bathich, A. Z. Markos, and G. Boeck, "Frequency response analysis and bandwidth extension of the Doherty amplifier," IEEE Transaction on Microwave Theory & Techniques, vol. 59, no. 4, pp. 934–944, Apr. 2011.

[3] R. W. Bauml, R. F. H. Fischer, and J. B. Huber, "Reducing the peak-to average power ratio of multicarrier modulation by selected mapping", Electronics Letters, vol. 32, no. 22, pp. 2056–2057, Oct. 1996.

[4] W. S. Ho, A. S. Madhukumar, and F. Chin, "Peak-to-average power reduction using partial transmit sequences: a suboptimal approach based on dual layered phase sequencing," IEEE Transactions on Broadcasting, vol. 49, no. 2, pp. 225–231, June 2003.

[5] S.Litsyn, Peak Power Control in Multicarrier Communications, Cambridge University Press, 2007.

[6] S. H. Han, and J. H. Lee, "An overview of peak-to-average power ratio reduction techniques for multicarrier transmission," IEEE Wireless Communications Magazine, vol. 12, no. 12, pp. 56–65, Apr. 2005.

[7] H. Ochiai, and H. Imai, "Performance analysis of deliberately clipped OFDM signals," IEEE Transaction on Communication, vol. 50, no. 1, pp. 89–101, Jan. 2002.

[8] X. Huang, J. Lu, J. Zheng, K. B. Letaief, and J. Gu, "Companding transform for reduction in peak-to-average power ratio of OFDM signals," IEEE Transaction On Wireless Communication, vol. 3, no. 6, pp. 2030–2039, Nov. 2004.

[9] B. S. Krongold, and D. L. Jones, "PAR reduction in OFDM via active constellation extension", IEEE Transactions on Broadcasting, vol. 49, no. 3, pp. 258–268, Sept. 2003.

[10] A. Saul, "Generalized active constellation extension for peak reduction in OFDM systems," in IEEE International Conference on Communications, vol. 3, pp. 1974–1979, May 2005.

[11] L. Hanzo et all, OFDM and MC-CDMA for broadband multi user communications, WLANs, and broadcasting, Wiley, 2003.

[12] M. Helaoui, S. Boumaiza, A. Ghazel, F.M. Ghannouchi, "Power and efficiency enhancement of 3G multicarrier amplifiers using digital signal processing with experimental validation", IEEE Transaction On Microwave Theory And Techniques, vol. 54, no. 4, pp. 1396 − 1404, June 2006

[13] D. Y.-T. Wu, S. Boumaiza, "A Modified Doherty Configuration for Broadband Amplification Using Symmetrical Devices", IEEE Transactions Microwave Theory and Techniques, vol. 60, no. 10, pp. 3101–3213, Oct. 2012.

[14] J. Moon, J. Son, J. Lee, B. Kim, "A Multimode/Multiband Envelope Tracking Transmitter With Broadband Saturated Amplifier", IEEE Transactions Microwave Theory and Techniques, vol. 59, no. 12, pp. 3463–3473, Dec. 2011.

[15] A. Zhu, T. Brazil, "Behavioral Modeling of RF Power Amplifiers Based on Pruned Volterra Series", IEEE Microwave and Wireless Components Letters, vol. 14, no. 12, pp. 563–565, Dec. 2004.

[16] J. C. Pedro and S. A. Maas, "A Comparative Overview of Microwave and Wireless Power-Amplifier Behavioral Modeling Approaches", IEEE Transactions Microwave Theory and Techniques, vol. 53, no.4, pp. 1150–1163, Apr. 2005.

[17] J. Kim and K. Konstantinou, "Digital predistortion of wide-band signals based on power amplifier model with memory", Electronics Letter, vol. 37, no. 23, pp. 1417–1418, Nov. 2001.

[18] A. Zhu et al., "Dynamic Deviation Reduction-Based Volterra Behavioral Modeling of RF Power Amplifiers", IEEE Transactions on Microwave Theory and Techniques, vol. 54, no. 12, pp. 4323–4332 , Dec. 2006.

[19] S. Boyd and L. Chua, "Fading memory and the problem of approximating nonlinear operator with Volterra series", IEEE Transactions on Circuit and Systems, vol. 32, no. 11, pp. 1150–1161, Nov. 1985.

[20] M. Isaksson et al., "A Comparative Analysis of Behavioral Models for RF Power Amplifiers", IEEE Transactions On Microwave Theory And Techniques, vol. 54, no. 1, pp. 348–359, Jan. 2006.

[21] A. Zhu, J. Dooley, T. Brazil, "Simplified Volterra Series Based Behavioral Modeling of RF Power Amplifiers Using Deviation-Reduction", in IEEE MTT-S International Microwave Symposium Digest, pp. 1113–1116, June 2006.

[22] S. Benedetto, E. Biglieri, and R. Daffara, "Modeling and performance evaluation of nonlinear satellite links—A Volterra series approach", IEEE Trans. Aerosp. Electron. Syst., vol. 15, no. 4, pp. 494–507, July 1979.

[23] M. Schetzen, The Volterra and Wiener Theories of Nonlinear Systems, John Wiley and Sons Inc., New York, 1980.

[24] C.-H. Cheng, E.J. Powers, "Optimal Volterra kernel estimation algorithms for a nonlinear communication system for PSK and QAM inputs", IEEE Transactions on Signal Processing, vol. 49, no. 1, pp. 147–163, Jan 2001.

[25] A. Gutierrez, W.E. Ryan, "Performance of Volterra and MLSD receivers for nonlinear band-limited satellite systems", IEEE Transactions on Communications, vol. 48, no. 7, pp. 1171–1177, Jul 2000.

[26] Cherif, I., Abid, S., Fnaiech, F., "On The Identification of Nonlinear Digital Transmission Channels", in IEEE International Conference on E-Learning in Industrial Electronics, pp. 185–190, 2006.

[27] A.J. Redfern, G.T. Zhou, "Blind zero forcing equalization of multichannel nonlinear CDMA systems", IEEE Transactions on Signal Processing, vol. 49, no. 10, pp. 2363–2371, Oct. 2001.

[28] C.A. R. Fernandes, J. C. M. Mota, G. Favier, "Analysis and Power Diversity-Based Cancellation of Nonlinear Distortions in OFDM Systems", IEEE Transactions On Signal Processing, vol. 60, no. 7, pp. 3520–3531, July 2012.

[29] A.J. Redfern, G.T. Zhou, "Decision feedback equalization for Volterra systems-a root method", in Conference on Signals Systems & Computers, vol. 1, pp. 47–51, Nov. 1998.

[30] Baylis, C., Marks, R.J., "Small Perturbation Harmonic Coupling in Nonlinear Periodicity Preservation Circuits", IEEE Transactions on Circuits and Systems I, vol. 59, no. 12, pp. 3034–3045, Dec. 2012.

[31] Karam, G., Sari, H., "Improved data predistortion using intersymbol interpolation", in IEEE International Conference on Communications, vol. 1, pp. 286–291, 1989.

[32] C. C. Cadenas, J. R. Tosina, M. J. M. Ayora, J. M. Cruzado, "A New Approach to Pruning Volterra Models for Power Amplifiers", IEEE Transactions On Signal Processing, vol. 58, no. 4, pp. 2113–2120, Apr. 2010.

[33] T.R. Cunha, E.G. Lima, J.C. Pedro, "Validation and Physical Interpretation of the Power-Amplifier Polar Volterra Model", IEEE Transactions on Microwave Theory and Techniques, vol. 58, no. 12, pp. 4012–4021, Dec. 2010.

[34] M. Green, A.M. Zoubir, "Selection of a time-varying quadratic Volterra model using a wavelet packet basis expansion", IEEE Transactions on Signal Processing, vol. 52, no. 10, pp. 2721–2728, Oct. 2004.

[35] P. Singerl, H. Koeppl, "Volterra kernel interpolation for system modeling and predistortion purposes", in International Symposium on Signals Circuits and Systems ISSCS 2005, vol. 1, pp. 251–254, July 2005.

[36] R. Raich, G.T. Zhou, "Orthogonal polynomials for complex Gaussian processes", IEEE Transactions on Signal Processing, vol. 52, no. 10, pp. 2788–2797, Oct. 2004.

[37] Y.-J. Liu, W. Chen, J. Zhou, B.-H. Zhou, F.M. Ghannouchi, Y.-N. Liu, "Modified Least Squares Extraction for Volterra-Series Digital Predistorter in the Presence of Feedback Measurement Errors", IEEE Transactions on Microwave Theory and Techniques, vol. 60, no. 11, pp. 3559–3570, Nov. 2012.

[38] Y. S. Shmaliy, Continuous Time Systems (Signals and Communication Technology), Springer, Dordrecht Netherlands, 2007, p. 450-455.

[39] J. Wood, Fundamentals of Nonlinear Behavioral Modeling for RF and Microwave Design, Artech House, Boston | London, 2005.

[40] M. Iwamoto, A. Williams, P.-F. Chen, A. G. Metzger, L. E. Larson, and P. M. Asbeck, "An extended Doherty amplifier with high efficiency over a wide power range," IEEE Trans. Microw. Theory Tech., vol. 49, no. 12, pp. 2472–2479, Dec. 2001.

[41] I. Kim, J. Moon, S. Jee, and B. Kim, "Optimized design of a highly efficient three-stage Doherty PA using gate adaptation," IEEE Trans. Microw. Theory Tech., vol. 58, no. 10, pp. 2562–2574, Oct. 2010.

[42] J. Kim, J. Cha, I. Kim, and B. Kim, "Optimum operation of asymmetrical- cells-based linear Doherty power amplifiers—Uneven power drive and power matching," IEEE Trans. Microw. Theory Tech., vol. 53, no. 5, pp. 1802–1809, May 2005.

[43] M. Nick and A. Mortazawi, "Adaptive input-power distribution in Doherty power amplifiers for linearity and efficiency enhancement," IEEE Trans. Microw. Theory Tech., vol. 58, no. 11, pp. 2764–2771, Nov. 2010.

[44] D. F. Kimball, J. Jeong, C. Hsia, P. Draxler, S. Lanfranco, W. Nagy, K. Linthicum, L. E. Larson, and P. M. Asbeck, "High-efficiency envelope tracking W-CDMA base-station amplifier using GaN HFETs," IEEE Trans. Microw. Theory Tech., vol. 54, no. 11, pp. 3848–3856, Nov. 2006.

[45] D. Kang, D. Kim, J. Choi, J. Kim, Y. Cho, and B. Kim, "A multimode/ multi-band power amplifier with a boosted supply modulator," IEEE Trans. Microw. Theory Tech., vol. 58, no. 10, pp. 2598–2608, Oct. 2010.

[46] B. Kim, J. Moon, and I. Kim, "Efficiently amplified," IEEE Microw. Mag., vol. 11, no. 5, pp. 89–100, Aug. 2010.

[47] J. H. Qureshi, N. Li, W. C. E. Neo, F. Rijs, I. Blednov, and L. C. N. de Vreede, "A wideband 20 W LMOS Doherty power amplifier," in IEEE MTT-S Int. Microw. Symp. Dig., Anaheim, CA, pp. 1504–1507, May 2010.

[48] D. Kang, D. Kim, Y. Cho, B. Park, J. Kim, and B. Kim, "Design of bandwidth-enhanced Doherty power amplifiers for handset applications," IEEE Trans. Microw. Theory Tech., vol. 59, no. 12, pp. 3474–3483, Dec. 2011.

[49] J. Moon, J. Son, J. Lee, J. Kim, S. Jee, S. Kim, and B. Kim, "A multimode/multiband envelope tracking transmitter with broadband saturated power amplifier," in IEEE MTT-S Int. Microw. Symp. Dig., Jun. 2011, pp. 1–4.

[50] J. Zhai, J. Zhou, L. Zhang, J. Zhao, and W. Hong, "Dynamic behavioral modeling of power amplifiers using ANFIS-based Hammerstein", IEEE Microw Wireless Compon Lett, 18, pp. 704–706, 2008.

[51] P.L. Gilabert, G. Montoro, and E. Bertran, "On the Wiener and Hammerstein models for power amplifier predistortion", Proc Asia-Pacific Microwave Conf 2005, Suzou, China, vol. 2, pp. 1–4, Dec. 2005.

[52] D. R. Morgan, Z. Ma, J. Kim, M. G. Zierdt, and J. Pastalan, "A generalized memory polynomial model for digital predistortion of RF power amplifiers," IEEE Trans. Signal Process., vol. 54, no. 10, pp. 3852–3860, Oct. 2006.

[53] D. Mirri, G. Luculano, et al, "A modified Volterra series approach for nonlinear dynamic systems modeling," IEEE Trans. on Circuits and Systems I: Fundamental Theory and Applications, vol. 49, no. 8, pp.1118-1128, Aug. 2002.

[54] F. Mkadem and S. Boumaiza, "Extended Hammerstein behavioral model using artificial neural networks," IEEE Trans. Microw. Theory Tech., vol. 57, no. 4, pp. 745–751, Apr. 2009.

[55] J. Wood, M. LeFevre, D. Runton, J. C. Nanan, B. H. Noori, and P. H. Aaen, "Envelope-domain time series (ET) behavioral model of a Doherty RF power amplifier for system design," IEEE Trans. Microw. Theory Tech., vol. 54, no. 8, pp. 3163–3172, Aug. 2006.

[56] M. Isaksson, D. Wisell, and D. Rönnow, "Wide-band dynamic modeling of power amplifiers using radial-basis function neural networks," IEEE Trans. Microw. Theory Tech., vol. 53, no. 11, pp. 3422–3428, Nov. 2005.

[57] F. Mkadem, and S. Boumaiza, "Physically inspired neural network model for RF power amplifier behavioral modeling and digital predistortion", IEEE Trans. Microw. Theory Tech., vol. 59, no. 4, Apr. 2011.

[58] P. Roblin, S. K. Myoung, D. Chaillot, Y. G. Kim, A. Fathimulla, J. Strahler, and S. Bibyk, "Frequency-selective predistortion linearization of RF power amplifiers," IEEE Trans. Microw. Theory Tech., vol. 56, no. 1, pp. 65–76, Jan. 2008.

[59] J. Kim, P. Roblin, X. Yang, and D. Chaillot, "A new architecture for frequency selective digital predistortion linearization for RF power amplifiers", in IEEE MTT-S Int. Microw. Symp. Dig., Jun. 2012.

[60] A. Cidronali, I. Magrini, R. Fagotti, and G. Manes, "A new approach for concurrent dual-band IF digital predistortion: System design and analysis", INMMIC Workshop, 2008.

[61] S. A. Bassam, M. Helaoui, and F. M. Ghannouchi, "2-D digital predistortion (2-D-DPD) architecture for concurrent dual-band transmitters", IEEE Trans. Microw. Theory Tech, vol. 59, no. 10, Oct. 2011, pp. 2547-2553

[62] S. A. Bassam, W. Chen, M. Helaoui, F. M. Ghannouchi, and Z. Feng, "Linearization of Concurrent Dual-Band Power Amplifier Based on 2D-DPD Technique", IEEE Microwave And Wireless Components Letters, Vol. 21, No. 12, Dec. 2011 p., 685-687.

[63] P. Saad, P. Colantonio, J. Moon, L. Piazzon, F. Giannini, K. Andersson, B. Kim, and C. Fager, "Concurrent Dual-Band GaN-HEMT Power Amplifier at 1.8 GHz and 2.4 GHz", 13th Annual IEEE WAMICON Conference, Ap. 2012, Florida, USA.

[64] W. Chen, S.A. Bassam, X. Li, Y. Liu, K. Rawat, M. Helaoui, F.M. Ghannouchi, and Z. Feng, "Design and linearization of concurrent dual-band Doherty power amplifier with frequency- dependent power ranges", IEEE Trans Microw Theory Tech, 59, pp. 2537–2546, 2011,

[65] S. A. Bassam, A. Kwan, W. Chen, M. Helaoui, and F. M. Ghannouchi, "Subsampling Feedback Loop Applicable to Concurrent Dual-Band Linearization Architecture", IEEE Transactions on Microwave Theory And Techniques, Vol. 60, No. 6, June 2012.

[66] L. Ding, Z. Yang, and H. Gandhi, "Concurrent Dual-band Digital Predistortion", International Microwave Symposium Digest (MTT), June 2012.

[67] A. Kwan, S. Bassam, M. Helaoui, F. Ghannouchi, "Concurrent Dual Band Digital Predistortion using Look Up Tables with Variable Depths", PAWR 2013.

[68] C. Quindroit, N. Naraharisetti, P. Roblin, S. Gheitanchi, V. Mauer and M. Fitton, "Concurrent Dual-Band Digital Predistortion for Power amplifier based on Orthogonal Polynomials", IEEE MTT-S International Microwave Symposium Digest (IMS) 2013.

[69] G. Yang, F. Liu, L. Li, H. Wang, C. Zhao, and Z. Wang, "2D Orthogonal Polynomials for Concurrent Dual-Band Digital Predistortion", IEEE MTT-S International Microwave Symposium Digest (IMS) 2013.

[70] Y.-J. Liu, W. Chen, J. Zhou, B.-H. Zhou, F. M. Ghannouchi, "Behavioral Modeling for Concurrent Dual-band Power Amplifiers Using 2D Hammerstein/Wiener Models", International Journal of RF and Microwave Computer-Aided Engineering, Nov. 2012.

[71] D. Y-T. Wu, S. Boumaiza, "Design of a broadband and highly efficient 45W GaN power amplifier via simplified real frequency technique", IEEE MTT-S International Microwave Symposium Digest (IMS) 2010, pp. 1090 − 1093, 2010.

[72] 3GPP TS 36.104 version 11.6.0 Release 11

[73] http://www.3gpp.org/Carrier-Aggregation-explained

[74] S. C. Cripps, RF Power Amplifiers for Wireless Communications, Artech House Publishers; 2 edition, June 2006

[75] N. Mrabet, I. Mohammad, F. Mkadem, C. Rebai, S. Boumaiza, "Optimized hardware for polynomial digital predistortion system implementation", PAWR, January 2012.

[76] F. Mkadem, M. C. Fares, S. Boumaiza and J. Wood, "Complexity- reduced Volterra series model for power amplifier digital predistortion," Analog Integr. Circ. Sig. Process, vol. 79, no. 2, pp. 331-343, Feb. 2014.

[77] B. Fehri, S. Boumaiza, "Baseband Equivalent Volterra Series for Behavioral Modeling and Digital Predistortion of Power Amplifiers Driven With Wideband Carrier Aggregated Signals," IEEE Trans. Microw. Theory Tech., vol., no. 99, pp. 2594 - 2603, Oct. 2014.

[78] Y. Ma, Y. Yamao, Y. Akaiwa, and C. Yu, "FPGA Implementation of Adaptive Digital Predistorter with Fast Convergence Rate and Low Complexity for Multi-Channel Transmitters", IEEE Trans. Microw. Theory Tech., vol. 61, no. 11, pp. 3961–3973, Nov. 2013.

[79] C. D. Presti, D. F. Kimball, and P. Asbeck, "Closed-Loop Digital Predistortion System With Fast Real-Time Adaptation Applied to a Handset WCDMA PA module", IEEE Trans. Microw. Theory Tech., vol. 60, no. 3, pp. 604–618, Mar. 2012.

[80] P. Roblin, C. Quindroit, N. Naraharisetti, S. Gheitanchi, V. Mauer and M. Fitton, "Concurrent Linearization: The State of the Art for Modeling and Linearization of Multiband Power Amplifiers", IEEE Microwave magazine, vol. 14, no. 7, pp. 75 − 91, Nov.-Dec. 2013.

[81] L. Guan, and A. Zhu, "Low-Cost FPGA Implementation of Volterra Series-Based Digital Predistortion for RF Power Amplifiers", IEEE Trans. On Microw. Theo. and. vol. 58, no. 4, pp. 866–871, Ap. 2010.

[82] N. Mrabet, F. Mkadem, O. Petelin, H. Medini and S. Boumaiza, "Mixed-Signal Multi-mode Radio Software/Hardware Development Platform," IEEE Microwave Magazine, vol. 14, nb. 1, pp. 128 - 133, Jan. 2013.

[83] R. N. Braithwaite, "RF Power Amplifier System Employing An Analog Predistortion Module Using Zero Crossings," U.S. Patent WO/2006/102278. 28, 09, 2006.

[84] Fehri, S. Boumaiza, "Baseband Equivalent Volterra Series for Digital Predistortion of Dual-Band Power Amplifiers," IEEE Transactions on Microwave Theory and Tech., vol. 60, no. 3, pp. 700 − 714, March 2014.

[85] A. Zhu, T. J. Brazil, "An adaptive Volterra predistorter for the linearization of RF high power amplifiers," 2002 IEEE MTT-S International Microw. Symp. Digest, Vol.1, pp. 461-464, June 2002.

[86] J. Moon, J. Son, J. Lee, and B. Kim, "A Multimode/Multiband Envelope Tracking Transmitter With Broadband Saturated Amplifier", IEEE Transactions Microwave Theory and Techniques, vol. 59, no. 12, pp. 3463–3473, Dec. 2011.

[87] M. Younes, A. Kwan, M. Rawat, F.M. Ghannouchi, "Linearization of Concurrent Tri-Band Transmitters Using 3-D Phase-Aligned Pruned Volterra Model," IEEE Trans. Microw. Theory Tech, vol. 61, no. 12, pp. 4569-4578, Nov. 2013.

[88] C. Yu, L. Guan, E. Zhu, and A. Zhu, "Band-Limited Volterra Series-Based Digital Predistortion for Wideband RF Power Amplifiers," IEEE Trans. Microw. Theory and Tech., pp. 4198- 4208, vol. 60, no. 12, Dec. 2012.

[89] F. Mkadem, S. Boumaiza, "Nonlinear system behavioral modeling using reduced transmitter observation receiver bandwidth," ARFTG Microwave Measurement Conference, Tampa FL, June 2014.

[90] N. Naraharisetti, P. Roblin, C. Quindroit, M. Rawat, S. Gheitanchi, "2D Quasi Exact Inverse of PA model in Digital Predistorter for Concurrent Dual-Band System," IEEE 15th Annual Wireless and Microwave Technology Conference (WAMICON), 2014.

[91] C. Yu, and A. Zhu, "Single feedback loop-based digital predistortion for linearizing concurrent multi-band transmitters," International Microwave Sympoisum (IMS), Tampa FL, June 2014.

[92] J. Wood, "Digital Pre-Distortion," in Behavioral Modeling and Linearization of RF Power Amplifiers, 1st ed. Norwood MA: Artech house, 2014, pp. 228-237.

[93] C. Quindroit, N. Naraharisetti, P. Roblin, S. Gheitanchi, V. Mauer and M. Fitton, "FPGA Implementation of Orthogonal 2D Digital Predistortion System for Concurrent Dual-Band Power Amplifiers Based on Time-Division Multiplexing", IEEE Transactions on Microwave Theory And Techniques, vol. 61, no. 12, pp. 4591 - 4599, Nov. 2013.

[94] B. Fehri, S. Boumaiza, "Automated Symbolic Optimization and High Level Synthesis of Single- and Multi- Band Digital Pre-distortion Hardware in an FPGA," IEEE MTT-S International Microwave Symposium Digest (IMS), May 2015.

[95] H. Xiang, C. Yu, J. Gao, S. Li, Y. Wu, M. Su and Y. Liu, "Dynamic deviation reduction-based concurrent dual-band digital predistortion," International Journal of RF and Microwave Computer-Aided Engineering, vol. 24, no. 3, pp. 401–411, May 2014.

[96] H. Sarbishaei, B. Fehri, Y. Hu, S. Boumaiza, "Dual-Band Volterra Series Digital Pre-Distortion for Envelope Tracking Power Amplifiers," IEEE Microwave and wireless Components letters, Vol. 24, No. 6, pp. 430 - 432, June 2014.

[97] A. Kwan, M. Younes, S. Zhang, W. Chen, R. Darraji, M. Helaoui, and F. M. Ghannouchi, "Dual-band predistortion linearization of an envelope modulated power amplifier operated in concurrent multi-standard mode," IEEE MTT-S International Microwave Symposium Digest, pp.1–4, Jun. 2014.

[98] P. Gilabert, G. Montoro, "3-D Distributed Memory Polynomial Behavioral Model for Concurrent Dual-Band Envelope Tracking Power Amplifier Linearization," IEEE Transactions on Microwave Theory And Techniques, vol. 63, no. 2, pp. 638 - 648, Feb. 2015.